STM Study of Interfaces and Defects in 2D Materials

Husong Zheng

Dissertation submitted to the faculty of the Virginia Polytechnic Institute and State University in partial fulfillment of the requirements for the degree of

Doctor of Philosophy

In

Physics

Chenggang Tao, Chair

James Heflin

Hans Robinson

Kyungwha Park

February 19, 2020

Blacksburg, VA

Keywords: Scanning Tunneling Microscope (STM), 2D materials, Transition Metal Dichalcogenides (TMDCs)

STM Study of Interfaces and Defects in 2D Materials

Husong Zheng

Abstract

Two-dimensional (2D) materials show novel electronic, optical and chemical properties and have great potential in devices such as field-effect transistors (FET), photodetectors and gas sensors. This dissertation focuses on scanning tunneling microscopy and spectroscopy (STM/STS) investigation of interfaces and defects 2D transition metal dichalcogenides (TMDCs).

The first part of the dissertation focuses on the synthesis of 2D $TiSe_2$ with chemical vapor transport (CVT). By properly choosing the growth condition, Sub-10 nm $TiSe_2$ flakes were successfully obtained. A 2×2 charge density wave (CDW) was clearly observed on these ultrathin flakes by scanning tunneling microscopy (STM). Accurate CDW phase transition temperature was measured by transport measurements. This work opens up a new approach to synthesize TMDCs.

The second part of the dissertation focuses on monolayer vacancy islands growing on $TiSe_2$ surface under electrical stressing. We have observed nonlinear area evolution and growth from triangular to hexagonal driven by STM subjected electrical stressing. Our simulations of monolayer island evolution using phase-field modeling and first-principles calculations are in good agreement with our experimental observations. The results could be potentially important for device reliability in systems containing ultrathin TMDCs and related 2D materials subject to electrical stressing.

The third part of the dissertation focuses on point defects in 2D $PtSe_2$. We observed five types of distinct defects from STM topography images and measured the local density of states (LDOS) of those defects from scanning tunneling spectroscopy (STS). We identified the types and characteristics of these defects with the first-principles calculations. Our findings would provide critical insight into tuning of carrier mobility, charge carrier relaxation, and electron-hole recombination rates by defect engineering or varying growth condition in few-layer 1T-$PtSe_2$ and other related 2D materials.

STM Study of Interfaces and Defects in 2D Materials

Husong Zheng

General Audience Abstract

Since the discovery of graphene in 2004, two-dimensional (2D) materials have attracted more and more attentions. When the thickness of a layered material thinned to one or few atoms, it shows interesting properties different from its bulk phase. Due to the reduced dimensionality, interfaces and defects in 2D materials will significantly affect the electronic property and chemical activity. However, such nanometer scale features are several orders of magnitude smaller than the wavelength of visible light, which is the limit of resolution for optical microscope. Scanning tunneling microscope (STM) is widely used in study of 2D materials not only because it can provide the topography and local electronic information at atomic scale, but also because of the possibility of directly fabricate atomic scale structure on the surface**.**

The first part of the dissertation focuses on the synthesis of 2D $TiSe_2$ with chemical vapor transport (CVT). $TiSe_2$ belongs to the transition metal dichalcogenides (TMDCs) family, showing a sandwiched layered structure. When the temperature goes down to 200K, a 2×2 superlattice called charge density wave (CDW) will show up, which is clearly observed in our STM images.

The second part of the dissertation focuses on monolayer vacancy islands growing on $TiSe_2$ surface controlled by electrical stressing. During continuous STM scanning, we have observed nonlinear area growth of the vacancy islands. The shape of those islands transfers from triangular to hexagonal. We successfully simulated such growth using phase-field modeling and first-principles calculations. The results could be potentially important for device reliability in systems containing ultrathin TMDCs and related 2D materials subject to electrical stressing.

The third part of the dissertation focuses on defects in 2D $PtSe_2$. We observed five types of distinct defects in our STM topography images. By comparing them with DFT-calculated simulation images, we identified the types and characteristics of these defects. Our findings would provide critical insight into tuning of carrier mobility, charge carrier relaxation, and electron-hole recombination rates by defect engineering in few-layer 1T-$PtSe_2$ and other related 2D materials.

Table of Contents

Chapter 1. Introduction

Two-dimensional (2D) materials refer to crystalline materials with thicknesses on the atomic scale. Graphene, a monolayer of graphite, is the first discovered 2D material. After that, a lot more members in this family are found and studied. In this chapter I will briefly introduce the recent works in 2D materials. Including those important 2D materials, how to grow them, the defect study in 2D materials, and applications based on 2D materials. My research was mainly focused on 2D transition metal dichalcogenides.

1.1. 2D Materials

In 2004, Andre Geim and Konstantin Novoselov exfoliated graphene from bulk graphite using adhesive tape [1], and they were rewarded the Nobel Prize in 2010 for this work. But before that, theorists has started their research long ago. In 1947 Philip Wallace calculated the band structure of monolayer graphite [2], and the result showed that graphene is a zero band gap semiconductor, which means the highest occupied molecular orbital (HOMO) and the lowest unoccupied molecular orbital (LUMO) touch at a single Dirac point. The characteristic linear dispersion relation of electrons in graphene in the vicinity of the Dirac points makes them behave as relativistic quasiparticles with zero effective mass. Graphene has the highest elastic modulus and strength among all known materials [3], it can be stretched by 20% without breaking [3]. For graphite, only 3 carbon atoms in the honeycomb ring can be seen in STM since the electron density for those 3 carbon atoms are higher than the others. However, in graphene you can observe the complete honeycomb structure [4]. Monolayer graphene has a flat absorption of about 2.3% over a broad wavelength range (300 nm to 2500 nm) [5]. In 2008, Kim's group confirmed that the carrier mobility for suspended monolayer graphene on Si/SiO_2 gate electrode is higher than 200,000 $cm^2\ V^{-1}\ s^{-1}$ at electron densities of $\sim 2\ \times 10^{11}\ cm^{-2}$, electric current induced annealing improved mobility up to 230,000 $cm^2\ V^{-1}\ s^{-1}$ [6]. Besides that, graphene also has excellent thermal conductivity. Suspended graphene flake have extremely high thermal conductivity in the range of 3080–5150 $W\ m^{-1}\ K^{-1}$ and phonon mean free path of 775 nm near room temperature [7]. All those amazing properties makes graphene to be the most promising material to replace silicon in

semiconductor industry. Other than mechanical exfoliation, other growth method such as liquid-phase exfoliation [8], thermal decomposition on SiC substrate [9] and CVD growth on metal substrate [10] are also being used to prepare graphene. On the other hand graphene is an ideal substrate to synthesis other 2D materials. Although lacking band gap is a weakness, the good electrical conductivity makes it a perfect platform for electrical devices. Band gap can be opened by defect engineering or doping [11]. On the other hand, defects and doping can also create active sites for catalytic activity [12]. Building heterostructures with other 2D materials not only overcomes some limitations of graphene-based materials, but also allows us to realize novel properties [13]. Graphene has a lot of derivatives, such as hydrogenated graphene (graphane), fluorographene, hydroxygraphene (graphol), and graphene acid [14]. Those derivatives are of great interest to 2D materials research. A lot of study has been focused on the potential applications on graphene based materials, such as field-effect transistor, lithium battery and photovoltaic cell [15-17]. Graphene is also a promising material in biomedical applications, including drug delivery, biosensing and tissue engineering [18].

Hexagonal boron nitride (h-BN) is an analogue of graphite. Bulk h-BN has similar structure of graphite and can also go down to 1 atom layer thickness. Unlike graphene, 2D h-BN is an insulator with a band gap depending on the thickness. It also possess excellent chemical and thermal stability. Due to its large band gap most application studies focus on photo detectors [19]. However, it has been widely used as dielectric substrates for other 2D materials, especially graphene since they share the same structure and the lattice mismatch is only 1.6% [20].

Black phosphorus is a layered semiconductor allotrope of phosphorus. Bulk black phosphorus was first synthesized by applying high temperature and pressure on white phosphorus in 1914 [21]. Monolayer black phosphorus has 1.5 eV direct band gap at Γ point. Due to the interlayer interactions, band gap decreases with thickness, eventually goes to 0.3 eV for bulk black phosphorus. The electrical property and structure of black phosphorus is very sensitive to pressure. At atmosphere it is an orthorhombic phase semiconductor. But at 5 GPa it changes to rhombohedral phase semimetal. When the pressure is further increased to 10 GPa, simple cubic phase will form [22]. Black phosphorus has been widely studied in devices such as field-effect transistors [23] and optoelectronic devices [24].

Transition metal dichalcogenides (TMDCs) are a big family with over 40 different types of metal and chalcogen combinations, each TMDC layer consists of three layers of metal (e.g. Mo, Nb, W) and chalcogen atoms (e.g. S, Se) [25]. Each transition metal atom is bonded to 3 top chalcogen atoms and 3 bottom chalcogen atoms. There are 3 common polytypes for TMDCs, called 1T, 2H and 3R. The number related to the number of layers repeated in each unit cell. And T, H and R means trigonal, hexagonal and rhombohedral respectively. 1T polytype has octahedral structure in which the top layer chalcogen atoms are rotated 60 degree compared with the bottom layer. 2H and 3R polytypes have trigonal prismatic structure in each sandwich layer, which means the top and bottom chalcogen layer share the same pattern. The difference between 2H and 3R polytypes is the stacking order. The electronic properties for TMDCs vary from semiconductor to semimetal, which gives them great advantage in electronic devices compare with graphene.

$TiSe_2$ is one of the widely studied 1T-TMDCs because of its interesting band structure. The band structure near Fermi surface is governed by a Se 4p valence band around the Γ point and a Ti 3d conduction band at the L point. However, the debate on whether $TiSe_2$ is a semimetal or a semiconductor with a very small indirect energy gap exists since 1960s, and still hasn't drawn a clear conclusion. Early optical experiment suggested that $TiSe_2$ is a semiconductor with 1-2 eV band gap [26]. In 1976, Salvo et al. measured the electronic transport property and claimed it to be a semimetal [27]. Li et al. claimed that the optical microscopy confirmed its metallic property [28]. Rasch et al. claimed that the ARPES analysis unambiguous proofed that $TiSe_2$ shows undoubtedly semiconducting behavior [29]. Another interesting property is, when the temperature decreases to 200K, $TiSe_2$ undergoes a phase transition into a $2 \times 2 \times 2$ periodic charge density wave (CDW) phase. A charge density wave means periodically modulated charge density in low dimensional materials. The first theoretical explanation of CDW mechanism is suggested by Peierls in 1930s [30]. Some theoretical works suggest that the CDW transition is driven by a purely electronic instability caused by its unique band structure [31]. However, CDW exists in many kind of materials, including several kinds of TMDCs. I will show the detail discussion about CDW and the CDW studies in TMDCs in Chapter 3.

Another 1T phase TMDC member $PtSe_2$ is a type-II Dirac semimetal. Among all the TMDs, $PtSe_2$ has the highest Seeback coefficient good for thermoelectric applications and the extremely high mobility, up to 3000 $cm^2/V/s$ [32]. Monolayer $PtSe_2$ has potential in building efficient gas sensors

because of its low adsorption energies for gases like NO, CO, CO_2 and H_2O [33]. DFT calculations and angle-resolved photoemission spectroscopy measurement showed that monolayer $PtSe_2$ is a semiconductor with an indirect bandgap of ~1.20 eV [34]. A tunable bandgap can be achieved by varying the thickness of $PtSe_2$ film. Such layer-dependent band structure can also be found in other TMDC materials. For example, Bulk MoS_2 has an indirect band gap of 1.3 eV, which would increase to 1.8 eV if the thickness is reduced to monolayer. Also the band gap changes to direct band gap, which would great enhance the photoluminescence intensity [35]. Therefore, reliable method to grow large sacale, high purity and crystal quality atomic thin TMDCs is required for 2D-TMDCs research.

1.2. 2D Materials Synthesis

As mentioned before, mechanical exfoliation was the first technique introduced to produce graphene in 2004 [1]. This easy and low-budget technique is still widely used in research purpose to obtain high quality graphene. However, the size of each flake is only 5-10 micrometer and the thickness is not uniform. In 2011 Jayasena et al. built a lathe-like experimental setup to cleave large and uniform graphene. An ultrasharp diamond wedge is aligned carefully to the highly oriented pyrolytic graphite (HOPG) to cleave graphite flakes. The flakes have thickness of tens of nanometers [36]. Similar to graphene, 2D-TMDCs can also be produced by mechanical exfoliation. Actually the history of peeling off thin film from TMDC bulk is even longer than graphene. In 1966 Frindt used the adhesive tape to liberate MoS_2 thin films from bulk MoS_2 crystal. The thinnest thickness he got is 1.5 nm, which agreed with the thickness of bilayer MoS_2. Mak et al. used mechanical exfoliation method to prepare 1-6 layers MoS_2 on SiO_2 substrate. The PL spectra confirmed that the band gap increased with decreasing thickness and the indirect band gap peak disappeared in monolayer MoS_2. The disadvantage for mechanical exfoliation method is, the size of the flakes are usually ~20 μm, and the thickness is uncontrollable. Desai et al. improved the mechanical exfoliation method with the help of Au film and successfully obtained large scale flakes with lateral dimensions up to ≈ 500 μm.

Liquid exfoliation is another common method growing 2D-materials. In 2008, Coleman et al. first reported liquid exfoliation of graphite by sonication. They dispersed graphite powder in organic

solvents and sonicated the solution [36]. The existence of monolayer graphene was confirmed by TEM. This method can be used to prepare TMDC as well. Joensen et al. soaked MoS_2 in a 1.6M solution of n-butyl lithium in hexane for 48 hours in argon atmosphere. Then immersed it in water and followed by ultrasonication. MoS_2 layers were separated in the solution and X-ray diffraction confirmed the existence of monolayer MoS_2 [37]. However the interactions with lithium would induce a 2H-1T' phase transition [38]. Also the monolayer concentration is relatively low [39].

Due to the instability of Si atoms at interface, it is possible to sublimate them from SiC surface, leaving graphene on the top of it. The thickness depends on the annealing time and temperature [40]. Similar to growing graphene on SiC(0001) substrate by directly annealing, TMDCs can be directly sulfurization (or selenization) on the transition metal or transition metal oxide under chalcogen atmosphere. In 2012 Lin et al. first thermal deposited MoO_3 on sapphire substrate, then annealed at 1000℃ with sulfer precursor for 15 min. After that, the MoS_2 film was transferred to SiO_2 substrate. The TEM characterizations confirmed that these films are polycrystalline MoS_2 films [41]. However, although this method can grow wafer size TMDC film, the grain size is limited to 10-20 nm due to the amorphous nature of the transition metal substrate.

CVD method is the most widely used synthesis method for high quality, large area 2D materials. When precursor gases pass through the substrate in furnace, they are reacting and deposited onto the surface. In 2006 Somani et al first reported synthesis of few-layer graphene by CVD method [42]. Since then CVD became the most successful method for synthesis large area graphene. By annealing the metal substrate with methane (CH_4) in a hydrocarbon gas ambient at high temperature, carbon source will decompose and form graphene on the substrate. Other than methane, a lot of other gas, liquid, and solid precursors have been used for CVD graphene synthesis, such as ethylene (C_2H_4), acetylene (C_2H_2), toluene (C_7H_8), polystyrene and polymethyl methacrylate (PMMA). A lot of transition metals, such as Ni, Pd, Ru, Ir and Cu, have been used as the substrate for CVD grown graphene due to their catalytic activity during the decomposition of carbon source. The best substrate for growing monolayer graphene is Cu due to the self-limiting effect of carbon atoms (another reason is, commercial Cu foils are relatively cheaper than other metals). CVD growth graphene on other metal substrates such as Ni and Co usually results in multilayers because of the dissolution and precipitation of carbon from the surface during cooling down. For example, despite the high decomposition temperature of methane (>1200℃), graphene

can grow on Pt at as low as 750℃ [43]. Pressure is a key factor during graphene growth. It has been reported that reducing the pressure down to 20 mbar during the annealing stage could increase the quality and uniformity of graphene [44]. Due to the increasing sublimation of Cu under low pressure, the surface became smoother. Temperature is critical for growing high quality graphene. The growing temperature varying from 800℃ to 1100℃ depending on different metal substrates. Usually higher temperature can reduce the density of graphene nuclei during growth. However, more evaporations caused by higher temperature would also promote the roughness. Geng et al. reported that graphene grew on liquid Cu (>1084℃) can significantly reduce the nucleation process in graphene CVD system [45]. The average grain size is up to 120 μm using 1160℃.Graphene grown by this method can be easily transferred to other substrates since the metal substrate can be etched by acid like HCl or $FeCl_3$.

This method was also used to grow all kinds of TMDCs. The most straightforward method is to first deposit metal/metal oxide film on the substrate then put it at the downstream of chalcogen powder in a annealing furnace. Wafer scale TMDC film can be produced with this method. However, the TMDC film is polycrystalline with very small grain size (<20 nm) due to the amorphous metal/metal oxide film. To grow TMDC films with larger grain size, vapour phase transition metal source is required. Lee et al. used CVD method successfully prepared large grain monolayer MoS_2. They first put MoO_3 and S powder separately in two crucibles and the SiO_2 substrate facing down on the upper side of MoO_3 power. Then anneal the chamber at 650℃ for 15 min under nitrogen flow. Vapour phase MoO_3 diffused to the SiO_2 and sulfurized on the substrate to produce MoS_2 film. The grain size for monolayer MoS_2 island was up to 20 μm [46]. Other TMDC such as WS_2, WSe_2 and $MoSe_2$ can be obtained with similar method [47-49]. However, for those transition metal oxides that have high melting points, the CVD method is not viable since it is hard to vaporize them.

Despite the high melting point, some transition metal can be volatilized in the form of a gaseous reactant at relatively low temperature with the help of the transport agent. Then the volatile transition metal reactant will recrystallize on the substrate at even lower temperature. This method is called chemical vapor transport. Chemical vapor transport has long been used for growing TMDC bulk [50,51]. By properly choose the growth parameters, CVT method can be used to growth high quality layer controllable TMDC films. $NbSe_2$ and $TiSe_2$ have been grown with CVT

method. For growth $NbSe_2$ film, NaCl is used as transport agent and mixed with NbO_x powder putting at the downstream of Se powders annealing at 795℃ [52]. For growth $TiSe_2$ film, high quality large grain size $TiSe_2$ film can be synthesis with the help of AgCl, I'll talk about the details in Chapter 3. Other transport agent such as LiCl has also been studied for growing $TiSe_2$ [53].

1.3. Defects in 2D Materials

The electronic states at the edges and defects in 2D materials are different from the bulk, usually significantly more active. A variety of defects could generated during synthesis. Due to the second law of thermodynamics the presence of defects is inevitable. Intrinsic defects such as vacancies, intercalation and substitutional atoms would be formed due to the nonuniform growth, especially in CVD growth. Impurities and oxidation will also bring in defects during and after growth. The formation of defects can be controlled by many methods, including high temperature treatment, chemical reduction and ultraviolet irradiation [54]. Chemical, optical properties and electrical conductivity of 2D materials are sensitive to defects. Understanding the nature of defects in critical for the development of 2D devices. There are several kinds of common defects in 2D materials: vacancies, substitutions, intercalations, adatoms, and line defects such as grain boundaries [54].

Missing atom is the simplest kind of defect. Single point vacancies in graphene were first observed in 2008 by TEM [55]. The honeycomb lattice break into a 5 membered and 9 membered ring. El-Barbary et.al calculated the formation energy for a single vacancy is about 7.5 eV, the formation energy for double vacancies (two neighboring vacancies) is about the same as a single vacancy(8.5 eV) [56], which makes it more favored to diffuse. And Kim et al. observed the dynamic structure of double vacancies in graphene under TEM scanning [57]. Due to similar synthesis processing, vacancies are unavoidable in TMDCs as well. For TMDCs, there are 2 types of vacancies: transition metal vacancy and chalcogen vacancy. Both kinds of defects can be observed in many kinds of TMDCs [58-61]. Usually chalcogen vacancy has lower formation energy. For 2D MoS_2, the formation energy for S vacancy is 1.2 eV (3 eV) in Mo (S) rich condition [58]. Those defects are stable in room temperature. However, Komsa et al. found that chalcogen vacancies would diffuse on the surface and agglomerate into line defects under the electron beam [62]. Vacancy

defects can be created by ion irradiation, field evaporation, oxygen plasma treatment and hydrogen annealing [63-65].

Another type of defect in is doping. Doping elements are either coming from the impurities or intentionally added during growth. Doping can significantly change the carrier density, even carrier type, which is of importance for gap engineering [66-68]. For graphene, after nitrogen doping in the monolayer graphene, the Fermi level shifts above the Dirac point and thus opens a band gap, which makes it more promising in semiconductor devices [69]. Compare with Graphene, doping is more widely used in TMDCs. For instance, due to the similar structure and synthesis temperature, the $Mo_{1-x}W_xS_2$ compounds can significantly tune the band gap and other electronic properties [70]. Similar studies on S/Se alloying are also being reported [67,71]. Nb substituted MoS_2 shows P-type semimetal property, on the other hand alkali metals can make the MoS_2 n-type. Other chalcogen dopant elements (such as N, P) have also been studied in MoS_2 [72]. If the dopant atoms cannot match with the 2D material crystal structure. They will prefer to intercalate between layers rather than substitute the existing atoms. Sugawara et al. deposited Li on bilayer graphene and observed the $\sqrt{3} \times \sqrt{3}$ R30 ° superstructure in LEED pattern, confirming that Li atoms are intercalated between the graphene layers [73]. Kühne et al. observed the diffusion of Li in bilayer graphene [74]. The measured diffusion coefficient is up to 7×10^{-5} cm^2 s^{-1}. Ichinokura et al. found that if Ca atoms were deposited on Li intercalated bilayer graphene at 150 ℃, the intercalated Li atoms would be replaced by Ca atoms. Ca intercalated bilayer graphene showed superconductivity behavior at 4K, and the resistance completely drop to 0 at 2K [75]. However, intercalation of even larger molecules would result in the exfoliation of graphene, which is actually being used for exfoliating graphene from graphite in liquid exfoliation. Intercalation exists in 2D TMDCs as well, and can be used to alter the property of TMDCs. For example Li intercalation could enhanced the hydrogen evolution reaction of MoS_2 by transforming the 2H phase to 1T phase [76]. Dopant atoms could also just absorb on the surface as adatoms. For graphene, the lowest energy position for a carbon adatom is the bridge configuration rather than the center of the hexagon. Local density approximation study shows that the binding energy is about 1.4 eV, and the diffusion barrier is 0.47 eV [77], which means carbon adatoms migrate easily at room temperature. That's why we cannot observe such defects with STM/AFM. The binding energy for metal adatoms are even lower (<1 eV) [78]. It is hard to observe such migration. Actually metal

adatoms are more likely to be trapped on surface defective sites [79]. A biaxial strain of 1% will lower the adsorption energy by about 0.1 eV for metal atoms. For TMDCs, the metal adatoms are also highly mobile and prefer to locate on vacancy sites. Pt adatoms would jump between nearby S vacancies on MoS_2 surface under STEM scanning [80]. Co adatoms on MoS_2 have been studied as well. Co atoms are also favorable staying at S vacancies, but can be observed at either the top of Mo or the hollow center of the ring [81].

During epitaxial growth of 2D materials, when two clusters merge together, grain boundaries would form on the interface due to the mismatch of crystal cells. The optical and electric properties vary a lot in grains and grain boundaries. Huang et al. measured the resistance of graphene and their result showed that the resistance of grain boundary is reduced to one third of the grain [82]. Yazyev et al. calculated the density of states on the graphene grain boundary and found van Hove singularities around the Fermi level [83]. Zande et al. used photoluminescence mapping showing that the PL intensity quenched on mirror boundary, while on tilt boundary the PL emission is enhanced by 100% [84]. Grain boundaries in TMDCs are more complicated due to the sandwich structure. $MoSe_2$ grown by molecular beam epitaxy method will form twin grain boundaries. Such grain boundaries show metallic behavior thus can be easily observed by STM [85]. The grain boundaries in MoS_2 they are still semiconducting, but the gap is reduced by 0.85 eV [86].

1.4. 2D Materials Applications

Field effect transistor (FET) is the most basic electronic device based on 2D materials. Pristine graphene cannot be directly used for FET devices due to the lack of band gap. However, Nitrogen-doped graphene is a typical n-type semiconductor. Wei et al. prepared bottom gated field-effect transistors with N-doped graphene, and meatured the mobilities are about 200-450 $cm^2V^{-1}s^{-1}$. Other 2D materials such as TMDCs have band gap naturally. The first FET based on Monolayer MoS_2 was builded by Kis's group in 2010 [87]. Monolayer MoS_2 was prepared by mechanical exfoliation method and then transferred to 270 nm SiO_2/Si substrate. 50 nm gold was deposited on the sample using electron beam lithography. After that, 30 nm Hf_2 film was deposited as the top gate dielectric. Finally another gold contact was applied on the top as the top gate. The mobility is ~ 200 $cm^2\,V^{-1}\,s^{-1}$, which is comparable to graphene nanoribbons. The on-off ratio is larger than 1

$\times 10^8$. A similar designed FET made by monolayer WSe_2 was reported by Fang et al. [88], which exhibited mobility of ~250 $cm^2\ V^{-1}\ s^{-1}$ and ~10^6 on-off ratio. Pradhan et al. analyzed few layers $MoTe_2$ based FET and obtain an on-off ratio ~10^6 which is similar to the MoS_2 without dielectric layer. Unlike the electron-doped MoS_2 FET, $MoTe_2$ FET was observed to be hole-doped. Few layer $PtSe_2$ FET in a back-gated configuration showed 210 $cm^2\ V^{-1}\ s^{-1}$ room-temperature electron mobility, which is comparable to black phosphorus, but has much better air stability [89].

Monolayer graphene can absorb as much as 2% light in a wide wavelength range. Xia et al. built ultrafast photodetector with mono or few layers graphene [90]. The detection bandwidth could exceed 500 GHz. In 2009 Mueller et al. observed strong photoresponse at 0.514 μm, 0.633 μm, and 2.4 μm wavelength. The maximum photoresponsivity they measured is 6.1 mA/W [91]. However, due to the lacking of band gap, the photoresponsivity of graphene based photodetector can not be further increased. On the other hand, many of the TMDCs change from indirect to direct bandgap when the thickness is reduced to a monolayer, which results in a 10^4 increase in PL intensity [35]. Yin et al. fabricated the first monolayer MoS_2 phototransistor [92]. They reported a photoresponsivity of 7.5 ma/W and a response time within 50 ms. After that, other monolayer or few layers MoS_2 photodetectors based on mechanical exfoliation or CVD growth MoS_2 have been reported with the best photoresponsivity over 880 A/W [93,94]. Photodetectors using a few layer $PtSe_2$ exhibit a wide range of absorption. Highest photocurrent up to 9 μA was obtained under the laser wavelength of 408 nm. This device also can maintain a high photoresponse after 1000 bending cycles [95]. Photodetector based on $PtSe_2$/CdTe heterostructure has a wide detection ranging from deep UV to near-infrared. This photodetector also shows a high responsivity (506.5 mA/W), a high specific detectivity(4.2×10^{11} J), a high current on/off ratio (7×10^6), a fast response speed (8.1/43.6 μs), and excellent repeatability, stability at room temperature [96]. Other $PtSe_2$ heterostructure like $PtSe_2$/perovskite, $PtSe_2$/silicon nanowire and $PtSe_2$/GaAs heterojunctions also shows great potential in high-frequency optoelectronic devices [97-99].

The high transparency, high conductivity and high chemical resistance of graphene makes it a perfect transparent conductive electrodes for photovoltaic. Compare with traditional indium tin oxide electrode, the flexibility of graphene makes it possible for flexible organic solar cells. Furthermore, graphene can be used as charge acceptor material as well. In 2008 Cheng et.al. employed graphene acceptor combined with P3HT and P3OT as electron donor. The highest

powerconversion efficiency is 1.4% [100]. Other than graphene, many TMDCs also shows photovoltaic potential. The bulk phase TMDC photovoltaic effect has been studied long ago. In 1982 Fortin et al. reported the PV efficiency in bulk MoS_2 is about 1% [101]. Theoretical calculation showed that monolayer TMDCs has a high absorbance of 5-10%, which is one order higher than Si and GaAs, making them perfect candidate for ultrathin solar cell [102]. Tsai et al. reported that monolayer MoS_2/Si heterojunction solar cells exhibited a power conversion efficiency of 5.23% [103]. Lin et al. demonstrated that the efficiency of MoS_2/GaAs heterostructure solar cell would increase from 4.82% to 5.42% by inserting h-BN interlayer, which can be further increased to 9.09% by employing chemical doping and electrical gating [104].

Gas sensors play an important role in our daily life. For example, monitoring the air quality or detecting toxic wastes. 2D materials show great potential in gas sensing technologies due to the high surface to volume ratio. Graphene is a promising gas sensing material since its electronic propertie is strongly affected by the adsorbing molecules. The interaction between graphene and gas molecules vary from van der Waals to covalent bonding, such interactions will change the electronic structure of graphene and therefore change the resistance. Schedin et al. built the first graphene gas sensor in 2007. They found that the adsorbed molecules change the local carrier concentration one electron by one electron, which leads to step-like changes in resistance [105]. The main disadvantage for graphene gas sensor is the long recovery time since the gas molecules are strongly absorbed on the surface. Yavari et al. improved the revovery time using joule-heating method to desorb gas molecules [106]. Another disadvantage for graphene gas sensor is the poor selectivity, which can be improved by graphene–metal oxide hybrids gas sensor. For example, SnO_2 nano crystal decorated reduced graphene oxided (RGO) enhanced sensitivity to NO_2 (from 2.16 to 2.87), but reduced ensitivity to NH_3 (from 1.46 to 1.12) [107]. Liu et al. showed that ZnO–RGO hybrids gas sensors have higher sensitivity and shorter response time for detecting NO_2 than RGO itself [108]. Recently another 2D material family TMDCs also draw a lot attention. Cho et al. produced few layered MoS_2 gas sensor via CVD method. This device showed excellent sensing sensitivity (down to 120 ppb) and fast response time (<500 ms). However, the recovery time was long [109]. Late et al. reported single layer $MoSe_2$ gas sensor which comprehensible detection of NH_3 gas down 50 ppm with fast response (∼150 s) and recovery (∼9 min) at room temperature [110].

2D materials could be promising candidates in alkali ion battery. Graphene is considered to be the perfect additive for cathode material in lithium ion battery due to its perfect conductivity and high surface/mass ratio. Su et al. reported that when 2% of carbon black was replaced with graphene in $LiFePO_4$/carbon composite, the charge transfer resistance reduced from 330 Ω to 110 Ω [111]. Improved conductivity could also increase the cyclability and rate capability of the materials. Zhou et al. reported that compare with $LiFePO_4$/carbon composite, $LiFePO_4$/graphene oxide and graphene modified $LiFePO_4$/carbon composite showed way higher discharge capacity and better cycling performances [112]. TMDCs, on the other hand, draw more intention in sodium ion battery. Sodium ion battery is the most promising alternatives to lithium ion battery due to the abundance and lower cost of sodium resources. However, traditional graphitic carbon materials cannot store large amount of sodium. Sodium intercalated in TMDCs usually shows way better capacity and mobility due to the larger interlayed space. Liu et al. reported that TiS_2 nanoplates delivered a large capacity (186 mAh/g) and high rate capability (100 mAh/g at 10 C) at both low and high current rates based on reversible intercalation/ deintercalation of sodium ion [113]. Zhang et al. reported that ultrasonication $TiSe_2$ nanosheets delivered high capacity (147 mAh/g), good rate capability (110 mAh/g at 5 C, 105 mAh/g at 10 C), and great cycling performance [114]. Theoretical calculation showed that $TiSe_2$ might also be an excellent cathode materials for Mg-ion and Ca-ion battery [115]. Besides, $TiSe_2$ can significantly improve the capacity of TiO_2-carbon nanofiber anode for lithium/sodium battery [116].

1.5. Layout of the Dissertation

In chapter 2 I'll introduce the background knowledge about our main experiment method STM. I'll first use quantum tunneling barrier to show how the tunneling current works. Then I'll demonstrate the relationship between dI/dV curve and local density of state to show the importance of tunneling spectroscopy. Followed by description on the design of our STM. Then talk about how STM can be used to modify the surface.

In chapter 3 I'll introduce the new synthesis method of $TiSe_2$ film by CVT method. CVT method is widely used to growth all kind of bulk TMDCs. By properly choose the parameter, such as

substrate, transfer agent, growing temperature, and heating up and cooling down rates, ultrathin $TiSe_2$ films ~10 nm can also be prepared. A CDW state with 2×2 superstructure was clearly observed on these ultrathin flakes by STM, and the phase transition temperature of these flakes was investigated by transport measurements, confirming the existence of CDW states. Our work opens up a new approach to synthesizing 2D CDW and superconductive TMDCs for exploring new fundamentals and applications in novel electronics.

In chapter 4 I'll talk about the vacancy island growth on $TiSe_2$ surface induced by STM electrical stressing. During growth we obserbed a non-linear growth rate also the shape of each triangle evaluated to hexagonal shape. We used phase field modeling to simulate this process and quantified a parabolic growth rate dependence with respect to the tunneling current magnitude. The results could be potentially important for device reliability in systems containing ultrathin transition metal dichalcogenides and related 2D materials subject to electrical stressing.

In chapter 5 we investigate intrinsic point defects in ultrathin 1T-$PtSe_2$ layers grown using the CVT method. We observed five types of distinct defects from STM topography images and obtained the local density of states of the defects. By combining the STM results with the first-principles calculations, we identified the types and characteristics of these defects. Our findings would provide critical insight into tuning of carrier mobility, charge carrier relaxation, and electron-hole recombination rates by defect engineering or varying growth condition in few-layer 1T-PtSe2 and other related 2D materials.

Chapter 2. Introduction to Scanning Tunneling Microscopy (STM)

The modern optical microscopes were first developed in 17th century. It is the first time micrometer scaled features are able to be observed. However, due to the diffraction of transmitted light, the limitation of optical microscope's resolution is about half of the wavelength (~200 nm).

Transmission electron microscopy (TEM) was demonstrated by Max Knoll and Ernst Ruska in 1931, and Ruska was awarded Nobel Prize for this work. With the development of scanning transmission electron microscopy (STEM) in 1970s, the resolution can go down to atomic scale. However, TEM requires the sample to be a film thinner than 100 μm. And the high energy electron beam might damage the surface.

STM was invented by Gerd Binnig and Heinrich Rohrer in 1982, and this work won them the Nobel Prize in physics in 1986. The resolution ~0.1 nm for x-y direction and ~0.01 nm for z direction, which means every single atom can be clearly imaged. Due to its non-conduction interaction with the sample, it is able to study surface diffusion and migration by continuous scanning. In this chapter, I will introduce the fundamental physical mechanism and the design of STM.

2.1 Quantum Tunneling Current

Suppose an electron energy E traveling along the x-axis encounters a potential barrier V at 0<x<L. By using Schrödinger's equation, we can get

$$-\frac{\hbar^2}{2m}\frac{d^2\psi(x)}{dx^2} + U(x) = E\psi(x)$$

In which

$$U(x) = \begin{cases} V \text{ for } 0 < x < L \\ 0 \text{ for } x < 0 \text{ and } x > L \end{cases}$$

The answer is in the form of

$$\psi_1(x) = Ae^{ikx} + Be^{-ikx} \quad \text{for } x < 0$$

$$\psi_2(x) = Ce^{-\beta x} + De^{\beta x} \quad \text{for } 0 < x < L$$

$$\psi_3(x) = Fe^{ikx} + Ge^{-ikx} \quad \text{for } x > L$$

Where $k = \frac{\sqrt{2mE}}{\hbar}$ and $\beta = \frac{\sqrt{2m(V-E)}}{\hbar}$

Given the continuity condition at region boundaries

$$\psi_1(0) = \psi_2(0)$$

$$\left.\frac{d\psi_1(x)}{dx}\right|_{x=0} = \left.\frac{d\psi_2(x)}{dx}\right|_{x=0}$$

$$\psi_2(L) = \psi_3(L)$$

$$\left.\frac{d\psi_2(x)}{dx}\right|_{x=L} = \left.\frac{d\psi_3(x)}{dx}\right|_{x=L}$$

and G=0 since there is no reflection wave in x>L region. We can solve the equations

$$\frac{F}{A} = \frac{e^{ikL}}{cosh(\beta L) + i\frac{\gamma}{2}sinh(\beta L)}$$

Where γ =β/k−k/β

And the transmission probability is

$$T = \left|\frac{F}{A}\right|^2 = \frac{1}{cosh^2(\beta L) + \frac{\gamma^2}{4}sinh^2(\beta L)}$$

For $\beta L \gg 1$ case, the transmission probability can be approximated by

$$T = 16\frac{E}{V}(1 - \frac{E}{V})e^{-2\beta L}$$

In this equation we can find out T is proportional to $e^{-2\beta L}$, assuming E << V and using V = 4.5 eV for the work function of tungsten tip. The tunneling probability would decay to 1/9 if the distance is increased by 1 Å. Such high sensitivity ensures the high vertical resolution of STM.

2.2 Scanning Tunneling Spectroscopy (STS)

The total current tunneling from the tip to the sample can be expressed as:

$$I_{ts} = \frac{4\pi e}{\hbar}\int_{-\infty}^{+\infty} |M|^2 \rho_t(E) f_t(E) \rho_s(E+eV)[1 - f_s(E+eV)]\, dE$$

Where e is the electron charge, $\hbar$ is the Dirac constant, E is energy with respect to Fermi energy of the sample, V is Vbias, $f_t(E)$ and $f_s(E+eV)$ are Fermi-Dirac distributions for the tip and the sample, which is given by

$$f(E) = \frac{1}{e^{\frac{E}{k_B T}} + 1}$$

Where k_B is the Boltzmann constant and T is the temperature, $\rho_t(E)$ and $\rho_s(E+eV)$ are the density of states for the tip and the sample. M is the tunneling matrix.

Adding on the small amount of current tunneling in the opposite direction

$$I_{st} = \frac{4\pi e}{\hbar}\int_{-\infty}^{+\infty} |M|^2 \rho_t(E)[1 - f_t(E)] \rho_s(E+eV) f_s(E+eV) dE$$

We get the total tunneling current:

$$I_{total} = \frac{4\pi e}{\hbar}\int_{-\infty}^{+\infty} |M|^2 \rho_t(E) \rho_s(E+eV)\{f_t(E)[1 - f_s(E+eV)] - [1 - f_t(E)] f_s(E+eV)\} dE$$

Using Low temperature approximation, we can treat Fermi-Dirac distribution as

$$f(E) = \begin{cases} 1 & \text{for } E < 0 \\ 0 & \text{for } E > 0 \end{cases}$$

Consequently, the tunneling current can be simplified as:

$$I_{total} = \frac{4\pi e}{\hbar}\int_{-eV}^{0} |M|^2 \rho_t(E) \rho_s(E+eV) dE$$

We can assume ρ_t is constant at certain range since the tip is made of metal, so

$$I_{total} = \frac{4\pi e}{\hbar}\rho_t \int_{-eV}^{0} |M|^2 \rho_s(E + eV) dE$$

The result of derivation would be

$$\frac{dI}{dV} \propto \rho_s(E + eV)$$

Which means the dynamic conductance is proportional to the local density states of the sample.

2.3 STM Design

There are 2 STMs in our lab. One is the first generation Omicron built in 1980s, the other is the latest Omicron low temperature STM (LT STM). However, the basic design of them are the same. I'll use the RT STM as an example to explain the functions of each part of the STM, as shown in Figure 2.1.

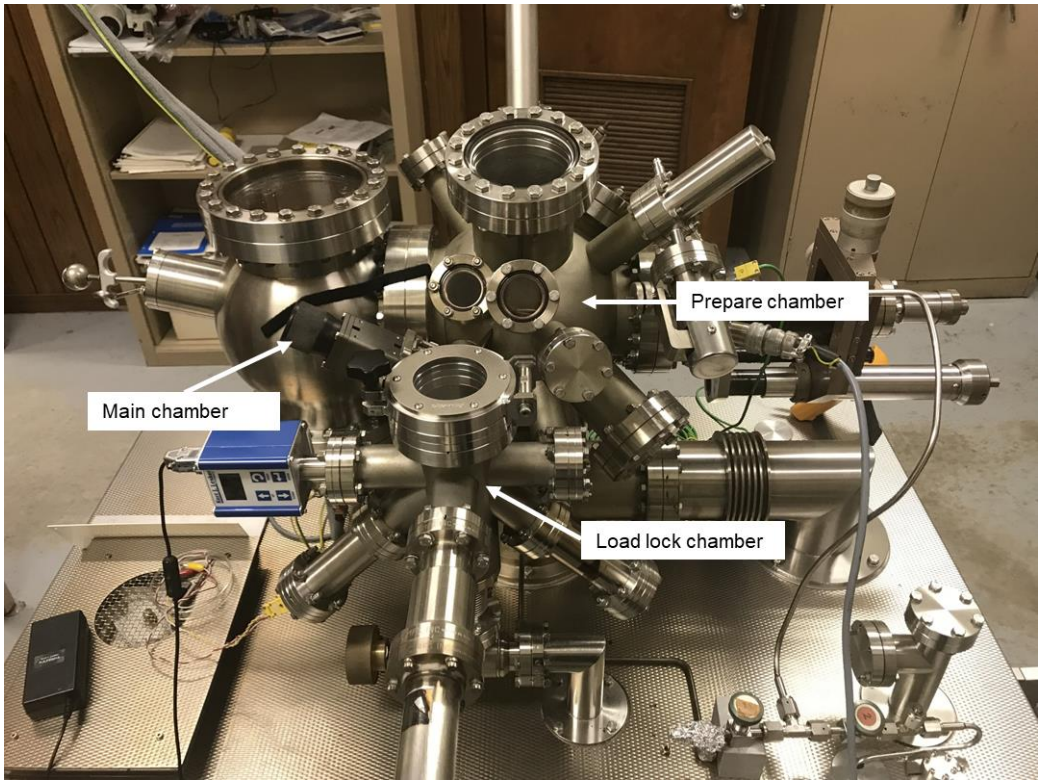

Figure 2.1. Room temperature STM

Before transferring into the main chamber, the sample is first mounted on the magnetic linear driver in the load lock chamber. Load lock chamber is designed for maintaining the UHV in the main chamber, which is critical for getting rid of contamination on the sample and tip. Then a turbo pump will pump this chamber for 4 hours before the sample could be transferred with magnetic linear driver onto the manipulator in the prepare chamber. Prepare chamber is used for preparing the sample such as annealing or sputter annealing, depositing molecules. The filaments on the manipulator can be used to anneal the sample, and accurate temperature can be measured by built-in thermocouple (See Figure 2.2). Usually the sample will be annealed above 100 ℃ for 30 min to 2h in order to degas and clean the surface before finally transferring into the main chamber.

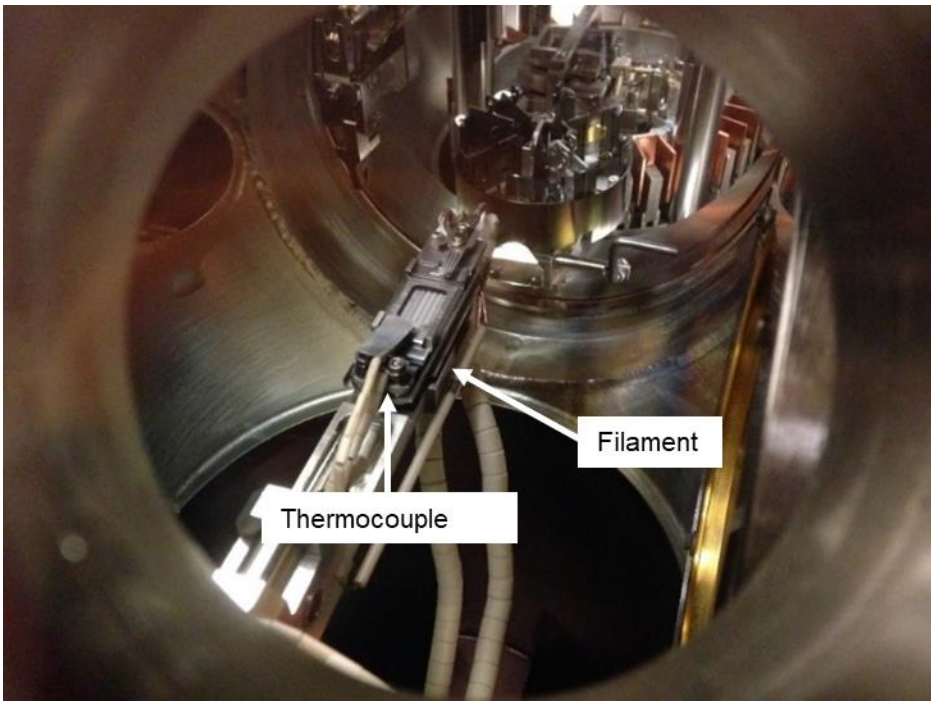

Figure 2.2. Manipulator in prepare chamber

As we mentioned before, tunneling current is sensitive to the distance between sample and tip. During STM scanning, the spacing between the tip and sample is typically 1-10 angstroms. The movement of the tip is achieved by using piezoelectric drives called scanner (See Figure 2.3). As the probe is scanning in horizontal direction (x) and adjusting the height in the vertical direction (z) to maintain a constant current, we can obtain a two-dimensional plot. By displacing the tip in

y direction by a certain amount and repeat such circle, we can establish the three dimensional topography. A good scanner requires high resonance frequencies and high scan speed, high sensitivity, low cross-talk between x, y, and z piezodrives, low nonlinearities and low thermal drifts.

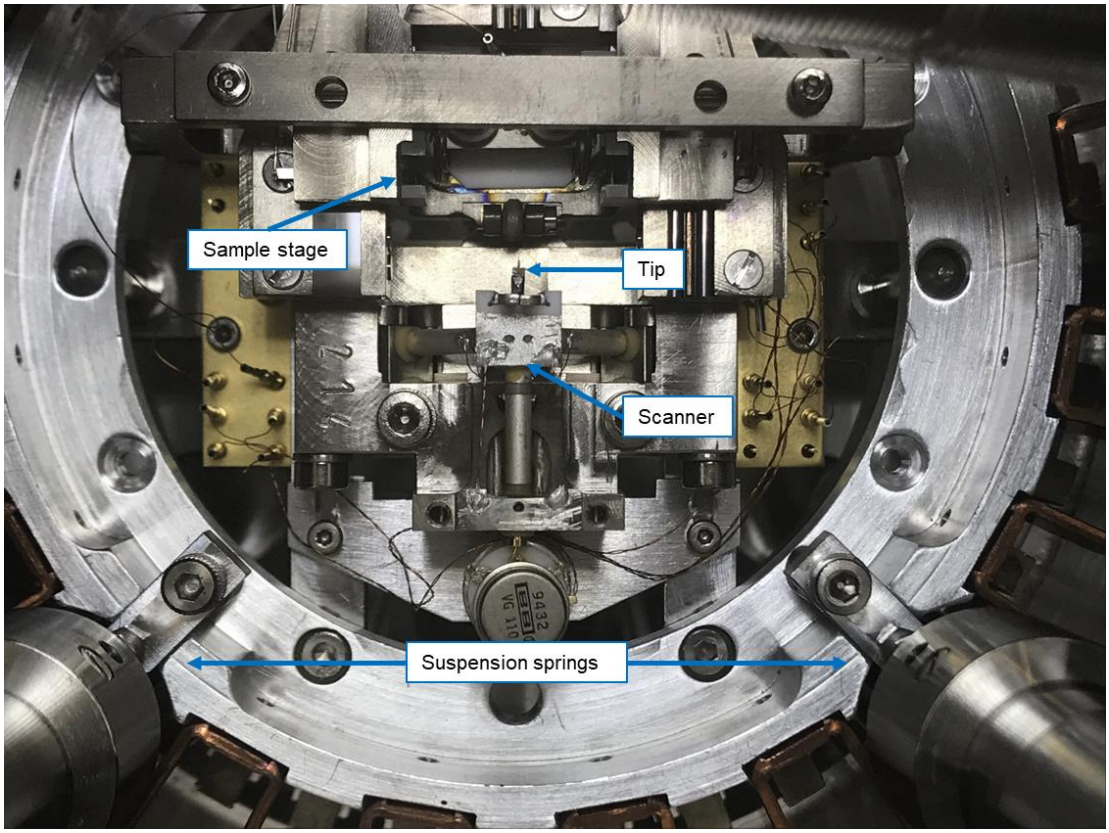

Figure 2.3. Scanning units.

The tip we used in RT-STM is the chemically etched tungsten tip. We use the 2-step methods to fabricate STM tips from tungsten wires with a diameter of 0.25 mm. The tungsten wire was first etching in 5 mol/L KOH solution to get the rough shape, then fine polished in a drop of 0.5 mol/L KOH solution to get the final shape with one single atom at the top. In order to check the quality of a tip, we need to first check it with optical microscope, then try to use it to scan Au (111) sample as the standard sample to test it. The basic requirement for a good tip is that it can resolve the steps clearly in Au surface. A perfect tip can even resolve the herringbone structure on stepped Au at room temperature.

Most of our samples are mounted on tantalum sample plate. We first cut 2 thin tantalum stripes and weld them on the sample plate with Huges model VTA-60 weld head in order to hold the sample on it (See Figure 2.4). A clean and flat sample surface is critical for STM scanning. The dust and oxidation could severely impact the quality of image or even damage the tip. For bulk materials like HOPG or $TiSe_2$ crystal we can use scratch tape to create a fresh cleaved surface. But 2D materials samples should be kept in the vacuum all the time even during transit. We used vacuum mini-chambers to transport and store samples (See Figure 2.5). The chamber itself is sealed by copper flange. After putting the sample in this mini-chamber was directly connected to a mechanical pump and pumping for ~30 min before closing the valve. The pressure inside is lower than 10 mbar and can keep in vacuum for at least a week.

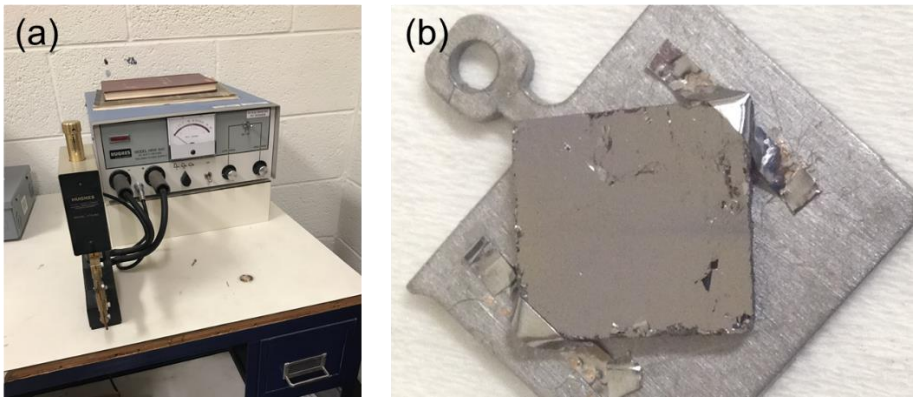

Figure 2.4. (a) Huges model VTA-60 weld head. (b) HOPG sample mounted on the sample plate.

Figure 2.5. Vacuum mini-chambers.

For 2D materials samples that grown on insulator substrate such as mica and SiO_2, we need to deposit electrode to make them conductive to the sample plate. Gold is the most popular choice for its good conductivity and stability despite the cost. For mica and sapphire substrates gold electrode was directly deposited by thermal evaporation through a shadow mask. But for SiO_2 substrate a 5 nm chromium should be deposited first as adhesion layer. Our LT-STM equips a high-resolution microscope. By comparing the real-time image with the optical image we can successfully land the tip on 20 μm size flakes (See Figure 2.6).

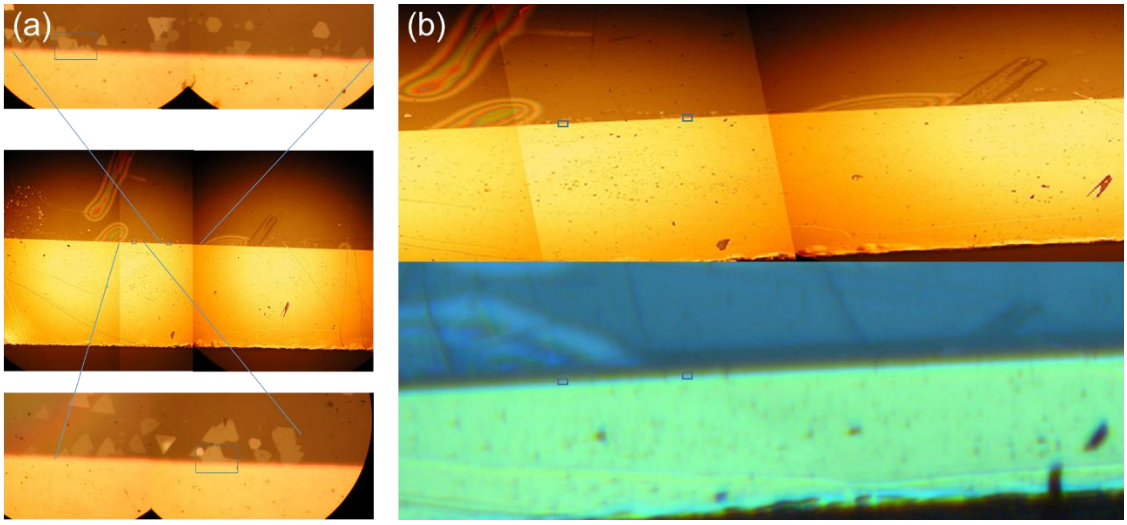

Figure 2.6. (a) Optical image of $PtSe_2$ flakes with gold electrode, both flakes are ~20 μm size. (b) Comparison of optical image taken before scanning and microscope image during scanning.

The electronic part in the STM is critical for reducing electronic noises and feedback loop instabilities. Computer-controlled digital-to-analog converter (DAC) is used to apply bias voltage to the tip or sample, and the range is usually from 1 mV to 4 V. The tunneling current is measured by a preamplifier between the tip and sample with a gain of 10^6-10^9 V/A. The relative error signal between tunneling current and the demanded current (10 pA to 10 nA) will be sent to the feedback amplifiers including a proportional amplifier and an integrator amplifier. This feedback signal will be used to adjust the z position of the tip through the z piezoelectric drive. Computer-controlled DACs with a subsequent high-voltage amplifiers can control scanning the X-Y plane.

As mentioned before, vertical rirection resolution of STM is less than 0.01 nm, which is about 6 orders of magnitude smaller than floor vibration. To achieve the stability for scanning we must introduce in vibration isolation system. The first designed STM used magnetic levitation on a superconducting bowl for vibration isolation, which means it can only work at liquid helium temperature. Later this design was replaced by spring system combined with Viton elements. Our lab is located in the basement in order to get the highest stability. Both RT-STM and LT-STM are mounted on pneumatic feet to further minimum the vibration.

2.4 STM surface alteration

STM is not only a powerful characterization tool, but also a useful method to fabricate atomic scale structure on the surface. In 1990 Eigler et al. used STM to write "IBM" with Xenon atoms on Ni(110) surface [117]. They first placed the tip above a Xe atom. Then increased the tunneling current to ~ 30nA, which made the tip-atom interaction strong enough to allow the Xe atom sliding on the surface without desorbing from it. Then moved the tip to target location and finally withdrew the tip by decreasing the tunneling current. In 1993 they used the same method built a "quantum corrals" with 48 Fe atoms on Cu(111) surface [118]. Since electrons were refined in a 12.4 nm ring, they would format a two-dimensional electronic gas standing waves within the corral. By measuring the periodicity of the standing wave, they determined that the effective mass of electrons states to be about 0.37 m_e, which is in consist with other reports.

Aside from modifying atoms on sample surface, STM can also do lithography on the surface of the sample by applying a significantly higher bias potential or a bias pulse. In 2008 Levente et al. employed STM lithography to cut graphene nanoribbons on a graphene flake [119]. The graphene nanoribbons were fabricated by moving the tip with a constant velocity of 1 nm/s at 2.28 V tip bias. With the high resolution of STM thinnest graphene nanoribbons down to ~2.5 nm can be fabricated with designed armchair or zig-zag edge. And STS measurements showed that the band gap was about 0.5 eV.

STM imaging was found to alter the surface of TMDCs for a long time. In 1991 Akari et al. first applied a 4-6 V sample bias pulse on WSe_2 surface to create a 5-nm diameter cluster. After continuous scanning for 20 minutes the shape transformed to an equilateral triangle vacancy and the sides of the triangle increased to ~75 nm [120]. Boneberg et al. did similar experiment and found that the edges of triangle vacancies increased linearly [121]. They also found that no growth could be observed in high vacuum or dry O_2/N_2 environment, suggesting that a thin water film is critical for the growth. However, Yamaguchi et al. showed that surface etching on 1T-TaS_2 can also be performed in high vacuum, although much slower than in ambient air, suggesting that the electrostatic interaction itself contribute most in the etching mechanism [122]. Hosoki et al. wrote atomic scale "PEACE '91 HCRL" on MoS_2 surface. They first positioned the tip 0.3 nm above a

Se atom then applied a 5 V and 70 ms pulse to kick it out. After repeating this process for hundreds of time the designed pattern was written on the surface [64].

Chapter 3. Controlled Synthesis of Two-Dimensional 1T-$TiSe_2$ with Charge Density Wave Transition by Chemical Vapor Transport

This work is published on Journal of the American Chemical Society [123]. In this work I did the STM scanning for room temperature large scale images and low temperature CDW images in figure 3.9, wrote the part of the "Result and Discussion" and "Conclusion" sections that related to STM.

3.1 Introduction

A charge density wave means periodically modulated charge density in low dimensional materials. The first theoretical explanation of CDW mechanism is suggested by Peierls in 1930s [30]. Consider a quasi-one-dimensional metal atoms, the lowest energy state requires a uniform lattice constant a. However, if a period lattice distortion $\lambda = \frac{\pi}{k_F} = 2a$ is applied as a periodic potential perturbation, a new Brillouin zone at $\pm k_F$ will be created and thus open a new energy gap at $k = \pm k_F$. The energies of the occupied states below E_f will be lowered due to the gap, which means a reducing in the total electronic energy.

At low temperatures, the elastic energy cost of the atomic distortion is less than the gain in conduction electron energy, so the CDW state is preferred. At high temperatures the CDW state will go back to metallic state due to the reducing of electronic energy gain. The phase transition between the metallic and CDW states is known as the Peierls transition.

For high dimension case, the situation is more complicated since the Brillouin zone edges only partly coincide with the Fermi surface. Only the systems with stronger interactions (or quasi 1D bands) can have weak Fermi surface nesting. CDW has been observed in many kinds of TMDCs such as $TaSe_2$, $NbSe_2$, $TiSe_2$, and TaS_2. However, angle-resolved photoemission spectroscopy (ARPES) studies and electronic structure calculations show that CDW in TMDCs is complicated than Peierls' scheme basing on Fermi surface nesting. Other theories such as a saddle point mechanism or electron−phonon coupling have also been proposed [124]. Many CDW materials are also superconducting. Superconductivity and CDW state are usually competing with each other at low temperature.

$TiSe_2$ undergoes a CDW phase transition into a commensurate $2 \times 2 \times 2$ superstructure at ~200K. As we mentioned before the nature of its semiconducting or semimetallic property still has dusputes, but the ARPES study showed that a gap of about 0.1 eV is formed in CDW phase [125]. At 77K, the displacement for Ti atoms are about 0.085Å, 3 times larger than Se atoms [27]. $TiSe_2$ is not a superconducting material. But when the CDW is suppressed, it will show superconductivity. Morosan et al. reported that CDW transition can be suppressed by Cu intercalation, and a new superconducting state emerges near x=0.04, therefore a superconducting state emerged with a maximum transition temperature of 4.15K [126]. Kusmartseva also showed that by applying pressure on pure 1T-$TiSe_2$, the CDW order melted and a superconducting phase emerged in the pressure ranges of 2–4 GPa [127]. Kolekar et al. showed that CDW transition temperature for monolayer $TiSe_2$ is significantly increased, and also strongly dependent on the substrate material [128].

CDW in 1T-VSe_2 has a 4×4 nesting vector and the transition temperature is ~110K. Sugawara et al. used STM and optical polarimetry measurements to demonstrate that the CDW peaks in 1T-VSe_2 form a kagome lattice, which is different from other TMDCs [129]. Duvjir et al. confirmed that imperfect nesting in three dimensions bulk VSe_2 universally flows into perfect nesting in Monolayer VSe_2, resulting a significant increasing CDW temperature from 105K to 350K. They also found another metal−insulator transition at 135 K with the help of ARPES and STM [130].

2H-$TaSe_2$ has a 3×3 CDW supercell. There are two CDW transitions in $TaSe_2$: a incommensurate transition at 122 K and a commensurate transition at 90 K. Ryu et al. confirmed that the 3×3 CDW order remains the same in monolayer $TaSe_2$. They also found that spin−orbit coupling and enhanced lattice distortion is more likely the origin of CDW order rather than Fermi nesting or saddle-point-based mechanism [131]. Freitas et al. present measured the superconducting and CDW critical temperatures as a function of pressure in both 2H-$TaSe_2$ and 2H-TaS_2. They found that the incommensurate transition temperature for 2H-$TaSe_2$ decreased to ~90K at 20 GPa. Similar trend can also be found in 2H-TaS_2 [132].

TaS_2 has 3 polytypes: 1T, 2H, and $4H_b$. 1T-TaS_2 has a $\sqrt{13} \times \sqrt{13}$ 'Star of David' shape CDW order and 3 CDW transition phases: metallic to incommensurate CDW at 543K; incommensurate CDW to nearly-commensurate CDW transition at 347K; and finally commensurate CDW transition at 183K. The rotation angle respect to the undisturbed lattice changes to 13.9° during

incommensurate to the commensurate phase transistion, for nearly commensurate phase the angle is 12° [133]. Zhu et al. demonstrated that Joule heating effect only played a secondary role in the NC to IC-CDW transition in 1T-TaS_2, while the IC-NC CDW transition is mainly determined by the temperature change of the sample. Moreover, light illumination can modulate the CDW phase, therefore change the frequency of the 1T-TaS_2 CDW oscillator [134]. 2H-TaS_2 has a 3×3 CDW order and undergoes an CDW phase transition at about 75K. For $4H_b$-TaS_2, the structure is built as alternating 1T and 1H layer stacking, therefore the CDW transition in $4H_b$-TaS_2 shows $\sqrt{13} \times \sqrt{13}$ and 3×3 within each layer. Fujisawa et al. used STM directly observed the Moiré pattern in $4H_b$ polytype TaS_2 caused by the differnet CDW superlattices between layers [135].

Bulk 2H-$NbSe_2$ undergoes a 3×3 CDW transition at 33K and a superconducting transistion at 7.2K. Ugeda et al. used STM confirmed that the 3×3 CDW superlattice remained unchanged in monolayer $NbSe_2$. However, the superconducting transition critical temperature was depressed to 1.9K [136]. Xi et al. reported that the CDW transistion temperature for monolayer $NbSe_2$ increased to 145K, which probably driven by the strong electron–phonon interactions in two-dimensional $NbSe_2$ [137].

Two-dimensional (2D) semiconducting transition metal dichalcogenides (TMDCs) such as MoS_2 and WS_2 have attracted considerable interests due to their potential application in next-generation electronics [138], optoelectronics [139], photovoltaic device [140], and so on. Beyond semiconducting TMDCs, 2D metallic TMDCs such as 1*T*-$TiSe_2$ [125,141-143], 2*H*-$NbSe_2$ [136,137,144], 1*T*-TaS_2 [145,146] and *1T*-$TaSe_2$ [147-149]have recently emerged as unique platforms for exploring their exciting properties of superconductivity and charge density wave (CDW) at low dimension. These ultrathin metallic TMDCs films behaved dramatically different properties from their bulk counterparts due to their unique 2D plenary structures and thus provided important insights into the origins of superconductivity and CDW in TMDCs which have been a longstanding question in condensed matter physics [126,127,150]. Among these metallic TMDCs, $TiSe_2$ is a typical CDW material which undergoes a CDW phase transition at ~200 K accompanied by the formation of a $2 \times 2 \times 2$ superstructure, and the CDW order can be suppressed and replaced by superconducting (SC) order via external modulations, such as doping and pressure [126,127]. Very recently, the phase transitions of ultrathin 2D $TiSe_2$ has been explored with both angle-

resolved photoemission spectroscopy (ARPES) [125,142] and electrical measurements [143], revealing distinct CDW phase transitions in these 2D atomic layers. More importantly, the 2D nature of ultrathin $TiSe_2$ flaks allows for the modulation of many body states by electric field and as a consequence, the details of the CDW/SC phase transitions of $TiSe_2$ can be tuned by electric-field effect [143], which is remarkable leap towards the practical applications of 2D TMDCs in CDW collective state and superconductivity devices. Besides further understanding the fundamental physics in these materials, another key challenge for the potential applications of these 2D TMDCs remains on the controllable synthesis as the chemical synthesis of pristine 2D CDW/SC TMDCs has not been achieved so far. Chemical vapor deposition (CVD) has been successfully employed to grow ultrathin semiconducting TMDCs such as MoS_2 and WS_2 [151,152], but it is not feasible to apply conventional CVD approach in synthesizing high quality metallic TMDCs due to the very high tendency of oxidation for these materials [143-145]. Molecular beam epitaxy (MBE) has been utilized to deposit $TiSe_2$ thin films on graphene [125,141,142], however, this approach is not capable of growing pristine $TiSe_2$ on insulating substrates without graphene which may significantly affect the phase transitions [125,142]. Therefore, it is highly desired to develop controllable chemical methods to synthesizing pristine ultrathin $TiSe_2$ flakes for making this emerging material easily accessible for exploring new fundamentals in both condensed matter physics and device physics.

Here, we explored the surface growth of ultrathin highly crystalline CDW/SC TMDCs with 1T-$TiSe_2$ as an example with chemical vapor transport (CVT) by carefully controlling the mass transport during the growth. For the first time, sub-10 nm pristine 2D $TiSe_2$ flakes were obtained by chemical synthesis and these flakes showed very high quality as indicated by atomic-resolved scanning tunneling microscopy (STM) imaging, spectroscopic characterizations and electrical measurements. Moreover, the characteristics feature of 2×2 superstructure for the CDW phase of $TiSe_2$ was clearly observed by STM on our samples at 77 K, indicating that well-ordered CDW states occurred at low temperature in the chemically synthesized ultrathin $TiSe_2$ flakes. The CDW phase transition temperature of the obtained $TiSe_2$ flakes was also determined to be in the range of 170-180 K by varied-temperature transport measurements, comparable with the mechanical exfoliated $TiSe_2$ flakes. Our work paved the way for the controllable synthesis of 2D CDW/SC TMDCs and thus greatly extended the functionalities and applications of 2D atomic crystals.

3.2 Method

CVT has been the most reliable approach for growing high quality TMDCs single crystals for both research and commercial purposes [153]. Although this approach has been intensively studied for decades for growing bulk crystals, it has never been tried on synthesizing 2D TMDCs. A typical chemical vapor transport growth of single crystals of TMDCs involves the volatilization and reactions of solid precursors (metals) with the aid of transport agents and the deposition of the products in the form of single crystals driven by a temperature gradient between the source and the growth zone in a sealed quartz ampoule [153]. In order to acquire the ultrathin flakes instead of bulk crystals using CVT method, the most critical question is how to dramatically slow down the growth rate to allow for the accurate control on the thickness of the obtained layered TMDCs. Based on intensive studies on the kinetics of single crystals growth by CVT, the growth rate of single crystals is controlled by the mass transport of reactants via gas motion from source zone to growth zone through diffusion or convection [153]. In our experiments, the ampoule lies horizontally and the pressure inside the ampoule is $< 2 \times 10^4$ Pa, so the mass transport is dominated by diffusion and therefore, the transport rate J can be described with Schafer's transport equation [154].

$$J \propto \frac{p_i}{\sum p_i} \cdot \frac{s}{l} \cdot \bar{T}^{0.75}$$

p_i : partial pressure of the transport effective specie, which is dependent on the amounts of transport agents and chalcogenide; s and l: cross-section and length of the diffusion path, respectively; and $\bar{T}$ is the average temperature of T_1 and T_2. Therefore, compared with conventional CVT growth, we should minimize the amounts of transport agent, increase the length of diffusion while decrease the cross-section of the diffusion path and reduce the average temperature to slow down the mass transport and enable the growth of 2D $TiSe_2$. Besides these, choosing suitable transport agent with lower transport capability is also an efficient way to slow down the growth rate of $TiSe_2$.

I_2 is the most-widely used transport agent for conventional CVT growth, but it is not feasible to grow ultrathin $TiSe_2$ with I_2 due to its too high transport ability. I_2 and AgCl as transport agents were tested to grow $TiSe_2$ flakes on different substrates, such as SiO_2/Si, C-plane sapphire and mica (Figure 3.1). Compared with AgCl, we found that the $TiSe_2$ flakes grown using I_2 as transport

agent are much thicker (hundreds of nm) than those of using AgCl, indicating the growth rate using I_2 as transport agent is much fast than that of using AgCl. And therefore, we utilized AgCl as transport agent for the growth of thin $TiSe_2$ flakes. The amount of transport agents is also critical to the growth of $TiSe_2$ thin flakes as shown in Figure 3.2. The optimized amount of AgCl is ~0.75 mg for a total mass of ~5.0 mg of the growth precursors.

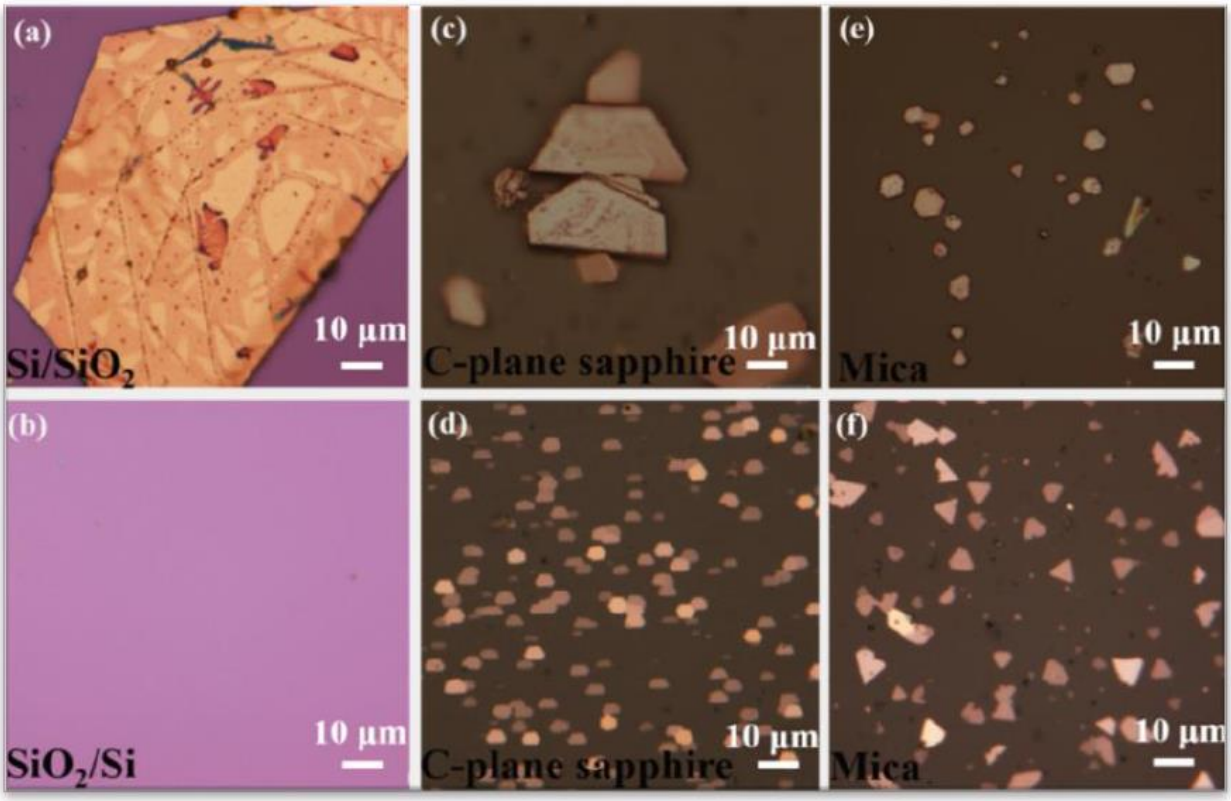

Figure 3.1. Optical images of $TiSe_2$ flakes grown using different transport agents (Figure a, c, and e using I_2; Figure b, d, and f using AgCl) with source temperature at 800℃ and growing temperature at 780℃ for 5 min on different substrates (Figure a and b: SiO_2/Si; Figure c and d: C-plane sapphire; Figure e and f: mica).

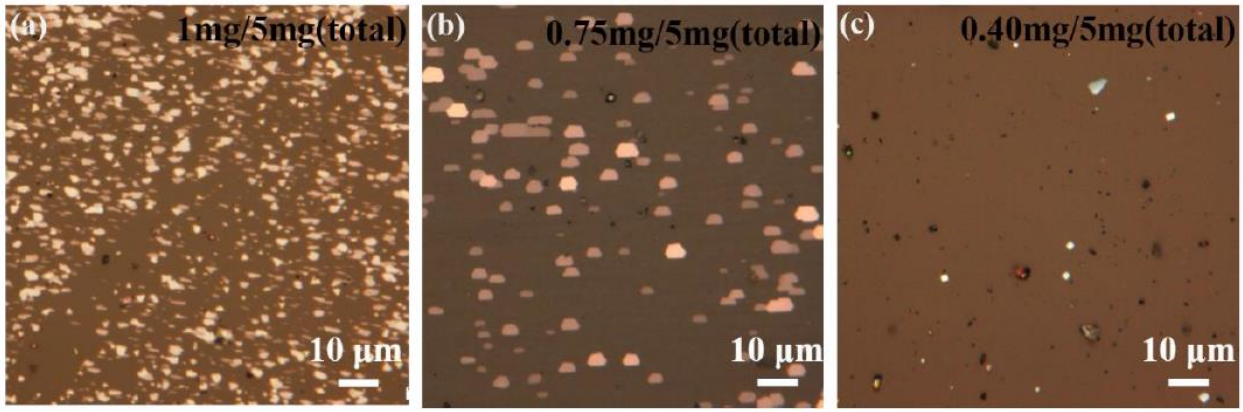

Figure 3.2. Optical images of $TiSe_2$ flakes grown with varied amounts of AgCl transport agent.

We observed that the growth results were very sensitive to the growth temperature as shown in Figure 3.3. Obviously, at a high growth temperature of ~800℃, the obtained $TiSe_2$ flakes showed irregular shape (Figure 3.3a) and at lower growing temperature of ~760℃, smaller flakes with a higher coverage were obtained (Figure 3.3c). On the C-plane sapphire substrate, the most suitable temperature for TiSe2 growth is 780℃ (Figure 3.3b). Besides growth temperature, the heating up and cooling down rates can also dramatically affect the growth results. Faster heating and cooling resulted in larger flakes as shown in Figure 3.4.

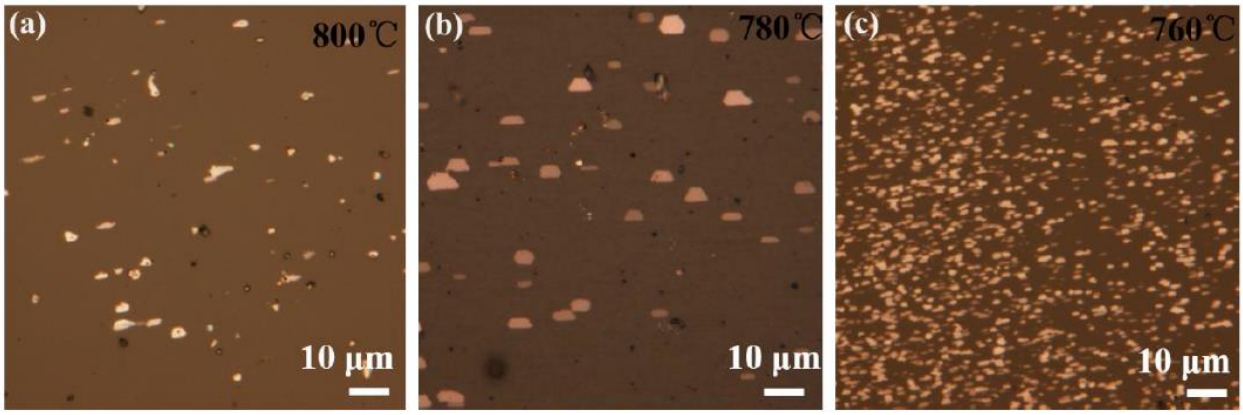

Figure 3.3. Optical images of $TiSe_2$ flakes obtained on sapphire substrates at varied growth temperature.

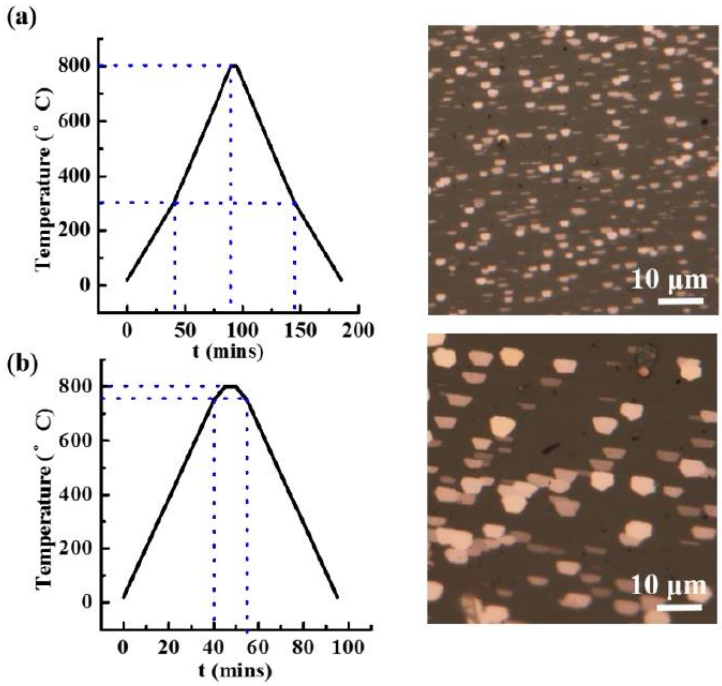

Figure 3.4. Temperature time profiles with slower (a) and faster (b) heating and cooling and corresponding growth results. Slower heating and cooling (<10℃ min) resulted in smaller flakes with an average size of 2 µm. Faster heating and cooling (~18℃ min) produced larger $TiSe_2$ flakes (~6 µm).

We observed that the growth substrates have significant impact on the growth results. As shown in Figure 3.1b, no TiSe2 flakes are obtained on SiO_2/Si substrates using AgCl as transport agent. Although sub 10 nm $TiSe_2$ flakes can be successfully grown on both sapphire and mica, the morphologies of the flakes obtained on these two substrates are totally different. The shape of $TiSe_2$ flakes grown on C-plane sapphire is half hexagonal and these flakes are parallel to the steps of the substrate independent of the gas flow direction (Figure 3.5), indicating that the growth of TiSe2 on sapphire is guided by the substrate. In addition, flakes grown on mica substrate are randomly distributed showing triangular shape with thickness of sub 10 nm (Figure 3.6).

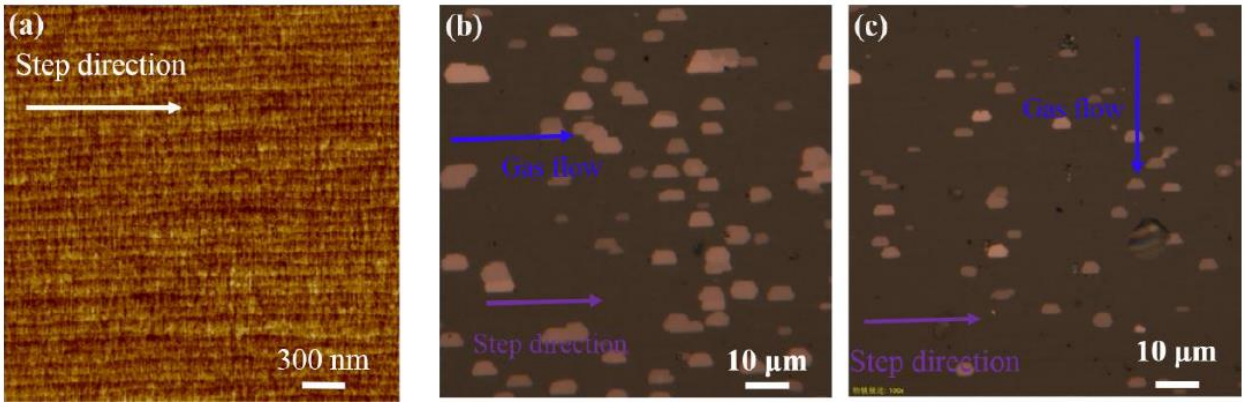

Figure 3.5. (a) AFM height image of the sapphire surface after annealing at 1000℃ for 2h, revealing the formation of aligned step edges (b) and (c) Optical images of the as grown $TiSe_2$ flakes when the gas flow direction is parallel or perpendicular to the step direction. From optical microscopic observations, the as grown $TiSe_2$ flakes are all aligned with the step direction independent of the gas flow directions, indicating that the alignment indeed originates from the substrate steps, not from the gas flow.

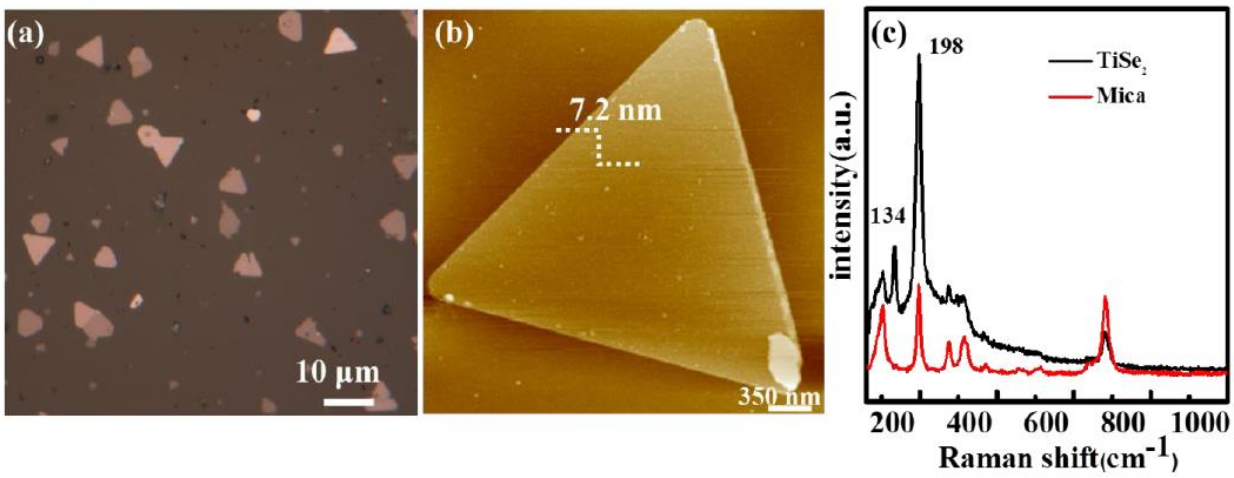

Figure 3.6. (a) and (b) Optical and AFM images of thin $TiSe_2$ flakes grown on mica substrate under the same growth conditions as using C-plane sapphire substrate. (c) Raman spectra of $TiSe_2$ flakes on mica substrate.

From the above discussions, we can conclude that the choice of transport agent is the most critical point for the controllable CVT growth of 2D $TiSe_2$. With a suitable transport agent, other growth parameters, such as growth temperature, substrates, the amounts of growth precursors and so on can be further tuned to achieve the optimized growth results.

3.3 Result and Discussion

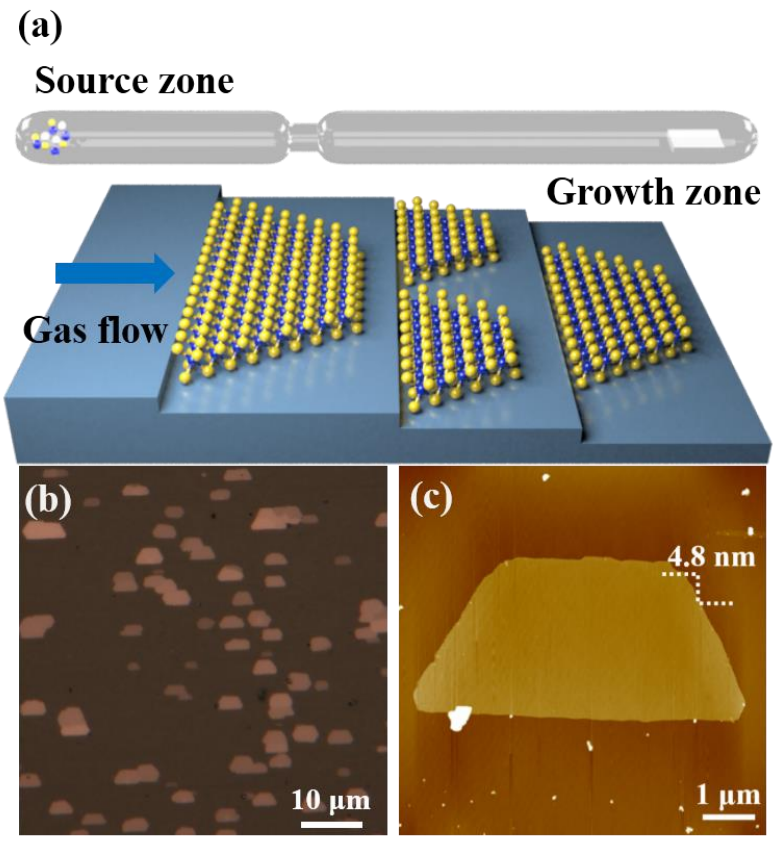

Figure 3.7. Synthesis of ultrathin $TiSe_2$ flakes using CVT method. (a) Schematic setup of the CVT method and atomic models showing the nucleation and growth of $TiSe_2$ are guided by the step edges on sapphire. (b) and (c) Optical and AFM images of the as-grown $TiSe_2$ flakes on the C-plane sapphire substrate which show half-hexagonal shapes with preferred orientations on the substrate.

Based on the above discussions, we designed the growth setup for the growth of $TiSe_2$ thin flakes as schematically illustrated in Figure 3.7a. To start with the synthesis, ultrapure Ti, Se and AgCl powders (~5 mg in total) were mixed at an appropriate ratio by fine grinding and then sealed together with a sapphire substrate in an evacuated quartz ampoule at a pressure of $<1.5\times10^{-4}$ Pa and the source powders were separated from the substrate by a neck on the ampoule. After the

sealing, the ampoule was loaded into a two zones furnace and the distance between the growth precursor and substrate was well-adjusted to ensure the temperatures for the source and growth regions were 800 ℃ and 780 ℃, respectively. By optimizing various growth parameters including substrate, growth temperature, the amount of AgCl and heating and cooling rates, very slow growth of $TiSe_2$ has been achieved, which allows for controllable synthesis of ultrathin $TiSe_2$ flakes by tuning the growth duration. After the growth for 5 min at the optimized condition, ultrathin $TiSe_2$ flakes in half-hexagonal shape with thickness of ~3-8 nm and length of ~4-10 μm were observed at a high density by both optical microscopy and atomic force microscopy (AFM) (Figure 3.7b-c). Obviously, these $TiSe_2$ flakes oriented along the same direction which is parallel to the step edges of the *C*-plane sapphire substrate, suggesting an epitaxial growth process. In contrast to the growth on sapphire, ultrathin $TiSe_2$ flakes grown on the mica substrate under the same growth conditions showed triangular shape. Therefore, we concluded that growth of ultrathin $TiSe_2$ flakes on sapphire substrates was guided by the step edges on the substrates in a similar way to the previous reported growth of WSe_2 on sapphire [155].

Micro-Raman spectroscopy is utilized to characterize the composition of the $TiSe_2$ flakes. The as-grown $TiSe_2$ flakes showed two Raman peaks at ~134 cm^{-1} and ~198cm^{-1} which were assigned to E^1_{2g} and A_{1g} mode, respectively under 632.8 nm excitation (Figure 3.8a), consistent with the Raman peaks of the bulk crystals [156]. Different from MoS_2 and many other 2D TMDCs [25], the Raman peak positions of $TiSe_2$ ultrathin flakes for both E^1_{2g} and A_{1g} modes did not show obvious dependence on the thickness down to 4.5nm (Figure 3.8a). To evaluate the uniformity of the $TiSe_2$ ultrathin flakes, we also performed Raman mapping image with ~198 cm^{-1} (strongest peak of $TiSe_2$) on the $TiSe_2$ flakes (Figure 3.8b), and the obtained mapping image showed uniform Raman intensity across the whole flake, confirming the high uniformity of our as-grown $TiSe_2$ flakes. Xray diffraction (XRD) was used to study the crystal structure of as-made $TiSe_2$ flakes. The peaks of our as-grown 2D $TiSe_2$ were consistent with the $TiSe_2$ crystal grown by the CVT method using I_2 as the transport agent, confirming the formation of single crystalline $TiSe_2$ thin flakes by our approach. To rule out the possible residue of Ag or Cl in our $TiSe_2$ flakes, we measured the individual $TiSe_2$ flakes with nano-Auger electron spectroscopy (AES), and the obtained results confirmed that no Ag or Cl element was detected by AES and the measured Se: Ti ratio was ~2.03, very close to the stoichiometric ratio of 2 for $TiSe_2$, further confirming the high purity of our $TiSe_2$ flakes.

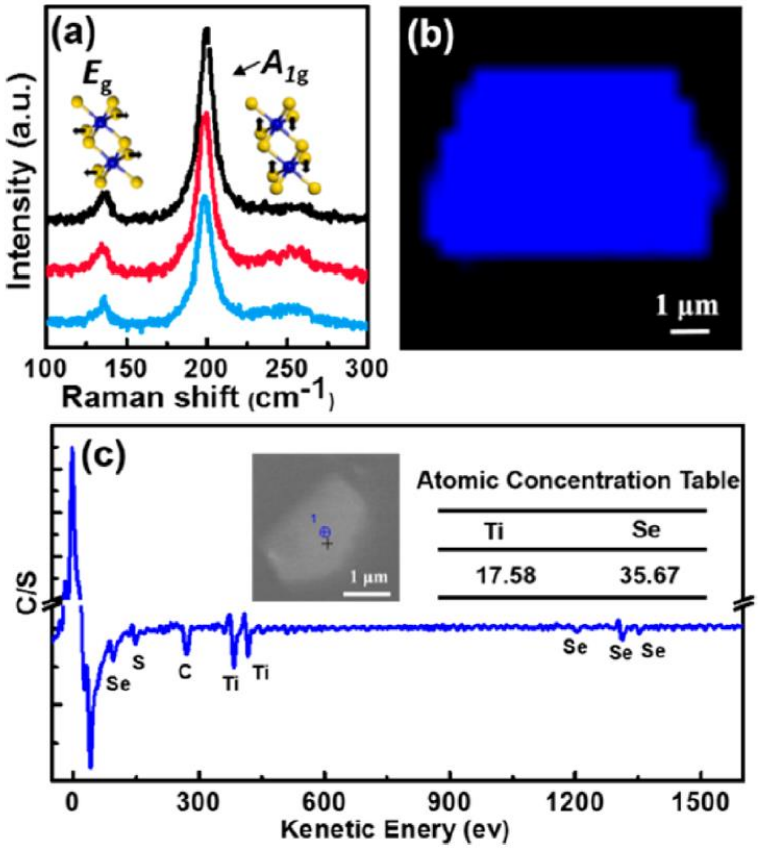

Figure 3.8. Raman and Auger electron spectroscopy characterizations of the CVT-grown ultrathin $TiSe_2$ flakes. (a) Typical Raman spectra of the $TiSe_2$ flakes with varied thickness of 4.5 nm, 6.5 and 12.0 nm, from bottom to top. Insets, the unit cell of the $TiSe_2$ lattice and the main phonon mode vectors. (b) Raman mapping image of a ~4.2-nm-thick flake with 198 cm^{-1} peak intensity. (c) Auger electron spectrum of an as grown 2D $TiSe_2$ flake as shown in the inset. To avoid charging effect during the measurements, a thin layer conductive polymer of Elektra 92 (SX AR-PC 5000/90.2) was spin-coated on the samples, and the detected S and C elements were originated from the polymer.

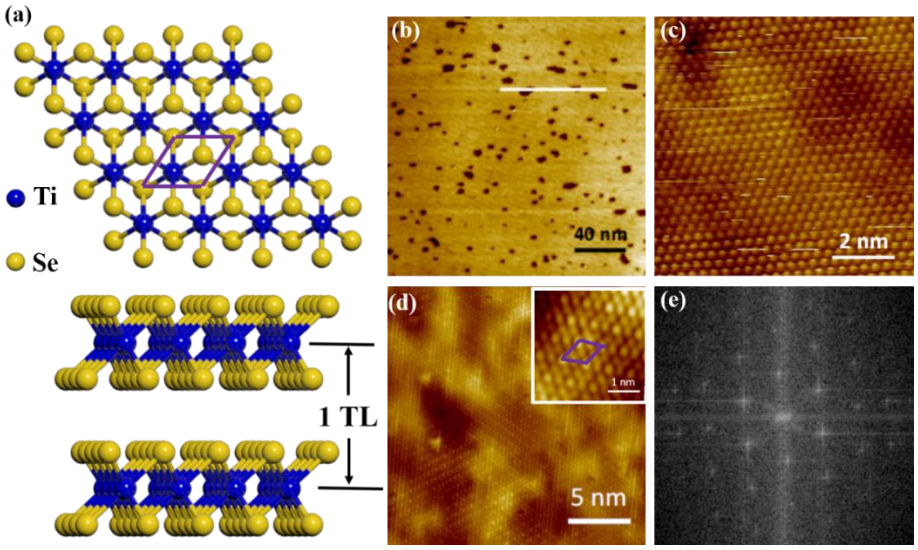

Figure 3.9. STM imaging of CVT-grown ultrathin $TiSe_2$ flakes. (a) Schematic crystal structure of 1T-$TiSe_2$. (b) Large-scale STM topographic image of the as-grown $TiSe_2$ flakes at room temperature (V_s = 1.0 V, I = 0.2 nA). The inset I s the line profile crossing a vacancy island marked by the green line. (c) Atomically resolved STM topographic image at room temperature (V_s = 0.4 V, I = 1.0 nA). (d and e) At T = 77 K, atomically resolved STM topographic images ((d) V_s = 0.2 V, I = 0.3 nA and (e) V_s = 0.1 V, I = 0.4 nA). Inset, the corresponding FFT image of (e).

We characterized the atomic crystal structure of as-grown $TiSe_2$ flakes (~5 nm thick) STM at both room temperature and low temperature. To obtain the intrinsic surface structure of the $TiSe_2$ flakes, we deposited metal contacts to the flakes grown on sapphire using shadow mask for direct STM imaging without transferring them to conducting substrates. Large scale STM image in Figure 3.9b of the as-grown $TiSe_2$ flakes obtained at room temperature showed a very smooth surface compared with the films grown by MBE [141,142], and in some regions small vacancy islands were resolved with a depth of~ 0.6 nm, in accordance with the c-axis unit-cell length of bulk $TiSe_2$ as shown in Figure 3.9a, which may be originated from the defects formed during the growth or by post-growth surface oxidation; the estimated defect density is $(7.7 \pm 3.9) \times 10^{-2}$ nm^{-2}. Atomic resolved STM images of the surface of $TiSe_2$ flakes showed well-ordered hexagonal packing of Se atoms with an interatomic spacing of 3.5 ± 0.1 Å, in consistence with the atomic structure of 1T-$TiSe_2$ as illustrated in Figure 3.9a. At T = 77 K, the atomically resolved STM images and corresponding 2D fast Fourier transform (FFT) image reveal a 2×2 superlattice, suggesting the occurrence of CDW order at low temperature (Figure 3.9d and 3.9e) [157,158].The existence of

the well-ordered CDW phase at 77 K in our synthesized ultrathin TiSe2 flakes strongly supports the high quality of our sample.

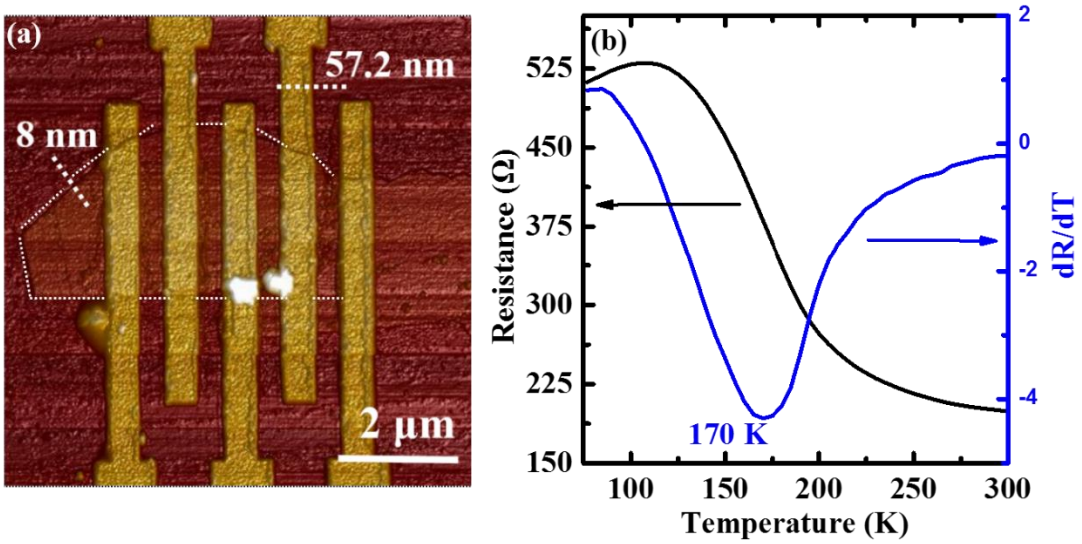

Figure 3.10. (a) AFM image of a typical multiple-terminal device of an as-grown $TiSe_2$ flakes with thickness ~8nm (b) Temperature dependence of the resistance of the as-grown $TiSe_2$ device shown in (a). Blue curve (dR/dT) denote the derivative of the resistance with the temperature, and the minimum value of the dR/dT at ~170K, indicating the CDW transition temperature [27].

To accurately determine the CWD phase transition temperature of the ultrathin $TiSe_2$ flakes, we fabricated multiple-terminal devices on these flakes with electron beam lithography (EBL) and metal deposition and carried out electrical measurements at varied temperature from 77-300 K. The four-terminal resistance-temperature (*R*-*T*) plot of a typical $TiSe_2$ flake with a thickness of ~8 nm showed a similar line shape to both bulk crystals and mechanically exfoliated flakes (Figure 3.10a and Figure 3.10b). The *R*-*T* curve presented a broad maximum at ~105 K with the ratio R_{max}/R_{300K} of 2.4. This ratio has been widely used to evaluate the quality of TiSe2 single crystals [126]; the ratio for our TiSe2 thin flakes is higher than the mechanically exfoliated ones (<1.5) [143], indicating our CVT-made $TiSe_2$ flakes having high quality. We noticed that our CVT-grown $TiSe_2$ ultrathin flakes showed a CDW phase transition at 170 K, which is the same as the T_{CDW} of exfoliated flakes [143], but dramatically lower than that of the bulk crystal at ~200 K, which may be attributed to the reduced thickness. Recently, two independent studies on the CDW transition

in 2D stacks of $TiSe_2$/graphene measured by ARPES reported dramatically different CDW transition temperatures of ~200 K and ~232 K [125,142], respectively. The inconsistencies of the measured transition temperatures of ultrathin $TiSe_2$ reported by different groups may be attributed to the varied defect densities, doping, interface with the substrate and also measuring methods and future studies on the origins of these differences may provide new insights for tuning the phase diagram of these 2D CDW/superconducting materials.

3.4. Conclusion

In summary, we developed a new approach for the controllable synthesis of high quality 2D TMDCs by tuning the kinetics in chemical vapor transport reactions. With this approach, pristine ultrathin $TiSe_2$ flakes were obtained with dimensions suitable for the sequential modulation of their CDW/superconducting phases. The as-made thin $TiSe_2$ flakes exhibited very high crystallinity as characterized by various microscopic, spectroscopic and electronic measurements, comparable to mechanically exfoliated thin $TiSe_2$ flakes. The occurrence of CDW phase accompanied with surface reconstruction was clearly visualized by the atomic resolved STM imaging at ~77 K and the CDW phase transition temperature of the CVT-grown $TiSe_2$ was also accurately measured with variable-temperature electrical measurements. This first observation of CDW phase in chemically synthesized pristine $TiSe_2$ ultrathin flakes presents a significant step towards the practical applications of the 2D CDW/superconducting materials. Moreover, in principle, all TMDCs that can be grown in the form of single crystals by CVT can also be grown into 2D form by carefully adjusting the growth parameters as we demonstrated in this work. Therefore, we believe that in parallel with CVD synthesis, CVT approach will become another universal method for growing various 2D atomic crystals to further extend the family of 2D materials.

Chapter 4. Electrical Stressing Induced Monolayer Vacancy Island Growth on [159] $TiSe_2$

This work is published on Nano Letters [159]. In this work I did all the experiment, draw the schematic structure, STM images and growth rate plot in figures 4.1, 4.3-4.5, wrote the whole "Introduction" and "Conclusion" sections and the experiment part of "Method" and "Result and Discussions" sections.

4.1. Intruduction

Emerging 2D materials, such as atomically thin transition metal dichalcogenides (TMDs), have been the subject of intense research due to their fascinating properties and potential practical applications [160-162]. TMDs have a layered structure in which a transition metal atom layer is sandwiched between two chalcogen atom layers and adjacent layers are stacked via Van der Waals forces. Atomically thin TMDs vary from metallic, semimetallic, to semiconducting, and can be used in electronic devices, phototransistors, solar cells and gas sensors [92,103,163-166]. As a member of the TMDs, 1*T*-$TiSe_2$ is a widely studied charge density wave (CDW) material. Below 200 K, 1*T*-$TiSe_2$ undergoes a phase transition to a CDW state, showing a $2 \times 2 \times 2$ commensurate superlattice [27,123,167]. Such a transition in 1*T*-$TiSe_2$ implies great potential applications in optoelectronics [168], voltage-controlled oscillators [146] and ultrafast electronics [169].

However, the properties of atomically thin TMDs and other 2D materials are both sensitive to and governed by defects and interfaces, such as domain boundaries and edges [170-173]. Usually these interfaces are more susceptible to thermal fluctuations and external stimuli, than the bulk of the material [174,175]. Thus, for practical applications of mono- and few-layer TMDs, it is essential to characterize their structural stability when subjected to the external stimuli present in devices, such as: electrical fields, irradiation and other forcing conditions. In situ investigations of said systems are usually difficult given the dynamical conditions present. To date, quantitative characterizations of the structural stability of these systems are still lacking. Furthermore, it is important to utilize theoretical modeling to interpret the results and understand the impact of

measurement parameters on observed trends. Numerical techniques such as molecular dynamics (MD) and phase-field modeling enable one to calculate the dynamical evolution of materials. Importantly, the phase-field method, unlike MD, can access diffusive time and length scales appropriate for studying microstructure stability in electronic materials.

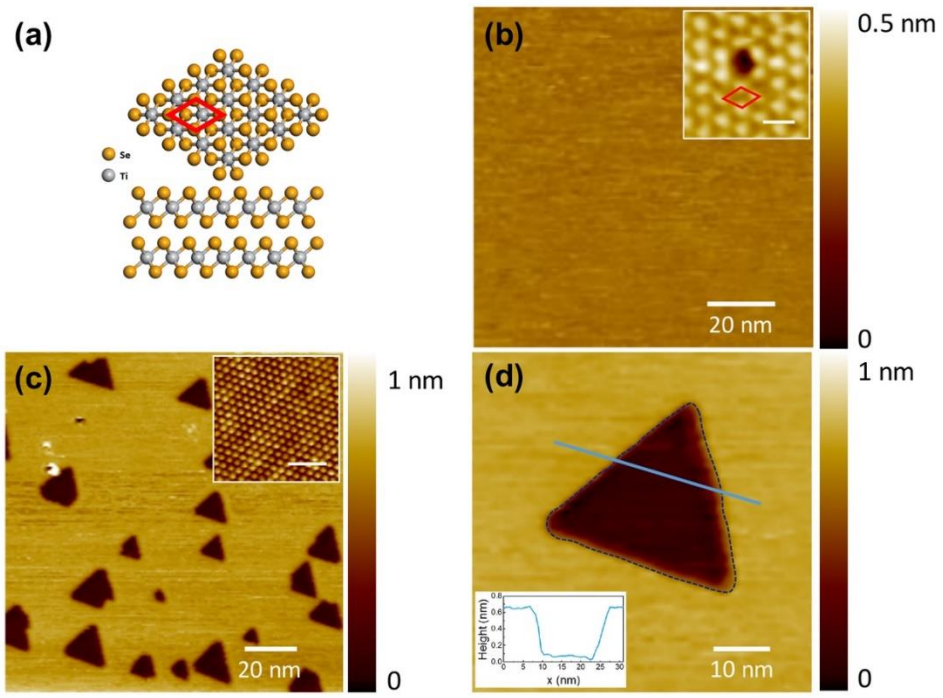

Figure 4.1. (a) Schematic structure of 1*T*- $TiSe_2$ in the top and side views. (b) STM image of freshly cleaved $TiSe_2$ surface (V_s = 0.99 V, I = 0.27 nA). Insert: Atomically resolved STM image showing a Se atomic vacancy (V_s = 0.1 V, I = 1.0 nA, scale bar = 0.5 nm). (c) STM image of monolayer vacancy islands on 1T-$TiSe_2$ after annealing (V_s = 0.70 V, I = 0.31 nA). Insert: Atomically resolved STM image of freshly cleaved $TiSe_2$ surface (V_s = 0.06 V, I = 1.29 nA, scale bar = 2 nm). (d) A zoom-in STM image of a single triangular vacancy monolayer island (V_s = 0.99 V, I = 0.4 nA). Insert: Line profile crossing a triangular vacancy monolayer island marked by the solid blue line.

Using monolayer vacancy islands on titanium diselenide ($TiSe_2$) surfaces as a model system, as shown in Figure 4.1a, we experimentally and theoretically investigated their shape evolution and growth rate driven by scanning tunneling microscopy (STM) electrical stressing. When electrically stressed by a STM tip, the equilibrium triangular monolayer vacancy islands evolve to a hexagonal

shape and the island area shows a non-linear area growth dependence with respect to time. The observed dynamics represent a departure from the linear area growth law expected for bulk vacancy clustering. The growth rate dependence on the tunneling current is also experimentally determined. Our simulations of shape and size evolution using a phase-field model are consistent with our experimental observations, and strongly suggest that the STM driven vacancy island growth is driven by island edge atom dissociation under electrical stressing. The non-linearity observed in this study indicate that 2D transition metal dichalcogenides may prove to be even more unstable under electrical stressing than expected for typical bulk materials, and could be potentially important for understanding the device reliability and limitations of atomically thin TMDs and other 2D materials subject to electrical stressing. These results are particularly relevant for TMD transistors subject to analogous vertical electric fields and leakage tunneling currents through gating.

4.2. Methods

4.2.1. Experimental methods

Single crystals of 1*T*-$TiSe_2$ were grown with chemical vapor transport (CVT) using iodine as the transport agent purchased from 2D age. Prior to performing scanning tunneling microscopy (STM) measurements, X-ray diffraction (XRD) and electrical measurements were conducted to confirm the high quality of the crystals.

The STM experiments were carried out in a customized STM (Omicron STM1). The fresh surfaces of samples were prepared by the mechanical exfoliation method. STM scanning was performed at room temperature in a vacuum chamber with a base pressure of lower than 10^{-9} Torr. The STM tips used in the experiments were etched from polycrystalline tungsten wires. All the STM images were obtained in the constant current mode.

4.2.2. Theoretical simulation method

Phase-field modeling is a phenomenological technique capable of simulating the kinetics of phase transformations and microstructural evolution. This technique relies on the construction of a free energy functional to describe the thermodynamics of the system of interest. We have chosen to utilize the phase-field method because it is able to access the exceptionally long diffusive simulation time scales present in our experiments (~800 min). Such time scales are well beyond the existing capabilities of MD and related atomistic methods. In our phase-field model of $TiSe_2$, a binary component model was used with two components (atoms and vacancies) [176,177]. The current simulations are based on that developed by Rokkam, El-Azab, Millet and Wolf [178] in which an order parameter (ϕ) and a concentration of vacancies (c_v) describe the system free energy (F) in the following form:

$$\mathrm{F}[\phi, c_v] = N \int \left[G(c_v)h(\phi) + w(c_v, \phi) + \frac{1}{2}\left|\varepsilon_\phi \nabla \phi\right|^2 + \frac{1}{2}|\varepsilon_v \nabla c_v|^2 \right] dV. \quad (1)$$

The function $G(c_v)$ represents the enthalpic and entropic contributions to the free energy. The free energy admits two stable bulk solutions by design. Moreover, $h(\phi)$ represents (1) terpolation function that allow for smooth transitions of the bulk free energy across interfaces. At $\phi = 0$, we have a stable well that represents the equilibrium concentration of vacancies determined by $G(c_v)$. Then at $\phi = 1$, the stable well is that for a void at $c_v = 1$ given by $w(c_v,\phi)$, which represents a driving force term as part of the bulk thermodynamics, as shown in Figure 4.2. The number of lattice sites is given by N. Finally, ε_v and ε_ϕ represent the gradient energy coefficients for the order parameter and concentration fields respectively, which determine the properties of interfaces. Within our phase-field model, we assume that the governing equations driving the microstructural evolution of $TiSe_2$ are:

$$\frac{\partial \phi}{\partial t} = -M_\phi \frac{\delta \mathrm{F}}{\delta \phi} \quad (2)$$

$$\frac{\partial c_v}{\partial t} = -\nabla \cdot \boldsymbol{J} + Zg(\phi) \quad (3)$$

$$\boldsymbol{J} = -M_v \nabla \frac{\delta \mathrm{F}}{\delta c_v} \quad (4)$$

$$M_v = \frac{D_v\, c_v^2 (1-c_v)^2}{k_B T} \tag{5}$$

$$g(\phi) = (\phi - 1)^2\, e^{-\alpha(\phi-1)^2} \tag{6}$$

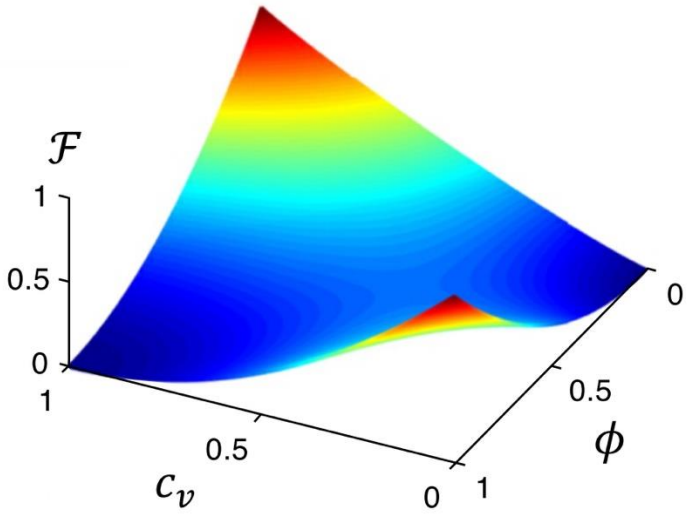

Figure 4.2. 3D representation of the bulk free energy of the system.

In the above equations, M_ϕ represents the interfacial mobility of the system and M_v is the diffusional mobility which is related to the diffusion coefficient (D_v) of vacancies. This mobility can be concentration and order parameter dependent; in this work we only allow it to have a compositional dependence (as given by Eq. (5)). The term $Zg(\phi)$ in Eq. (3) represents a source term driving the preferential formation of vacancies at void edges, via electrical stressing from a STM tip. The magnitude and breadth of the source term are determined by the parameters Z and α, respectively.

The kinetics of the model described by Eqs. (2) through (6) follow from dissipative thermodynamics of conserved and non-conserved fields. Meaning, the phase-field in Eq. (2) follows the dynamics of free energy minimization, so-called Allen-Cahn dynamics. While, the concentration field (setting the source term to zero) follows the continuity equation of flux conservation Eq. (3), so-called Cahn-Hilliard dynamics. These dynamics are also called *Model A* and *Model B* respectively, and when combined are referred to as *Model C*.

Lastly, to capture the hexagonal anisotropy observed during $TiSe_2$ void growth, the order parameter gradient coefficient was constrained to be orientation dependent in the form:

$$\int \left|\varepsilon_\phi \nabla\phi\right|^2 dV \rightarrow \int \left|\breve{\varepsilon}_\phi(\theta)\nabla\phi\right|^2 dV \tag{7}$$

Where, θ is the orientation of the interface normal referenced to the experimental image frame and $\breve{\varepsilon}_\phi$ describes the degree of anisotropy of the surface tension.

The bulk thermodynamic contributions to the free energy can be further expanded out into

$$G(c_v) = E_v(1-c_v) + k_B T(c_v ln(c_v) + (1-c_v)\ln(1-c_v)) \tag{8}$$

$$w(c_v,\phi) = p(\phi)\left(c_v - c_v^{eq}\right)^2 + g(\phi)(c_v-1)^2\,. \tag{9}$$

where $p(\phi)$ and $g(\phi)$ represent interpolation functions that allow for smooth transitions of bulk free energy information across interfaces. They drive the free energy terms to zero as ϕ goes to 0 or 1. The energy of vacancy formation is given by E_v. As discussed in the main body of the manuscript, the order parameter gradient term must be further modified to generate hexagonal anisotropy in the contributions to the free energy. The interfacial energy coefficient becomes angle dependent which reflects the anisotropy of the structure. For a hexagonal structure this would imply that a given seed grows along six different directions, as described by:

$$\left|\varepsilon_\phi \nabla\phi\right|^2 \rightarrow \left|\breve{\varepsilon}_\phi(\theta)\nabla\phi\right|^2 \tag{10}$$

$$\breve{\varepsilon}_\phi(\theta) = \varepsilon_\phi A(\theta) \tag{11}$$

$$A(\theta) = 1 + \gamma\cos(6\theta) \tag{12}$$

$$\theta = \arctan\left(\frac{\frac{\partial\phi}{\partial y}}{\frac{\partial\phi}{\partial x}}\right). \tag{13}$$

In the above equations, $A(\theta)$ modulates the anisotropy of the order parameter gradient coefficient and γ is an amplitude coefficient. A table summarizing the parameters utilized in our phase-field simulations is given below.

TABLE 4.1. $TiSe_2$ Phase-field Simulation Parameters

Parameter	Value
E_v	0.35 eV
A	0.35 eV
B	0.35 eV
ε_ϕ	2.0 $eV^{1/2}$ $nm^{-1/2}$
ε_v	1.0 $eV^{1/2}$ $nm^{-1/2}$
c_v^{eq}	1.3176×10^{-6}
ε	0.08
Δx	0.5 nm
Δt	0.001 min
D_v	5×10^{-18} cm^2 s^{-1}
M_v	0.03 nm^2 eV^{-1} min^{-1}
M_ϕ	0.15 eV^{-1} min^{-1}
c_v^o	$2.0 \times c_v^{eq}$
Z	0.14 min^{-1}
α	18.42

By scaling the model parameters [178], we were able to simulate $TiSe_2$ void growth through the application of these governing equations. A comprehensive discussion of the application of this phase-field model, to capture the vacancy island growth physics observed, is given in the next section.

4.3. Results and Discussions

The atomic structure of 1*T*-$TiSe_2$ is schematically shown in Figure 4.1a. Figure 4.1b displays a large scale STM image of a freshly cleaved $TiSe_2$ surface that appears atomically smooth. From the atomically resolved STM images (insets in Figures 4.1b and 4.1c), we were able to determine a lattice constant of 3.54 ± 0.06 Å. Some point defects, such as Se vacancy defects, as shown in the inset of Figure 4.1b, were also observed. Such intrinsic atomic defects have been previously observed in similar systems [123,179]. After annealing at 350℃ for 2 hours in the UHV chamber with a base pressure of lower 10^{-9} Torr, triangular vacancy islands with a size ranging from 10 to 30 nm were formed in a random distribution on the surface as shown in Figure 4.1c. The density of islands was determined to be $(5.0 \pm 2.6) \times 10^{10}$ cm^{-2}. The depth of islands, as shown in the line profile in Figure 4.1d, was measured at 6.2 ± 0.3 Å, consistent with the monolayer height of 1*T*-$TiSe_2$ [180]. By comparing with atomically resolved STM images obtained from small scan areas (see the inset of Figure 4.1c), the island edges can be seen to align overall along the highly symmetric orientations of the surface with some small deviation at short segments. The triangular shape observed is that commonly displayed for monolayer vacancy islands on TMD surfaces. Similar monolayer vacancy islands have previously been observed in other TMDs after annealing [181,182].

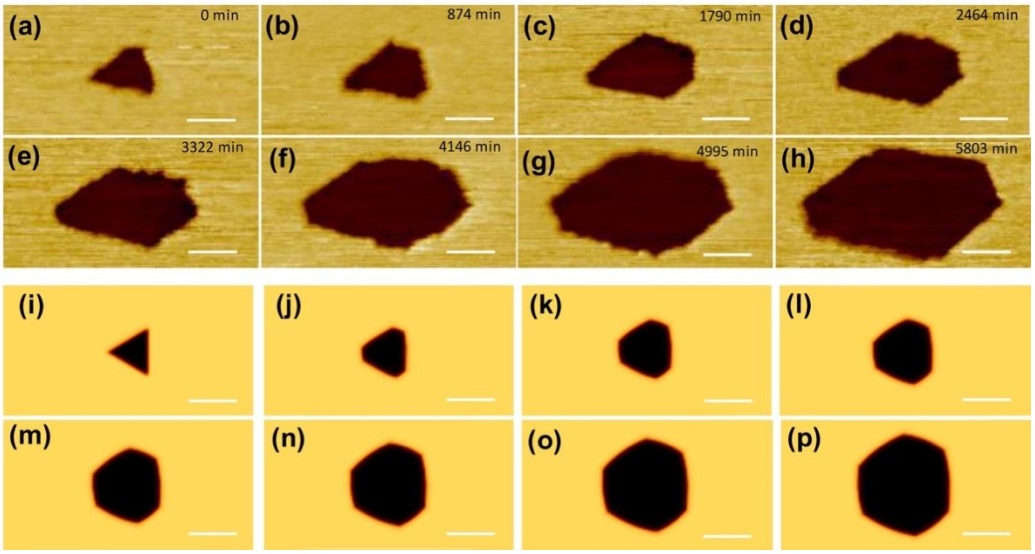

Figure 4.3. STM images (a-h) and phase-field simulations (i-p) of the time evolution of a monolayer vacancy island on the surface of $TiSe_2$ under continuous scanning (Scale bar: 10 nm, V_s = 1.0 V, I = 1.8 nA).

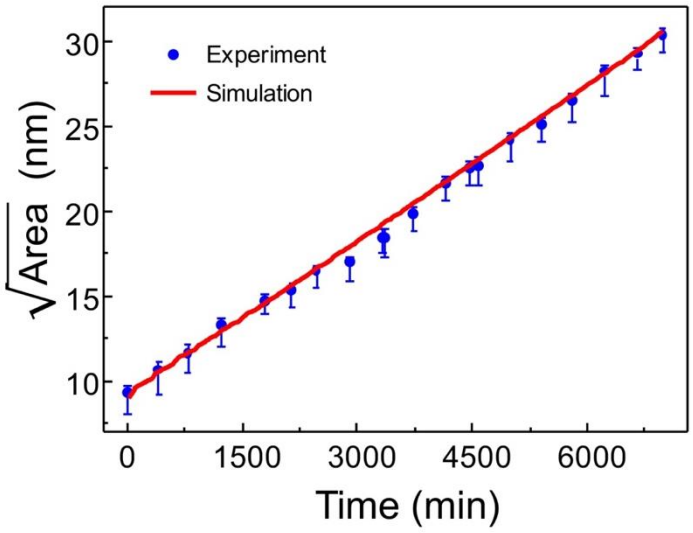

Figure 4.4. Square root of area of a monolayer vacancy island vs. time (V_s = 1.0 V, I = 1.8 nA). The solid line is result of a phase-field simulation with a preferential vacancy source term located at the vacancy island edges.

When an STM tip is continuously scanning, and thereby electrically stressing the surface, our results show that the monolayer vacancy islands grow and their shape changes. Figures 4.3a-h provide a snapshot of images spaced at a time interval of ~ 800 minutes, selected from a total data set of 974 sequential images, which clearly display the shape of the monolayer vacancy island evolving from triangular to hexagonal under STM electrical stressing. Such growth behavior only happens when an island is under continuous scanning with positive bias. To aid visual comparison, the images in Figures 4.3a-h were cropped from the scanning area of 88×88 nm^2. The scanning rate is 500 s per image with a 256×256 pixel resolution and a line-scanning speed of 90.9 nm/s. To extract the area of the monolayer vacancy islands, the perimeters were identified as the point at which the surface height is 30% of the step height lower than the top layer. This threshold was chosen to minimize the error included by island edge roughness, pixel noise, and STM image noise. The accuracy of the island area is given by the step width and is typically less than 3 nm for a sharp STM tip. To validate the analysis, we carefully checked the obtained island perimeters by visual inspection and ensured that the island area deviations introduced by the STM image processing computer code was at most 1%. The vacancy island area uncertainty was determined by varying the threshold values from 10% of the step height lower than the top layer to the midway between the top layer and the bottom of the monolayer vacancy islands. Figure 4.4 is a plot of the square root of the area of the monolayer vacancy island shown in Figures 4.3a-h as a function of time. The plot clearly indicates a non-linear parabolic dependence of the island area with respect to the STM scan time. By fitting the plot in Figure 4.4, we obtained a constant growth rate of $(3.00 \pm 0.05) \times 10^{-3}$ nm/s.

To validate our interpretation, we performed comparison experiments between islands subject to continuous scanning and others that were not continuously scanned. Figure 4.5a shows the initial morphology of a chosen area before continuous scanning. Subsequently we zoomed-in to Island #7 and performed continuous scanning on a smaller focus area of 58.52×58.52 nm^2 (V_s = 1.0 V, I = 1.8 nA). After continuously scanning Island #7 for ~ 740 mins, we zoomed-out to the same area as in Figure 4.5a. The final morphology of the area is shown in Figure 4.5b. Without continuous scanning, the vacancy islands remained unchanged in vacuum under room temperature. The areas of each vacancy island before (Figure 4.5a) and after (Figure 4.5b) are listed in Table 4.2. The area of Island #7 increased from 86 ± 6 nm^2 to 213 ± 5 nm^2 while the unscanned islands

did not show significant change. This data confirms that the island growth at room temperature is indeed induced by electrical stressing (by our scanning tunneling microscope).

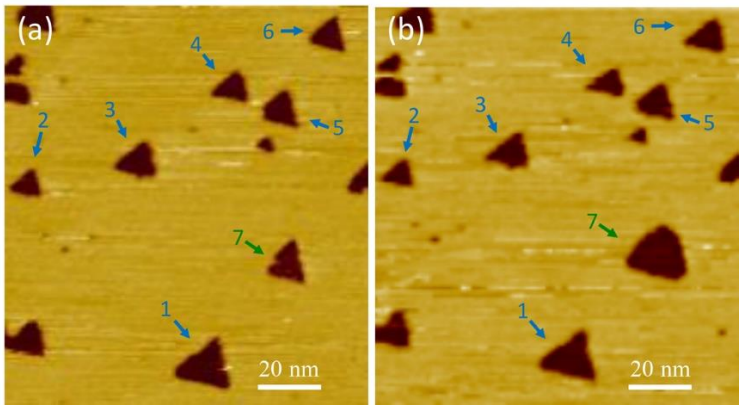

Figure 4.5. Large scale image of vacancy islands before (a) and after (b) continuously scanning on Island #7. The scanning parameters are V_s = 1.0 V, I = 0.52 nA for (a), and V_s = 1.0 V, I = 1.8 nA for (b), respectively.

TABLE 4.2. Area of the Islands

No. of the islands	Area before (Figure 4.5a) (nm^2)	Area after (Figure 4.5b) (nm^2)
1	150 ± 8	152 ± 13
2	49 ± 4	49 ± 3
3	86 ± 6	85 ± 7
4	62 ± 3	60 ± 6
5	76 ± 8	79 ± 5
6	67 ± 5	72 ± 3
7	86 ± 6	213 ± 5

We have performed controlled scanning over defined regions. Figure 4.6a shows an initial vacancy island. Instead of continuously scanning the entire island, we zoomed in to part of its edge and performed continuous scanning. Figure 4.6b shows the final morphology of the vacancy island after continuous scanning of total ~ 650 mins (the scan area varied from 30 nm^2 to 175 nm^2). We can clearly see that only the segment of the edge area under continuous scanning grew, causing a bump on the straight edge. Figure 4.6c is a high-resolution STM image of the edge section marked in Figure 4.6b. This result implies that potentially we may control the shape of vacancy island by scanning on particular position.

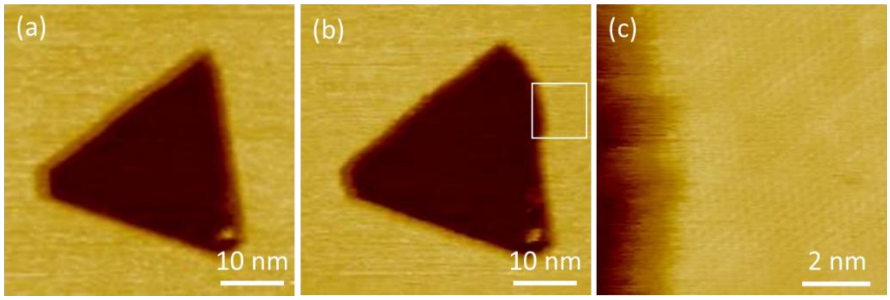

Figure 4.6. (a) Initial morphology of a vacancy island (V_s = 0.88 V, I = 0.23 nA). (b) Final morphology of the same island after continuous scanning on part of the edge (V_s = 0.64 V, I = 0.27 nA). (c) High-resolution STM image at the edge section marked in (b) (V_s = 0.07 V, I = 1.01 nA).

We also performed control experiments at negative sample bias. Figure 4.7 shows the island evolution under continuous scanning at a sample bias of –1 V and a tunneling current of 0.3 nA. The scanning size and scanning speed were kept the same with the data sets in Fig. 5. As shown in Figures 4.7a and 4.7b, there is no noticeable change on the size and shape of the island at t = 0 min and t = 902 min, which is totally different from the island growth behavior at a positive bias. By fitting the size vs. time plot (black data set in Figure 4.7c), the extracted growth rate is $2.3 \pm 0.5 \times 10^{-4}$ nm/min, which is one order smaller than the growth rate at +1 V under the same current (red data set in Figure 4.7c). At a higher tunneling current of 0.9 nA and other scanning parameters kept the same, the growth rate is $2.4 \pm 0.8 \times 10^{-4}$ nm/min, implying independence of vacancy island growth on the tunneling current at negative sample biases. These results indicate that the island growth is almost negligible at a negative sample bias. The asymmetric growth dependence upon electric polarity agrees with earlier studies of tip induced dissociation and can be explained by hot electrons injected from the STM tip to the samples.[183,184] At positive sample biases, hot electrons flow from the STM tip to the surface and induce the growth (or molecular dissociation). While at negative sample biases, hot electrons flow oppositely, from the sample to the tip, and thus do not induce monolayer vacancy island growth on the surface.

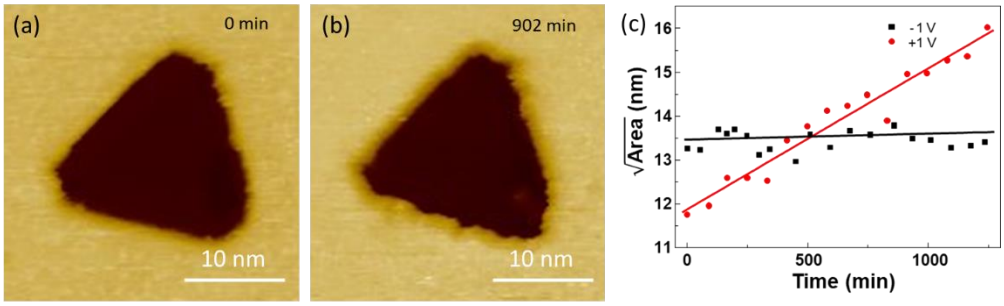

Figure 4.7. Time evolution of a monolayer vacancy island on the surface of $TiSe_2$ (a) before and (b) after continuous scanning at negative sample bias (Scale bar: 10 nm, V_s = –1.0 V, I = 0.3 nA). (c) Square root of area vs. time plots for –1 V and +1 V bias.

To understand the time dependence of $TiSe_2$ vacancy island growth, we employed a phase-field model to simulate island growth and shape evolution (as detailed in Section II). Initially, we attempted to model the vacancy island growth by assuming a uniform bulk distribution of vacancies induced by STM electrical stressing of the substrate. This yielded out-of-equilibrium vacancy-void clustering results that demonstrated linear area growth with respect to time, in line with the diffusional growth law for bulk vacancy clustering [185]. The experiments, however, demonstrated a non-linear behavior (as shown in Figure 4.4). We therefore concluded that electrical stressing applied by the STM tip must be preferentially driving vacancy formation at the vacancy island edges, due to the fewer number of bonding neighbors present for edge atoms, as discussed below.

The effect of electrical stressing from the STM tip was simulated in the model as a source term that is included in the vacancy concentration field equation of motion given by Eq. (3). This source term was added to generate a high concentration of vacancies at interfaces and a very small amount of vacancies in the bulk of the studied dichalcogenide [186-188]. Due to the diffusivity of the vacancies being so low and the contribution of a surface diffusion term $c_v^2(1- c_v)^2$ in the mobility, vacancies in the bulk are for practical purposes immobile while vacancies at the interface or in contact with the interface have a higher mobility thus allowing the void to take vacancies and grow. This low bulk diffusion has been validated experimentally by very low measured diffusion constants in dichalcogenides [186], from which we infer a low diffusion coefficient for vacancies in the $TiSe_2$ bulk.

The vacancy source term physically approximates the degree to which electrical stressing by the STM tip preferentially generates vacancies at the edges of $TiSe_2$ vacancy islands. The scope of the phase-field model is to capture the behavior of vacancies in $TiSe_2$ (as detailed in Section II). This behavior is limited to bulk diffusion, coarsening and surface diffusion of vacancies. Excess vacancies in the system can arise from either an initial excess of vacancies or through the source term $Zg(\phi)$ in Eq. (5). The Z term controls the amount of vacancies being added to the material via electrical stressing from the STM tip, while $g(\phi)$ controls the breadth of preferential vacancy generation at $TiSe_2$ vacancy island edges. In this manner the source term generates a higher amount of vacancies at interfaces and a lower amount of vacancies in the bulk of the material, thereby yielding a non-linear growth when the area is plotted against the simulation time as seen through the good agreement between theory and experiment in Figures 4.3 and 4.4. The vacancy island edge source term is physically justified by the fewer number of bonding neighbors present for interface adatoms and therefore a lower kinetic barrier for interface adatom dissociation (as compared to the bulk) upon electrical stressing by the STM tip [189]. And it is only through preferential edge vacancy generation that we are able to explain the non-linear vacancy island area growth with respect to time, though many other vacancy source mechanisms were explored (including uniform bulk vacancy generation, as discussed earlier). Although similar vacancy growth has already been seen on some TMDs through both STM and AFM measurements [64,120-122,190-195]. To our knowledge, this is the first time that a direct correlation between preferential electrical stressing at vacancy island edges and the observed growth rate has been established.

As long as there is some kind of preferential adatom dissociation at the interface, our $TiSe_2$ phase-field model produces parabolic growth behavior. Several $g(\phi)$ functions were used, that produced very similar results, however a more detailed analysis of how changing the source function affects the non-linear growth behavior is left for future work. Importantly, the very small diffusion coefficient assumed for $TiSe_2$ only allows the closest vacancies to the interface to "travel" towards the void and contribute to the growth leading to interfacial diffusion as the key growth mechanism. Physically speaking, this represents an etching process in which atoms are removed from the edge of the void due to electrical stressing from the STM tip. However, the model not only includes vacancy generation at the edge of a void (which is meant to represent the etching) it also draws any vacancies that are very close to the void (into the void). This is can be understood thermodynamically, whereby excess vacancies cluster to minimize the free energy (which is also

a way of reducing strain on the lattice). Thus, all vacancies that are near a void experience a thermodynamic potential drawing them towards it.

The observed hexagonal shape transition under non-equilibrium stressing can be attributed to a change in the void edge interface free energy under electrical stressing, due to preferential chalcogen (Se) removal at the edges. Recent first-principles work has shown that chalcogen removal from TMDs has a lower activation energy than transition metal atoms at TMD edges [189], and that the formation of chalcogen vacancies at/near edges drives the island free energy shape preference from triangular to hexagonal in TMDs [196,197]. Similarly, it has been shown that chalcogen rich conditions favor the formation of triangular islands, while chalcogen poor conditions result in hexagonal islands [172]. Although all these studies were applied to MoS_2, we hypothesize that the same chemical physics is present in $TiSe_2$ [172,189,196,197]. Meaning, the STM tip preferentially drives chalcogen (Se) removal and this changes the free energy of the void to favor hexagonal structuring during the growth process. The experimental images in Figures 4.3a-h support this interpretation, with the free energy shape preference gradually evolving from triangular to hexagonal as further chalcogen (Se) vacancies are created at/near the edges (such as the Se vacancy shown in the inset to Figure 4.1b).

Two methods of vacancy formation in a $TiSe_2$ monolayer were explored: (1) removal of an adatom vacancy to the vacuum; and (2) removal of an adatom vacancy to the bulk phase. In the case of removal to the bulk phase, this implies placing the removed atom in either bulk crystalline Ti or bulk crystalline Se (for Ti and Se vacancies, respectively). We define the vacancy formation energy, as the energy required to create a vacancy and place the removed atom in the new phase. From Table 4.3 below, it can be concluded that Se vacancy formation is strongly preferred, supporting our experimental conclusions. These calculations were performed utilizing a 6×6 $TiSe_2$ monolayer supercell. We leave a precise examination of vacancy formation kinetics to future work, as this would require exhaustive kinetic barrier calculations beyond the scope of this work.

TABLE 4.3. Estimated Energies Required to Form a Vacancy in $TiSe_2$

Vacancy Type	Vacuum	Bulk
Se	+4.25 eV	+1.53 eV
Ti	+10.68 eV	+5.24 eV

Now let us consider the energetics of $TiSe_2$ edges. We have examined six possible edges for a single monolayer of $TiSe_2$ as shown in Figure 4.8: armchair (AC), zig-zag terminated with Ti (ZZ-Ti), zig-zag terminated with one Se atom (ZZ-1Se), and zig-zag terminated with two Se atoms (ZZ-2Se). We have also considered dimerized ZZ-2Se edge reconstructions, but have found the configuration in Figure 4.8d to be lower in energy. These edges are arrived at by cutting $TiSe_2$ at symmetry angles separated by 30° (see Figure 4.8e). To study the energetics of these edges we utilized the nanoribbon geometries illustrated in Figure 4.8. [196] Among the configurations in Figure 4.8, nanoribbons with ZZ-Ti or ZZ-2Se edges are nonstoichiometric. The formation per unit length energy of these edges can be determined via:

$$\gamma_{edge} = [E_{Ti_nSe_m} - n\,\mu_{TiSe_2} - (m-2n)\mu_{Se}\,]/2L_{edge}\ ,$$

where $E_{Ti_nSe_m}$ is the total energy of a nanoribbon, n and m are the number of Ti and Se atoms in the nanoribbon respectively, μ_{TiSe_2} is the energy of a single $TiSe_2$ unit cell in a monolayer of $TiSe_2$, and μ_{Se} is the chemical potential of a Se atom. When $m = 2n$, the nanoribbon is stoichiometric and the formation energy does not vary with respect to μ_{Se}. When $m \neq 2n$, the nanoribbon is non-stoichiometric, as a result the formation energy is a function of μ_{Se}. In Figure 4.9 we have plotted the formation energies as a function of chemical potential difference ($\Delta\mu_{Se} = \mu_{Se} - \mu_{Se,bulk}$) in the range of $-0.45\ eV \leq \Delta\mu_{Se} \leq 0\ eV$, with $\mu_{Se,bulk}$ being the chemical potential of Se in the bulk phase. Here it can clearly be seen that a ZZ-2Se edge is energetically preferred at high concentrations of Se. We believe that the experimental system is initially Se-rich (prior to extended perturbation by the STM tip), such that $\Delta\mu_{Se} \to 0\ eV$ and all vacancy island edges are in the ZZ-2Se configuration. Now, due to the crystal structure of 1T-$TiSe_2$, the ZZ-2Se

construction may be achieved along any ZZ direction (as shown in Figure 4.8e). Thus, if one considers only the edge free energy in the Se-rich region, ZZ-2Se bounded hexagonal shapes should be preferred since they minimize the edge length for a given number of vacancies.

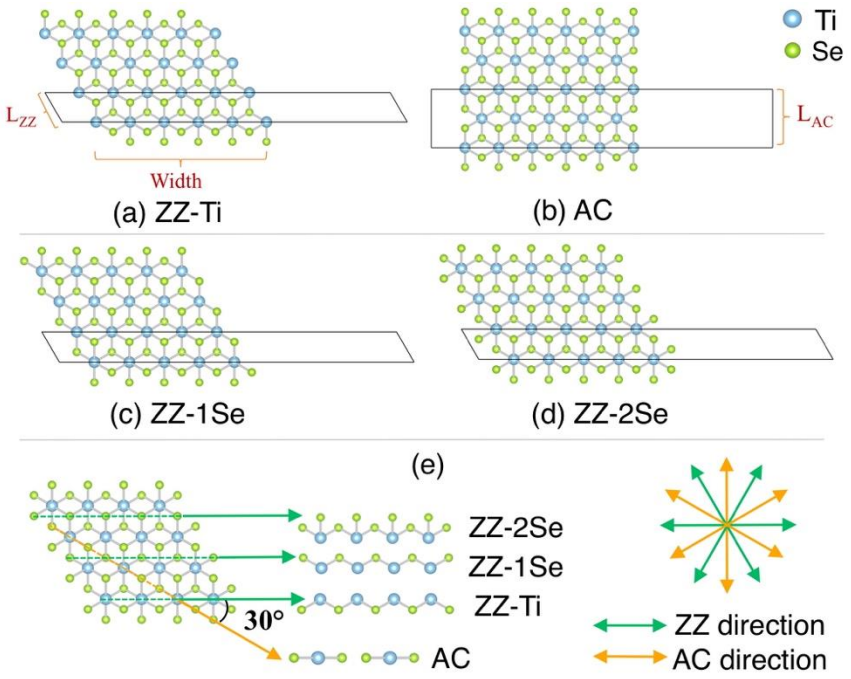

Figure 4.8. Different types of nanoribbon edges in a $TiSe_2$ monolayer. (a) A zig-zag edge terminated with Ti (ZZ-Ti), (b) an armchair (AC) edge, (c) a zig-zag edge terminated with one Se atom (ZZ-1Se), and (d) a zig-zag edge terminated with two Se atoms (ZZ-2Se). In each subfigure, the periodically repeating nanoribbon region simulated is shown. (e) Alternating armchair and zig-zag edges occur every 30°.

However, it is the total energy of the system which determines the preferred ground state and shape evolution (rather than solely edge energetics). In a total energy comparison one must consider both the cost of forming an edge and the exchange of any excess Se with the Se chemical potential reservoir (as well as the bulk energetics of $TiSe_2$). Any Se atom which is not able to find an edge ZZ-2Se edge binding configuration, can be considered to be rejected to the Se chemical potential reservoir. In a Se-rich environment, we have determined that a Se atom lowers its total energy by $-0.3117\ \text{eV} - \Delta\mu_{Se}$ when it is removed from Se chemical potential reservoir to a ZZ-2Se binding site (shown in Figure 4.8d). This implies that in Se-rich growth conditions (see Figure 4.9) it is

energetically favorable for a grouping of vacancies to organize into an edge reconstruction that provides more ZZ-2Se binding sites. A triangular shaped grouping of vacancies has a total edge length that is a 1.22× longer than the same vacancy area reoriented into a hexagonal shape. Thus, in Se- rich conditions a triangular shape is more energetically favorable than a hexagonal shape (if one evaluates the total energy of the entire system). When considering the Se chemical potential range over which triangular shape formation is favorable, one can compare the cost of forming a ZZ-2Se binding site versus placing the same Se atom in the Se chemical potential reservoir. As mentioned earlier, a Se atom lowers the total energy of the system by -0.3117 eV $- \Delta\mu_{Se}$when moving from the Se chemical potential reservoir to a ZZ-2Se binding configuration. However, the cost of forming a ZZ-2Se edge is also a direct function of $\Delta\mu_{Se}$, only when $\Delta\mu_{Se} \geq -0.038$ eV does the formation of a further ZZ-2Se site (to accommodate excess Se from the reservoir) become energetically favorable as shown in Figure 4.9. To arrive at this transition point we simply multiply the ZZ-2Se formation energy per unit length by the length of a ZZ-2Se unit cell (L_{ZZ} = 3.54 Å as shown in Figure 4.8), and solve for the value of $\Delta\mu_{Se}$ at which the ZZ-2Se site formation energy equals $+0.3117$ eV $+ \Delta\mu_{Se}$. In the region $\Delta\mu_{Se} \geq -0.038$ eV, it is energetically favorable for the same area of vacancies to reorganize into a triangular void with a lengthened edge (as marked in Figure 4.9) to provide more ZZ-2Se binding sites. Moreover, when $\Delta\mu_{Se} = 0$ eV in the extremely Se-rich regime, the net energy gain per additional ZZ-2Se binding site is -0.076 eV (which is not insignificant when multiplied over 100s or 1000s of edge binding sites). However, as one moves towards less Se-rich conditions the formation of triangular voids is less energetically favorable and a gradual transition towards hexagonal voids occurs (see Figure 4.9). Once there is no longer a sufficient concentration of Se (at sufficiently low values $\Delta\mu_{Se}$) to favor the ZZ-2Se edge, the stoichiometric ZZ-1Se edge becomes energetically preferred (see Figure 4.9); thereafter, the hexagonal shape is strongly preferred energetically (since, again, a ZZ-1Se edge can be formed every $60°$ along each ZZ edge). As discussed above, we hypothesize that the sample is initially extremely Se-rich and favors a triangular void shape. Scanning by the STM tip drives the removal of Se, creating more Se vacancies, and driving the system further towards a Se-poor configuration. We further hypothesize, this alters the local Se chemical potential in $TiSe_2$ and drives the shape evolution from triangular to hexagonal as observed in the experiments.

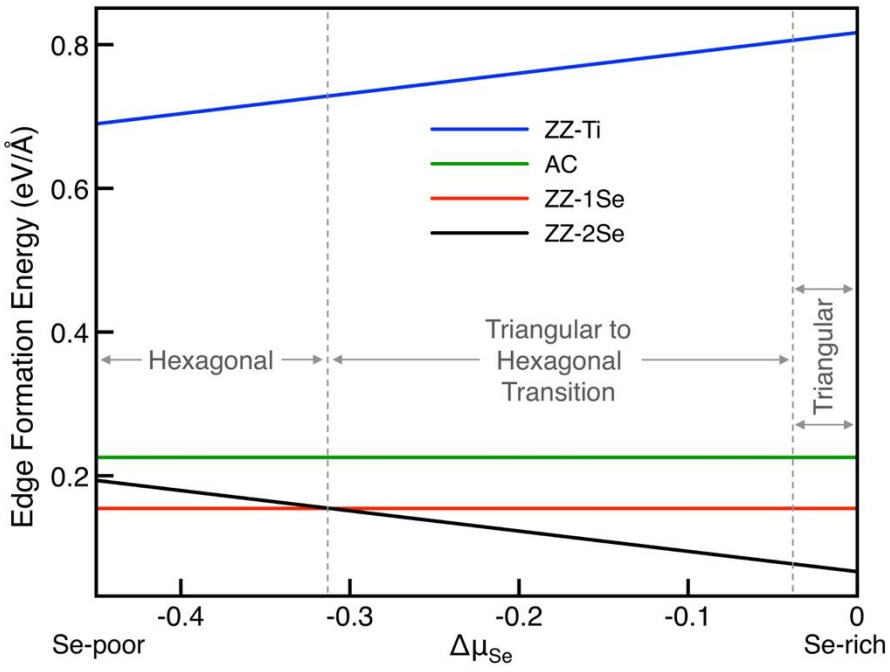

Figure 4.9. Formation energies of different edges as a function of the chemical potential change for Se atoms, with respect to the chemical potential of bulk crystalline Se. Triangular shaped voids are preferred when $\Delta\mu_{Se}$ is greater than -0.076 eV, when the sample is Se-rich. A gradual transition to hexagonal voids occurs as the Se content is lowered towards Se-poor.

Furthermore, we were able to further apply our model to capture the isolated growth of single voids and correlate the model directly with the observed STM image results in Figures 4.3a-h. As an initial condition, we start with a void (i.e., a cluster of vacancies) in the shape of a triangle like those of the experiment after annealing as shown in Figure 4.3i. We also assume that the interaction between voids is negligible and set the bulk vacancy concentration close to the equilibrium value for the given conditions. By allowing the phase-field model to progress at diffusional time scales we obtained the results in Figures 4.3i-p, which is in good agreement with the experimental results in Figure 4.3a-h both in terms of area and the structural transition from triangular to hexagonal.

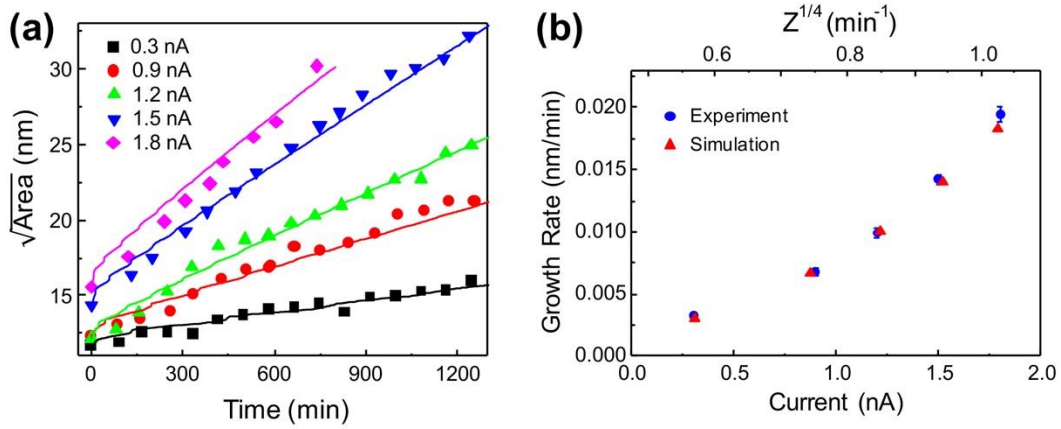

Figure 4.10. (a) Time evolution of square root of area of monolayer vacancy islands at various tunneling currents (V_s = 1.0 V), symbols represent experimental results and solid lines represent theoretical simulations. (b) Growth rate as a function of the tunneling current (blue circles) and plot comparing the growth rate against the ¼ power of the phase-field source constant *Z* (red triangles).

To understand the role of the tunneling current in the growth process, and further establish that the vacancy island growth is driven by electrical stressing by the STM tip, we measured monolayer island growth at various tunneling currents under the same tip status. Figure 4.10a shows a variation in island growth rates as the tunneling current is varied from 0.3 nA to 1.8 nA. In the measurements, the scanning areas, rates and sample bias were kept the same for the entire data set. The scanning area was held at 58.52 × 58.52 nm^2 and the scanning rate at 60.63 nm/s, with the sample bias set at 1.0 V. We were able to obtain an excellent fit to the parabolic area growth at different tunneling currents by altering only the source constant *Z* magnitude in the phase-field model as shown in Figure 4.10a. Only the initial island size was taken from experimental data in the phase-field results presented in Figure 4.10a. From this fit we were also able to obtain the growth rate as a function of the tunneling current, as shown in Figure 4.10b. There is an approximate quadratic non-linear relationship between growth rate and the tunneling current.

At this point we cannot conclusively state whether the quadratic non-linear relationship between the growth rate and the tunneling current is driven by the electric field or electric current increase (or both). However, when varying the scanning current we held the bias at 1 V, this implies that

the current gain arises from modulation of the tunneling barrier width (W). If one assumes a simple tunneling barrier where the current may be approximately described by the proportionality relation $I_{tip} \propto \exp(-2\kappa W)$, where $\kappa = \sqrt{2mU}/\hbar - m$ is the mass of an electron, U is its tunneling barrier, and $\hbar$ is Planck's constant. Then the variation in current from 0.3 nA to 1.8 nA can be attributed to an approximate 1 Å variation in the tunneling barrier width, assuming $U \approx 4$ eV. Under such small distance perturbations, the increase in the electric field between the tip and sample is not likely to be a major factor (given that applied bias is held constant in our measurements). From this we conclude that the rate of vacancy generation is most likely directly correlated to the amount of electrons injected per unit time. Since the tip bias is held constant, the mean energy per tunneling electron remains the same, however the number of tunneling electrons increases as the barrier width (resistance) is reduced. It seems logical to conclude that the corresponding increase in the power dissipated by the tunneling electrons ($P \propto I_{tip}^2$) leads to a corresponding proportional increase in the rate of energy dissipated in the sample through bond breaking at the void edges and the corresponding parabolic increase in the etching rate with respect to current flow (as shown in Figure 4.10b).

However, the vacancy generation source term magnitude (Z) and the phase-field simulated growth rate does not display a parabolic relationship, unlike the experimental growth rate vs current plot (see Figure 4.10b). In Figure 4.10a we have matched the experimental growth rates, taken at various currents, by varying only Z in our model. Yet, in Figure 4.10b we see that the phase-field growth rate is dependent upon the source magnitude (Z) to the power ¼. At this point it is difficult to establish a quantitative relationship between the vacancy source magnitude and the tip current without more exhaustive first-principles kinetic and electron transport simulations [198,199]. The reason behind this difficulty is that since the distance between the sample and the STM tip does not remain constant, the interactions between the tip and the surface of the sample are quite difficult to establish precisely. A detailed first-principles analysis of this rich and intriguing physics is left for future work.

4.4. Conclusion

In this work, we observed a non-linear (parabolic) area growth behavior with respect to time and a shape evolution from triangular to hexagonal in monolayer vacancy islands on $TiSe_2$ surfaces under STM scanning. This intriguing 2D material behavior is quite different from the linear area growth usually expected from the bulk diffusion of vacancies. The growth rates were measured at various tunneling currents and determined to be directly correlated with preferential electrical stressing by the STM tip at vacancy island edges. A phase-field model is used to simulate the growth behavior of a triangular void that is formed during the annealing of the $TiSe_2$ and its diffusional growth when exposed to electrical stressing by a STM tip. Good agreement was obtained between observed experimental results and simulated growth, by using a vacancy source term preferentially acting at the void edges in the equation of motion of the vacancy concentration field. However, a deeper understanding of the governing kinetics and electron transport phenomena requires further detailed first-principles simulations. Nevertheless, the model demonstrates that the observed growth rates are driven by interfacial adatom dissociation through excitation by an STM tip. These results could likely impact our understanding of the reliability of TMDs in electronic devices, when exposed to electrical stressing in realistic operating conditions. This includes vertical gating fields and tunneling currents in novel TMD transistor designs (analogous to the vertical STM induced stressing studied in this work). Importantly, our work suggests the non-linear (parabolic) void growth observed could result in reduced 2D TMD device lifetimes, from that expected via conventional linear bulk diffusional growth law estimates.

Chapter 5. Visualization of Point Defects in Ultrathin Layered 1T-$PtSe_2$

This work is published on 2D Materials [200]. In this work I did all the experiment, draw the schematic structure, STM/STS images and formation energy plot in figures 5.1-5.3, 5.5, 5.6, wrote the whole "Introduction" and "Conclusion" sections and the experiment part of "Method" and "Result and Discussions" sections.

5.1. Intruduction

Transition-metal dichalcogenides (TMDs) with a general formula of MX_2, where M represents transition metal elements (groups 4-10) and X represents chalcogen elements (S, Se or Te), are a family of two-dimensional (2D) materials being extensively studied in the past few years [34,157,201,202]. A single TMD layer consists of a hexagonal layer of the M atoms sandwiched between two hexagonal layers of the X atoms. Neighboring TMD layers are typically coupled via a weak van der Waals interaction. Depending on the number of *d* electrons and thickness, TMDs can have a variety of electronic properties, namely metallic, semimetallic, semiconducting and superconducting [33,203]. Physical and chemical properties of these 2D materials are markedly different from their bulk counterparts and can be tuned for wide ranges of applications [204-207].

So far, studies on TMDs have been mostly conducted on MX_2 with group VIB transition metals, such as M = Mo, W, and X = S, Se. Recently a new type of TMD, platinum diselenide ($PtSe_2$) in a 1T structure (Figure 5.1a), has been synthesized in bulk form and ultrathin layers [34,208-210]. Compared to the well-studied TMDs, 1T-$PtSe_2$ has inversion symmetry and it has stronger coupling between neighboring unit layers. Furthermore, this material is unique in the sense that a transition from indirect-gap semiconductor to metal can be driven by simply varying thickness [211]. Among all the TMDs, $PtSe_2$ has the highest Seeback coefficient good for thermoelectric applications [212] and the extremely high mobility, up to 3000 $cm^2/V/s$, desirable for electronic applications [32]. $PtSe_2$ can be also used in catalysis [34,213] and as efficient gas sensors because of low adsorption energies for gases like NO, CO, CO_2 and H_2O [33]. In monolayer 1T-$PtSe_2$ layer, spin polarization induced by a local Rashba effect was recently observed [210].

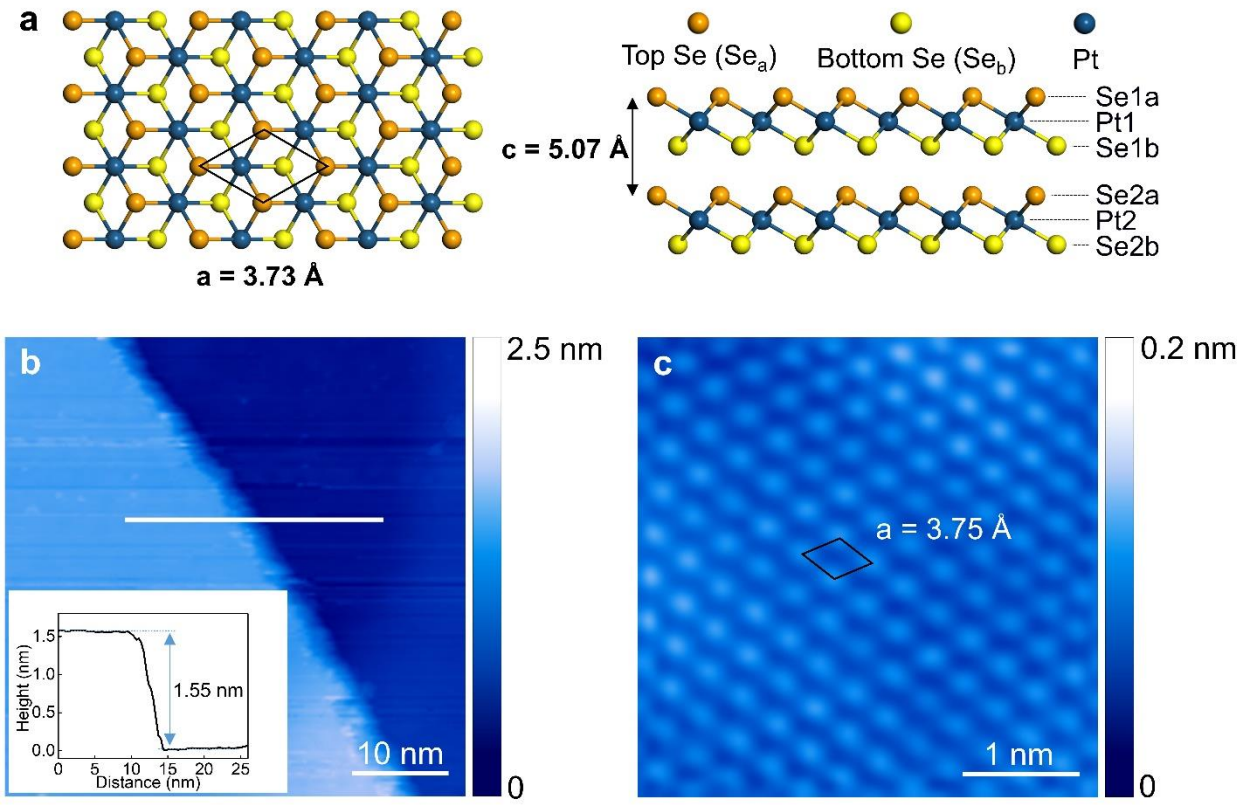

Figure 5.1. (a) Structure model of 1T-$PtSe_2$. (b) Large scale STM image of a few-layer $PtSe_2$ flake, including a step edge indicating that the left area is three-layer thicker than the right area (V_s = 2.0 V, I = 0.3 nA). Inset: line profile along the marked line in the STM image. (c) Atomically resolved STM image of 1T-$PtSe_2$ surface (V_s = 0.3 V, I = 0.6 nA).

Defects are ubiquitous in 2D TMDs, especially those synthesized via chemical vapor deposition (CVD) or transport (CVT) [214,215]. Some defects appear from growth or annealing processes [216], whereas some other defects are naturally or intentionally brought into the structure during investigation [217]. In 2D materials, typical zero-dimensional or point defects constitute vacancies, antisites, adatoms, intercalations, interstitial dopants, and substitutional dopants [157,158], while one-dimensional defects include grain boundaries, dislocations, and edges [84,171,218]. Properties of 2D TMDs are very sensitive to defects, especially for 2D semimetals and semiconductors [70,217,219-221]. Depending on the properties of interest and desirable applications, defects can be beneficial or detrimental. For instance, 60˚ twin grain boundaries in

molybdenum and tungsten dichalcogenides can function as metal wires (conducting pathways) or sinks for carriers [222]. Point defects typically lower the carrier mobility or degrade mechanical properties of 2D materials [223]. On the other hand, under certain conditions, point defects can also be sources of single photon emission [202,224] and induce large spin-orbit splitting in 1T TMDs [83,225].

Despite the ubiquity and importance of defects [226], there are no experimental studies of defects in 1T-$PtSe_2$ layers at the atomistic level yet. Here we investigate intrinsic point defects for ultrathin 1T-$PtSe_2$ layers grown on mica through the CVT method, by using scanning tunneling microscopy and spectroscopy (STM/STS) and first-principles calculations. Point defects were formed in the structure of 1T-$PtSe_2$ during the growth process. As shown in Figure 5.1a, in a 1T structure, $PtSe_2$ monolayers are stacked in a fashion of A-A. Through STM/STS, we identified five types of dominant point defects and obtained their atomic structures and local density of states. We determined characteristics and formation energies of the defects by using density-functional theory (DFT). Our results may stimulate studies of effects of defects on electronic and optical properties and defect engineering for applications in this interesting new ultrathin 1T-$PtSe_2$ and other 2D TMDs.

5.2. Methods

5.2.1. Experiment

Ultrathin $PtSe_2$ flakes were grown on a mica substrate by the CVT method at a growth temperature of 600-700 ^{o}C. The detailed procedures were reported in our previous papers [123,227]. Then a stripe of 100-nm thick gold film was evaporated through a shadow mask on the samples as electrodes. The samples were annealed at 250 ℃ for 2.5 hours in the preparation chamber in a customized Omicron LT STM/AFM system with a base pressure of low 10^{-10} mbar before transferring it into the STM analysis chamber that is connected to the preparation chamber. In the

main text, all the STM and STS results were carried out in the customized Omicron STM/AFM system and all the measurements were performed at 77 K. STM imaging was carried out at a constant current mode, and STS measurements were done at an open feedback loop using a bias modulation 20 mV with the frequency of 1000 Hz.

5.2.2. Simulation

DFT-based simulations were performed including spin-orbit coupling (unless specified otherwise) using VASP [228,229]. We employed local-density approximation (LDA) [230] for the exchange-correlation functional and used projector-augmented wave (PAW) pseudopotentials [231]. We chose LDA because it gives both in-plane and out-of-plane lattice constants of bulk $PtSe_2$ closer to the experimental values [232-234] than the Perdew-Burke-Ernzerhof (PBE) generalized-gradient approximation (GGA) [235] upon geometry relaxation, as reported in Refs. [236,237]. The PBE-optimized out-of-plane lattice constant *c* for bulk is 27-29% larger than the experimental value, as shown in the literature [236,237]. The energy cut-off and number of *k*-points used in Refs. [236,237] are as follows: 70 Ry with 13×13×1 *k*-points for slabs and 800 eV with 11×11×6 *k*-points for bulk. Furthermore, with the PBE-optimized *c* value, a band gap opens for bulk $PtSe_2$ [236], which is inconsistent with the experimental observation [238,239]. There are also conflicting results [236,237] in the improvement of the out-of-plane lattice constant when van der Waals interaction [240,241] is included within PBE-GGA.

A surface of a thin $PtSe_2$ film was modeled by two 1T-$PtSe_2$ monolayers. Supercells of 5×5 surface atoms were used except for the Pt2 vacancy defect (discussed later), in order to simulate isolated defects. The energy cutoff was set to 260 eV and a k-point mesh of 5×5×1 was used. We fully relaxed the supercell structures until the residual forces were less than 0.01 eV/Å. For the Pt2 vacancy defect, a 7×7 in-plane supercell was used to simulate large-area modulations of the observed STM image near the defect site. Only in this case, spin-orbit coupling was turned off, and an energy cutoff of 230 eV and a k-point mesh of 3×3×1 were employed. For the slab calculations, we included a vacuum layer thicker than 20 Å to avoid interactions between successive images of $PtSe_2$ layers.

To compare with the STM topographic images, applying Tersoff-Hamman approach [242,243], we integrated the DFT-calculated surface local density of states (LDOS) from the Fermi level to the experimental bias voltage at a plane z = 1 Å above the topmost atomic layer. Although isosurfaces of the integrated LDOS corresponding to constant current are more accurate, the method we applied has been used as a good approximation to STM topographic images in the literature [244-246]. The integrated LDOS images were visualized using VESTA [247]. We also calculated formation energies of various defects using the standard method discussed in Ref. [248].

Defect formation energy was calculated using the following formula [249]:

$$E_f = E_{defect} - E_{pristine} - \Sigma_i n_i \mu_i \quad (1)$$

where E_{defect} and $E_{pristine}$ are total energies with and without a defect, respectively, μ_i is a chemical potential of the i^{th} atomic species, and n_i is the number of added i^{th} atoms by the defect ($n_i < 0$ if the atoms are removed). The chemical potential of each atomic species depends on materials growth conditions. The bounds of the chemical potentials are determined from the following conditions:

$$\mu_{Pt} + 2\mu_{Se} = \mu_{PtSe2},$$

$$\mu_i \leq \mu_i^{bulk}, \quad (2)$$

where μ_{PtSe2} is the energy of pristine $PtSe_2$ per formula unit, and μ_i^{bulk} is the bulk chemical potential of the i^{th} species. The second inequality gives the upper bound of the chemical potential and indicates that the chemical potential of each atomic species during the synthesis cannot be greater than the chemical potential of the corresponding stable bulk state, since otherwise elemental bulk would be grown rather than desired $PtSe_2$. Now combining the first equation (which is from the law of mass action) with the inequality, we set the lower bound of the chemical potential. Thus, the chemical potentials are confined within a specific range and the two extreme cases are Se rich ($\mu_{Se} = \mu_{Se}^{bulk}$) and Pt rich ($\mu_{Pt} = \mu_{Pt}^{bulk}$) conditions.

5.3. Result and Discussion

5.3.1. STM topographic images

The atomic structure of 1cT-$PtSe_2$ is schematically drawn in Figure 5.1a. We used atomic force microscope (AFM) and STM to determine the number of layers of $PtSe_2$ flakes (Figure 5.1b). Considering the reported thickness of a single $PtSe_2$ layer, 0.507 nm [233], we determined that the thickness of flakes in our measurements ranges from 5 to 9 layers. A high-resolution STM topographic image of a defect-free 1T-$PtSe_2$ surface is shown in Figure 5.1c. Similar to previous STM study on monolayer $PtSe_2$ grown though selenization of a Pt(111) substrate and other transition-metal diselenides [34,159], the hexagonal protrusions in Figure 5.1c represent the topmost Se atoms. From the arrangement of the surface Se atoms, the in-plane lattice constant of 1T-$PtSe_2$ is determined to be 0.375 ± 0.003 nm, which is consistent with previous theoretical and experimental results [34,213,250]. Figure 5.2 is an atomically resolved large scale STM image of an area of $PtSe_2$ surface showing various types of defects. Figures 5.2a and 5.2b are the STM images of the same area obtained at positive (empty states) and negative sample bias voltages (filled states), respectively. These defects can be visualized at the surface with distinct atomic structures and morphologies at a given bias voltage, marked by arrows in Figure 5.2. The morphology of some types of defects reveals a clear dependence on bias voltage. Combining the defect morphology at the filled and empty states, we identified five dominant types of point defects at the $PtSe_2$ surface, labeled as A, B, C, D, and E, as shown in Figure 5.2. Considering the shape of each defect in a single-crystalline flake as a triangle except for defect A, we noticed that each defect type has the same orientation. In addition to these five defect types, we occasionally observed a few other defects which can be either combined or new defects. For simplicity, we focus on these five dominant types of defects.

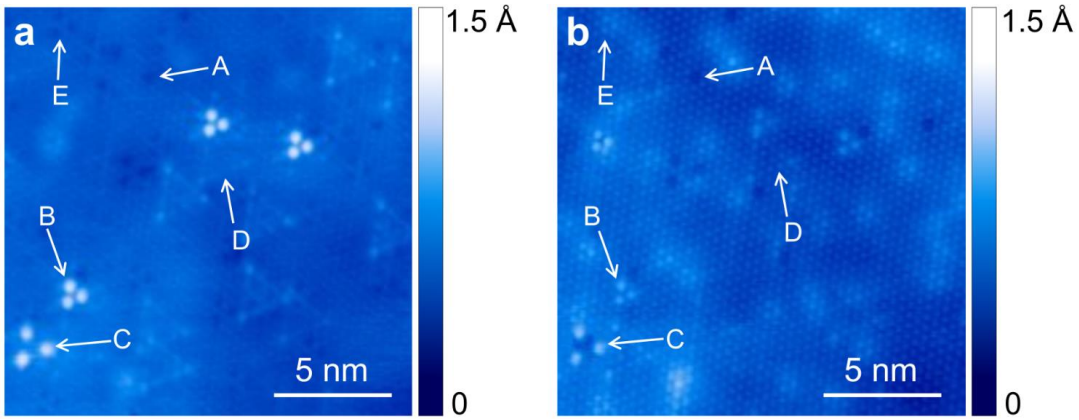

Figure 5.2. STM micrographs of $PtSe_2$ film at 77K. (a) Empty-state image (V_s = 0.4 V, I = 0.7 nA) and (b) Filled-state image (V_s = − 0.4 V, I = 0.7 nA).

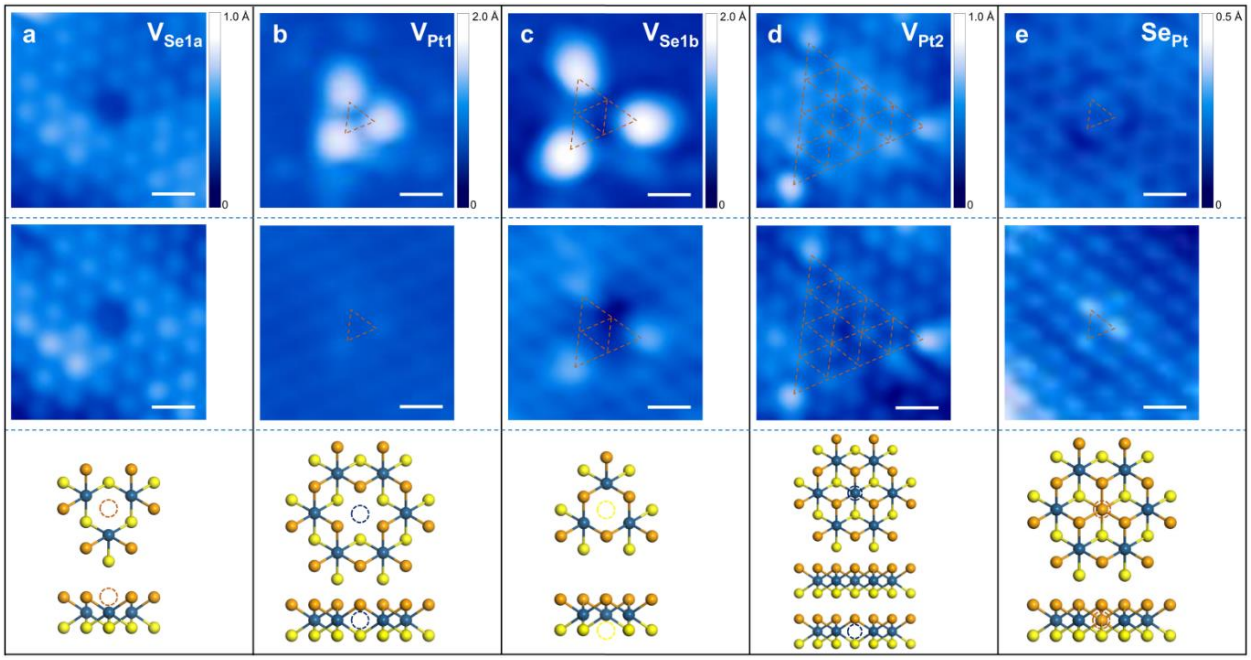

Figure 5.3. Atomically resolved STM images of five types of defects. Top panel: Empty-state images. (a) Type A (V_s = 0.3 V, I = 0.7 nA). (b) Type B (V_s = 0.2 V, I = 0.7 nA). (c) Type C (V_s = 0.2 V, I = 0.7 nA). (d) Type D (V_s = 0.085 V, I = 0.7 nA). (e) Type E (V_s = 0.3 V, I = 0.7 nA). Middle panel: Filled-state images. (a) Type A (V_s = − 0.3 V, I = 0.7 nA). (b) Type B (V_s = − 0.1 V, I = 0.7 nA). (c) Type C (V_s = − 0.2 V, I = 0.7 nA). (d) Type D (V_s = − 0.1 V, I = 0.7 nA). (e) Type E (V_s = − 0.3 V, I = 0.7 nA). The dashed lines indicate the size of defects in term of the lattice constant, appearing as 1×1, 2×2 and 4×4 triangles in (b), (c) and (d), respectively. Bottom panel: Top and side view of the models of each type of defects shown in the top and middle panels. The scale bar on the images is 0.5 nm.

Figures 5.3a-e show zoom-in STM images of the five defect types. Defects of type A appear like depressions at both positive and negative bias voltages. Defects of type B, C, and D look like protrusions at both positive and negative bias voltages. For defects of type E, protrusions (depressions) are shown at negative (positive) bias voltages. All these types of defects have three-fold symmetry. Defects of type A are centered at Se_{top} sites, while defects of type B, C, D, and E are centered at Pt, Se_{bottom}, Pt and Pt sites, respectively, where Se_{bottom} (Se_{top}) is the bottom (top) Se site of the topmost monolayer, as marked by the dashed triangles in Figure 5.3. In addition to

their different sizes, defect type B is centered at Pt site in the topmost monolayer while defect type D is centered at Pt site in the second topmost monolayer. Table 1 lists the density of these defects obtained by averaging over STM images of typical regions each with an area of 20×20 nm^2. Among these five types, defects of type E have the highest density. We now discuss each defect type separately.

Table 1. Densities of defects obtained from STM and STEM measurements.

Defects	Density obtained from STM images ($1/cm^2 \times 10^{12}$)
A (V_{Se1})	2.2 ± 2.0
B (V_{Pt1})	1.2 ± 0.4
C (V_{Se2})	1.2 ± 0.6
D (V_{Pt2})	3.1 ± 1
E (Se_{Pt})	16.4 ± 3.9

Defects of type A show one-site depressions at the surface at both positive and negative bias (Figure 5.3a). There is not a much difference in the brightness of the STM images at various bias voltages. This defect type could be due to a missing Se atom on the surface of the topmost $PtSe_2$ layer, in other words, a Se vacancy in the top Se layer, labeled as V_{Se1a}.

Defects of type B show 1×1 triangular protrusions at both positive and negative bias voltages, although the protrusions are much more apparent at positive bias voltages (Figure 5.3b). There are a few factors affecting tunneling current, such as the height of the atoms at the surface and integrated local density of states [243,251]. Typically, the higher surface atoms or larger integrated local density of states result in protrusions in STM images. Despite this difficulty, our observation suggests that the defects of type B are electron acceptor defects. Since we cannot determine the

orientation of 1-T structure from the top Se layer, each of the three sites may be associated with either (i) Se substituted by a more electronegative element at the bottom atomic layer of the topmost monolayer, or (ii) a Pt vacancy (V_{Pt1}) located at the topmost monolayer, noted as Pt1 in Figure 5.1a. Option (i) is, however, ruled out since there were no other observable more electronegative elements than Se in the growth environment. Option (ii) is more promising since the growth was under a Se-rich condition. The Pt vacancy can build a high acceptor density at the three neighboring Se sites forming the triangle, giving rise to the three protrusions at positive bias. This analysis is supported by our DFT calculations, as explained later.

Defects of type C show 2×2 triangular protrusions at both positive and negative bias voltages (Figure 5.3c), although the protrusions are much more apparent at positive bias voltages, similarly to defects of type B. Considering that the defects of type C are centered at the bottom Se atoms, we come up with three candidates for the origin of such a defect, such as a bottom Se atom replaced by Pt ($Pt_{antisite}$, Pt_{Se1b}), a bottom Se atom vacancy (V_{Se1b}), or three neighboring Pt vacancies around the center bottom Se atom (V_{3Pt}). Different from MoS_2 or $TiSe_2$, O-substituted defects were not observed in our measurements [157,252].

Defects of type D show 4×4 triangular protrusions at both positive and negative bias voltages (Figure 5.3d), and they are centered at Pt sites just like the defects of type B. Protrusions are more prominent at the vertices of the triangles, but they are not as strong as those for the defects of type B and C at positive bias voltages. Compared with the defects of type B and C, topographic images do not show much contrast between positive and negative bias voltages.

Defects of type E appear as 1×1 triangular protrusions at negative bias, and show the same triangular protrusion surrounded by depressions at positive bias (Figure 5.3e). Among the five defect types, this type appears with the highest density (Table 1), which is consistent with the DFT-calculated formation energies of defects discussed later. This finding in 1T-$PtSe_2$ layers is in contrast to the trend of defects in group VIB TMD MoS_2 family layers where vacancies are the most dominant defects in either Mo- or S-rich condition [202].

5.3.2. DFT simulations of integrated LDOS

In order to determine the characteristics of the five defect types, we performed DFT calculations. We considered all possible intrinsic single point defects within a $PtSe_2$ slab of two monolayers as well as Se adsorption based on the Se-rich growth condition. Within each atomic layer, two types of single point defects, vacancy and antisite, were considered. In addition, intercalation of a Se or a Pt atom within the van der Waals gap was taken into account. Although the experimental sample flakes are about five to nine monolayers thick, such thick slabs including defects cannot be simulated due to high computational cost. We calculated the total DOS for the pristine bilayer and six monolayer using the LDA-optimized geometries.

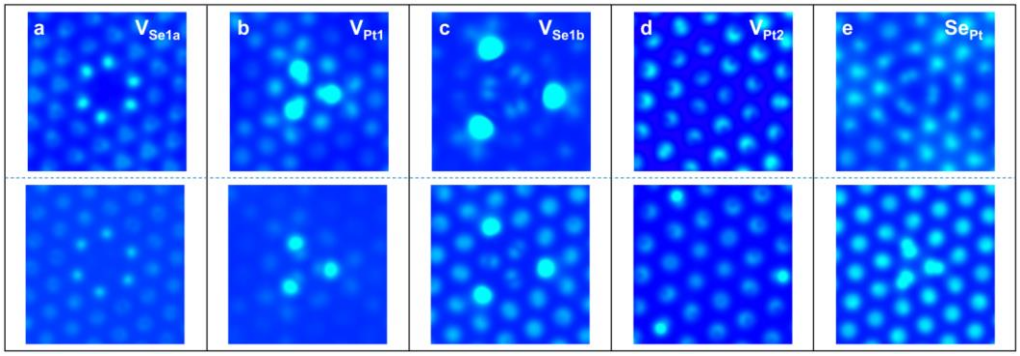

Figure 5.4. DFT-calculated integrated local density of states for the five types of defects. Top panel: Empty-state images. (a) Type A at 0.25 eV. (b) Type B at 0.15 eV. (c) Type C at 0.2 eV. (d) Type D at 0.085 eV. (e) Type E at 0.15 eV. Bottom panel: Filled-state images. (a) Type A at − 0.3 eV. (b) Type B at − 0.1 eV. (c) Type C at − 0.2 eV. (d) Type D at – 0.1 eV. (e) Type E at − 0.3 eV.

Figure 5.4 shows integrated LDOS images for five distinct types of defects which are closest to the experimental STM images of defect types A-E at positive and negative bias voltages. These images as well as our calculated formation energies (Sec. III. C) bolster the identification of each observed defect type. According to the DFT-calculated LDOS images, defect types A-E correspond to V_{Se1a}, V_{Pt1}, V_{Se1b}, V_{Pt2} and Se_{Pt1}, respectively.

Defects of type A are indeed from one missing atom at the topmost Se layer, V_{Se1a}, clearly seen in both experimental images and integrated LDOS (Figures 5.3a and 5.4a). In various TMDs [157-

159,253,254], defects of this type are the most abundant and produce electron trap states within the band gap.

For defects of type B, our integrated LDOS images show that V_{Pt1} produces 1×1 triangular protrusions at positive and negative bias (Figure 5.4b), similarly to the experimental STM images. We also found that after the structural relaxation, three nearest neighboring Se atoms at the topmost Se layer around the Pt vacancy site are expanded outward in plane (~ 0.3 Å) and vertically (~ 0.1 Å) due to the missing bonds between the Pt and Se atoms. This topographic effect explains why the STM images for defects of type B show 1×1 bright triangular shapes at both negative and positive bias as well as the small expansion of the in-plane lattice constant in the triangular protrusions.

For defects of type C, among the three aforementioned possibilities (Pt_{Se1b}, V_{Se1b}, V_{3Pt}), we found that V_{Se1b} produces the 2×2 triangular protrusions similar to those observed in the STM images at positive and negative bias (Figure 5.4c). Unlike the case of type B defects, changes in the atomic positions near the defect site were negligible upon the structural relaxation. Therefore, the observed STM image is likely to be determined by the influence of the defects on the nearby electronic structure, rather than by mere topographic changes.

The integrated LDOS images confirm that defects type D arise from V_{Pt2}. From the simulations, we observe 4×4 triangular protrusions at positive and negative bias voltages (Figure 5.4d). The three Se atoms at the vertices of the triangle are vertically shifted upward by about 0.04 Å, which explains moderately bright protrusions at both positive and negative bias.

The observed STM images for defect type E agree with the integrated LDOS images of Se_{Pt1} defects (Figure 5.4e), although the effect of defect type E is quite subtle. Qualitative features such as 1×1 triangular protrusions at both negative and positive bias voltages and the surrounding depressions at positive bias are close to those of the experimental images.

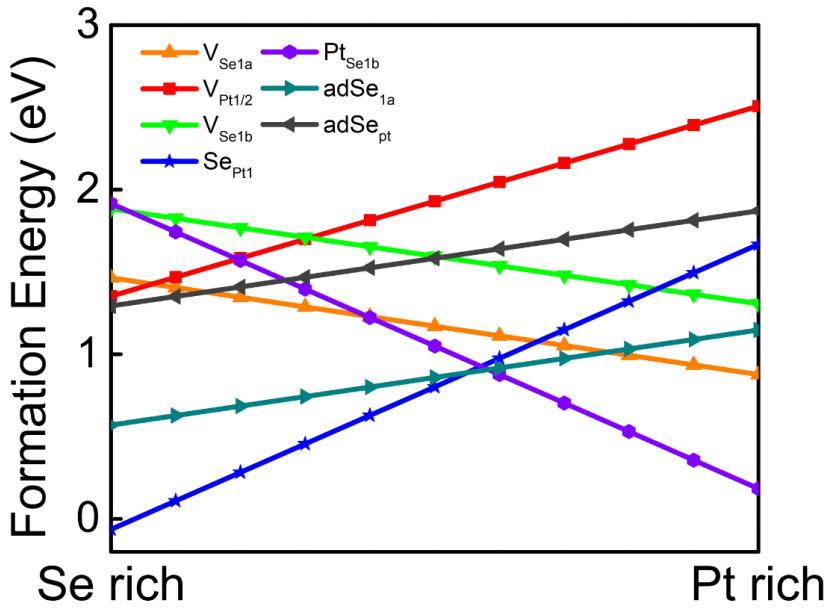

Figure 5.5. Calculated defect formation energies. $adSe_{pt1}$ and $adSe_{1a}$ indicate Se adatoms at the hollow site above Pt atoms and the top site above Se_{1a} atoms, respectively. The case of Se adatom at the hollow site above Se_{1b} atoms gives a very similar result to the $adSe_{1a}$ case and not shown here. V_{Pt1} and V_{Pt2} have the same formation energies.

5.3.3. DFT calculations of defect formation energies

For a better understanding of stability of different defect types, we calculated the formation energies of all the defect types we considered in this work, as shown in Figure 5.5. The formation energy values at the extreme Se-rich and Pt-rich conditions for all defect types are listed in Table 5.2. Since we calculated the formation energies for a $PtSe_2$ bilayer with inversion symmetry, Pt1 and Pt2 atoms are equivalent to each other and the formation energies of V_{Pt1} and V_{Pt2} are the same in our calculations. The formation energies of some defect types are not shown in Figure 5.5 but listed in Table 5.2, because their formation energies are much higher than the other observed defects. Our calculated formation energies agree with the STM experimental densities of defects listed in Table 1, although the experimental sample flakes are thicker than a bilayer. For instance,

in a Se-rich condition, the formation energy of Se_{Pt1} defect alone is well below the formation energies of other defects, becoming negative in the extreme Se rich case. In our sample grown under a Se-rich condition, defect type E turns out to have the highest density as observed in experiments (Table 1), and that the integrated LDOS images (Figure 5.4e) suggest that defect type E arises from the Se_{Pt} antisite defect. In addition, Table 1 shows that the density of defect type A is higher than that of defect type C. This agrees with our result that the formation energy of defect type A is noticeably lower than that of defect type C (Figure 5.5).

Some defect types shown in Figure 5.5 and Table 5.2 have low formation energies but they have not been observed in the STM experiment. For example, Se adatoms (at the hollow Se site, hollow Pt site, and on top site) have not been observed, although their formation energies are significantly lower than those of the observed defect types. This could be due to the annealing process done before transferring into the STM analysis chamber.

Defect	Se rich	Pt rich
Se antisite at Pt site	− 0.064 eV	1.668 eV
Se adatom hollow Se_{1b} site*	0.566 eV	1.144 eV
Se adatom top site*	0.570 eV	1.148 eV
Se adatom hollow Pt site*	1.294 eV	1.872 eV
Pt_1 vacancy	1.353 eV	2.508 eV
Se_{1a} vacancy	1.464 eV	0.877 eV
Se_{1b} vacancy	1.884 eV	1.307 eV
Pt antisite at Se_{1b} site	1.916 eV	0.184 eV
Se intercalation	2.983 eV	3.561 eV
Pt antisite at Se_{1a} site*	3.593 eV	1.861 eV
Three Pt vacancy*	4.230 eV	7.693 eV
Pt intercalation	21.636 eV	20.481 eV

Table 5.2. Defect formation energies of the considered defect types are tabulated in the ascending order of the formation energy in the Se rich condition, which is relevant to the growth condition of our sample. Except for adatom cases (which might be removed due to annealing), all defect types up to Se_{1b} vacancy are observed in the STM experiment, and other defects with higher formation energies are not observed. Se adatom at bridge site is also simulated. However, in this case, the Se adatom moves toward a hollow site upon relaxation, which indicates that hollow sites are more stable than the bridge site. For the defect types marked by an asterisk, a 3×3×1 k-mesh is used. Other computational details are explained in the main text.

5.3.4. STS analysis

To characterize the electronic structures near the defects, we performed STS measurements on both defect-free and defect-rich areas. Figure 5.6 shows dI/dV spectra of pristine areas and defect-rich areas with types A-E with a thickness of six monolayers, in the voltage range of − 0.8 V to

0.8 V. For the defect-free areas (see Figure 5.1c) the V-like shaped dI/dV spectrum has much higher density of states (DOS) at empty states than at filled states with a rather wide region of low DOS near the Fermi level. This feature indicates that pristine $PtSe_2$ is semi-metallic at the thickness down to six layers, which is consistent with the reported experimental data [238]. The dI/dV spectra of the defects were measured at the center for defect type A and at the corner protrusions of defect types B, C, D and E, respectively. We also measured the STS at the centers of the defects, and found less prominent features compared with those measured at the protrusions, especially for V_{Pt2} defects. Each dI/dV curve was obtained by averaging over 15 spectra. Due to the metallic nature of the $PtSe_2$ flakes, the dI/dV peaks for the defect-rich regions are not as prominent as those for typical semiconducting layers with defects.

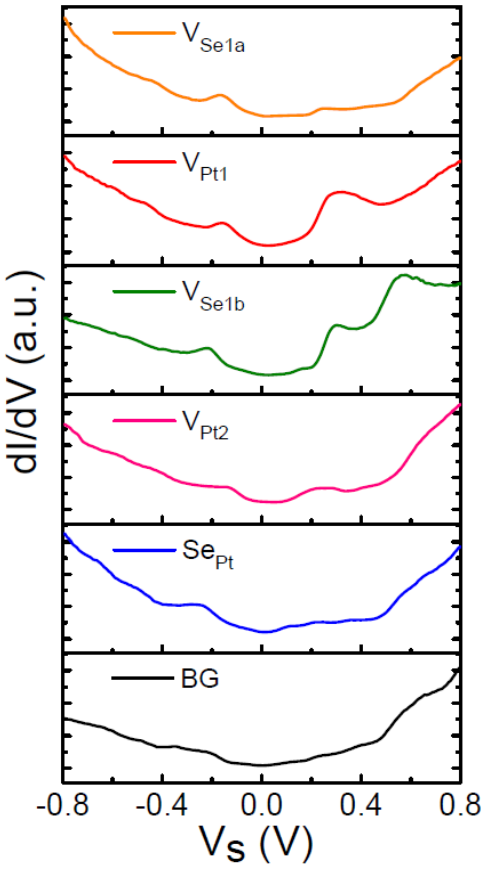

Figure 5.6. STS of six-layer $PtSe_2$ with and without defects. The top five panels are for the layer with defects, while the bottommost panel is for the pristine layer.

5.4. Conclusion

We investigated intrinsic point defects in ultrathin $PtSe_2$ layers grown via the CVT method, by using STM/STS and first-principles calculations. We observed and identified five dominant types of point defects, such as V_{Se1a}, V_{Pt1}, V_{Se1b}, V_{Pt2} and Se_{Pt1}. We calculated the formation energies of these defect types and compared them with the densities of the defects observed in experiments. The relative densities of the dominant defect types are in good agreement with the calculated formation energies. The experimental data and theoretical results suggest that Se_{Pt1} antisite defects are the most abundant with the lowest formation energy in the Se-rich condition. Our findings elucidate the modification of electronic structures from the point defects, which would be crucial for optimizing the growth of ultrathin $PtSe_2$ layers and designing future electronic and spintronic devices.

5.5. Supporting Information

5.5.1. Extra experimental data

$PtSe_2$ layers were synthesized on mica substrates, with a triangular or hexagonal shape, shown in light color in figure 5.7a. Figure 5.7b is a zoom-in image of the marked area in figure 5.7a, indicating the thickness of the flake is 9 $PtSe_2$ layers. As shown in figure 5.8, $PtSe_2$ flakes are with various thickness, since there is a height difference between the layers (part 1 versus part 2 in figures 5.8a and 5.8b). The step height on the mentioned area of $PtSe_2$ flakes shows 1.55 nm height difference between two areas of $PtSe_2$ which means the left (part1) part is about 3 layers of $PtSe_2$ higher than the right part (part2). Figures 5.8c and 5.8d are atomically resolved STM images of part 1 and part 2, clearly showing that the crystallographic orientations of these two parts are with an 180˚ rotation. In the following images, we try to provide additional information about the position of defects and the nature of them. Figure 5.9a shows an STM image of the surface of an 1T-$PtSe_2$ flake, and figure 5.9b is the same image with an atomic model of $PtSe_2$ overlapped on it for determine the atomic position of the defects. Note that figure 5.9 was obtained at room

temperature and all the rest of STM or STS data were at 77K. There is a high resolution scanning transmission electron microscopy (STEM) image (figure 5.10). As shown in this image, there are some defects marked by green circles being attributed to defects type A and C, and also those marked by yellow circles are attributed to defects type B and D. As defects of type A and C are both at Se sites, those could be either V_{Se1a} or V_{Se1b}. Similarly both defects of type B and D are at Pt sites. However, we did not see the effect of defect type E in the STEM image. It is mainly due to the thickness of the flake, 5 layers, used for taking the electron microscopy image. Defect formation energies of the considered defect types are tabulated in the ascending order of the formation energy in the Se rich condition (Table 5.3), which is relevant to the growth condition of our sample. Total density of states of the pristine bilayer and six-monolayer $PtSe_2$ from the LDA-optimized geometries are shown in figure 5.11. PDOS from Pt and Se atoms for the DFT-optimized pristine $PtSe_2$ bilayer are shown in figure 5.12. We provide additional DFT-calculated integrated LDOS for each type of the defects at different bias voltages in figure 5.13. Figures 5.14 and 5.15 show STS obtained at different positions. Figure 5.16 shows a double vacancy in top Se layer.

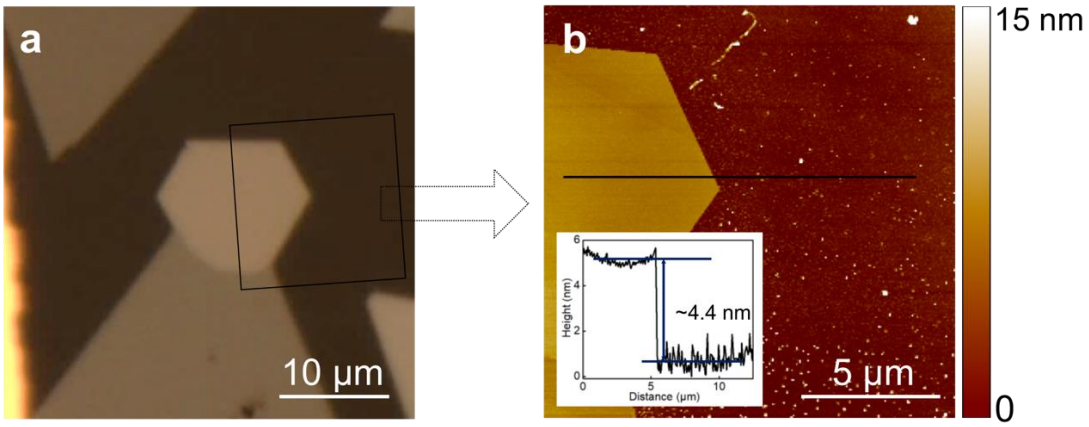

Figure 5.7. (a) Optical image of a flake with similar color to the higher part shown in figure 1b. (b) AFM image of the area marked by the square in (a). Inset: line profile along the marked line.

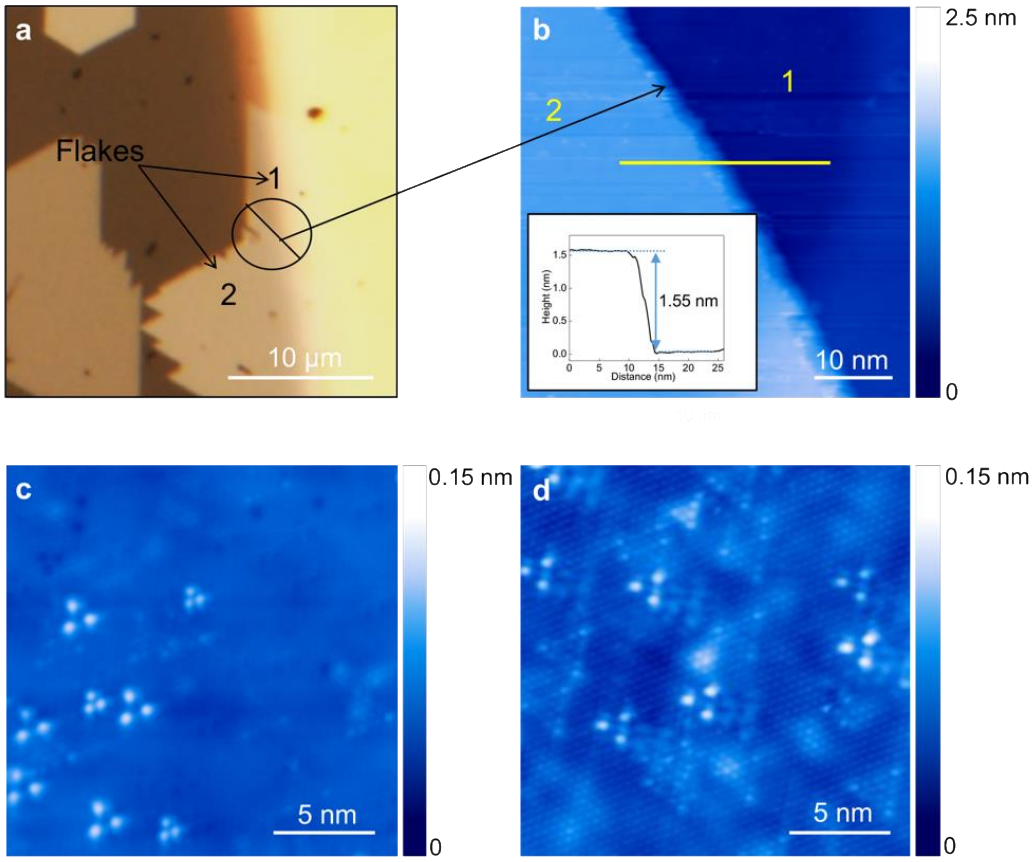

Figure 5.8. (a) Optical image of flakes with thickness of 9 and 6 layers, labeled as 2 and 1, respectively. (b) STM image of the area marked by the circle in (a) (V_s = 2.0 V, I = 0.3 nA). Inset: line profile along the marked yellow line. (c) and (d) Atomically resolved STM images of the higher part (V_s = 0.7 V, I = 0.7 nA) and the lower part in (b) (V_s = 0.3 V, I = 0.5 nA). The defects in the higher part show opposite orientation compared with those in the lower part.

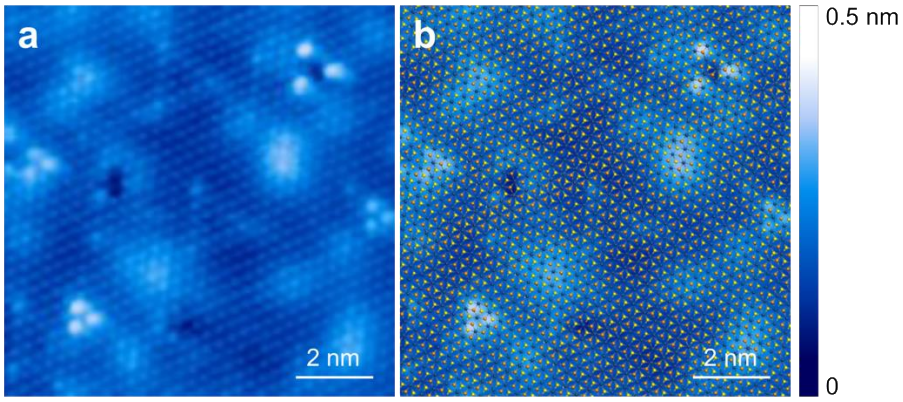

Figure 5.9. (a) STM image and (b) the same image with atomic model overlaid on it ($V_s = -0.4$ V, I = 0.5 nA).

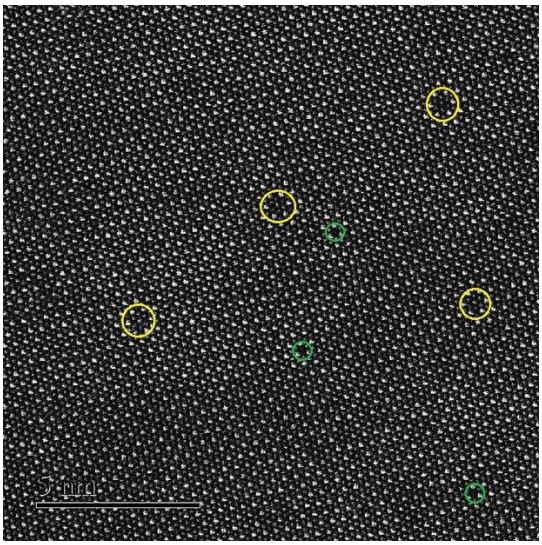

Figure 5.10. High resolution transmission electron microscopy image of a 5-layer 1T-$PtSe_2$.

5.5.2. DFT calculations of formation energies

Defect formation energy was calculated using the following formula [249]:

$$E_f = E_{defect} - E_{pristine} - \Sigma_i n_i \mu_i \quad (1)$$

where E_{defect} and $E_{pristine}$ are total energies with and without a defect, respectively, μ_i is a chemical potential of the i^{th} atomic species, and n_i is the number of added i^{th} atoms by the defect ($n_i < 0$ if the atoms are removed). The chemical potential of each atomic species depends on materials growth conditions. The bounds of the chemical potentials are determined from the following conditions:

$$\mu_{Pt} + 2\mu_{Se} = \mu_{PtSe2},$$

$$\mu_i \leq \mu_i^{bulk}, \quad (2)$$

where μ_{PtSe2} is the energy of pristine $PtSe_2$ per formula unit, and μ_i^{bulk} is the bulk chemical potential of the i^{th} species. The second inequality gives the upper bound of the chemical potential and indicates that the chemical potential of each atomic species during the synthesis cannot be greater than the chemical potential of the corresponding stable bulk state, since otherwise elemental bulk would be grown rather than desired $PtSe_2$. Now combining the first equation (which is from the law of mass action) with the inequality, we set the lower bound of the chemical potential. Thus, the chemical potentials are confined within a specific range and the two extreme cases are Se rich ($\mu_{Se} = \mu_{Se}^{bulk}$) and Pt rich ($\mu_{Pt} = \mu_{Pt}^{bulk}$) conditions. The LDA-calculated formation energies of defects that we considered are shown in Table 5.3.

Defect	Se rich	Pt rich
Se antisite at Pt site	− 0.064 eV	1.668 eV
Se adatom hollow Se_{1b} site*	0.566 eV	1.144 eV
Se adatom top site*	0.570 eV	1.148 eV
Se adatom hollow Pt site*	1.294 eV	1.872 eV
Pt_1 vacancy	1.353 eV	2.508 eV
Se_{1a} vacancy	1.464 eV	0.877 eV
Se_{1b} vacancy	1.884 eV	1.307 eV
Pt antisite at Se_{1b} site	1.916 eV	0.184 eV
Se intercalation	2.983 eV	3.561 eV
Pt antisite at Se_{1a} site*	3.593 eV	1.861 eV
Three Pt vacancy*	4.230 eV	7.693 eV
Pt intercalation	21.636 eV	20.481 eV

Table 5.3. Defect formation energies of the considered defect types are tabulated in the ascending order of the formation energy in the Se rich condition, which is relevant to the growth condition of our sample. Except for adatom cases (which might be removed due to annealing), all defect types up to Se_{1b} vacancy are observed in the STM experiment, and other defects with higher formation energies are not observed. Se adatom at bridge site is also simulated. However, in this case, the Se adatom moves toward a hollow site upon relaxation, which indicates that hollow sites are more stable than the bridge site. For the defect types marked by an asterisk, a 3×3×1 k-mesh is used. Other computational details are explained in the main text.

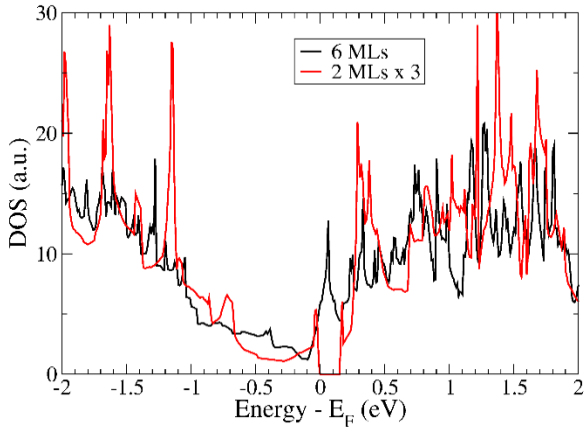

Figure 5.11. Total density of states of the pristine bilayer and six-monolayer $PtSe_2$ from the LDA-optimized geometries. The density of states for the bilayer was scaled by a factor of three for comparison.

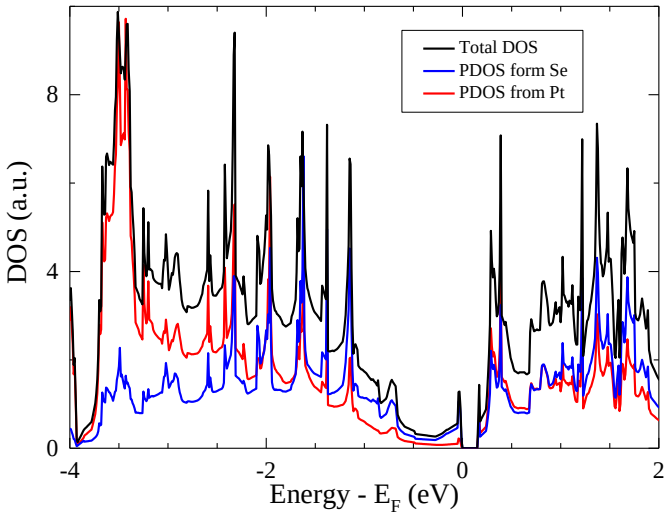

Figure 5.12. Calculated PDOS from Pt and Se atoms for the DFT-optimized pristine $PtSe_2$ bilayer.

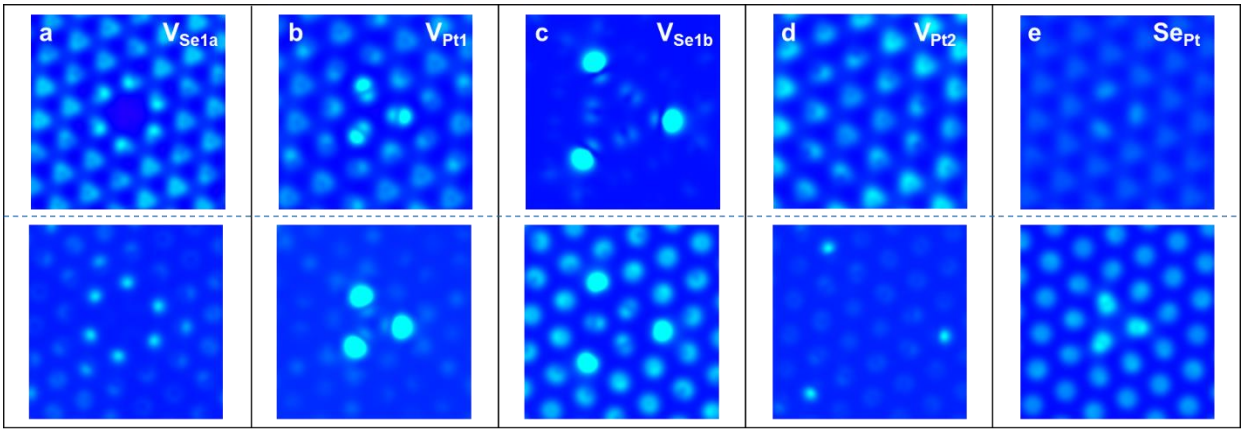

Figure 5.13. Additional DFT-calculated integrated local density of states (LDOS) for the five types of defects at different bias voltages from the experimental data shown in Fig.3 and the simulated LDOS in Fig.4. Top panel: Empty-state images. (a) Type A at 0.4 eV. (b) Type B at 0.4 eV. (c) Type C at 0.1 eV. (d) Type D at 0.2 eV. (e) Type E at 0.4 eV. Bottom panel: Filled-state images. (a) Type A at − 0.1 eV. (b) Type B at − 0.2 eV. (c) Type C at − 0.3 eV. (d) Type D at – 0.1 eV. (e) Type E at − 0.4 eV.

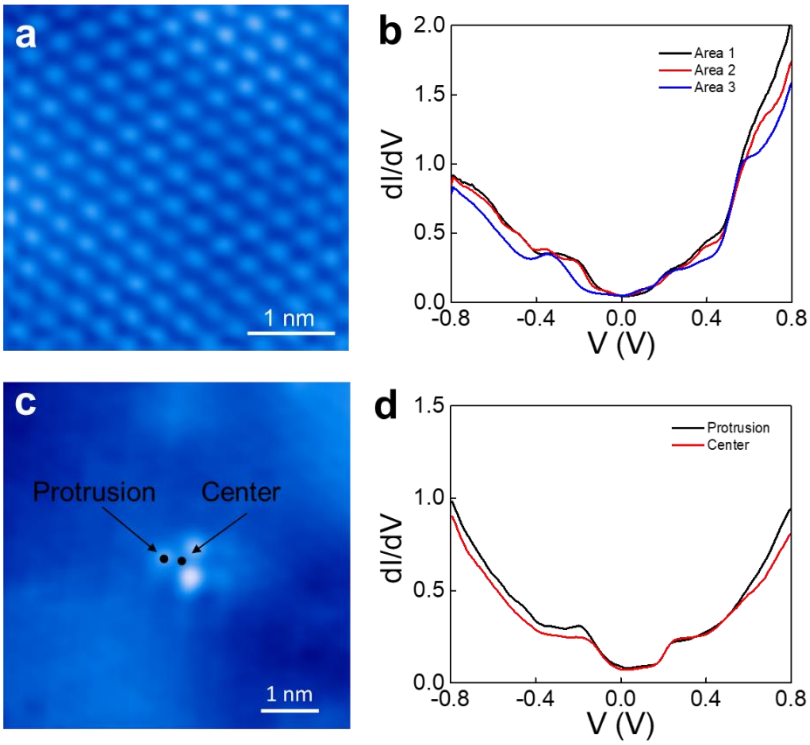

Figure 5.14. STS obtained from different positions. (a) Atomically resolved STM image of a clean 1T-PtSe2 surface (Vs = 0.3 V, I = 0.6 nA). (b) STS obtained at three different areas similar to (a). (c) STM image showing an isolated defect type B (Vs = 0.3 V, I = 0.7 nA). (d) STS obtained from the center and the protrusion.

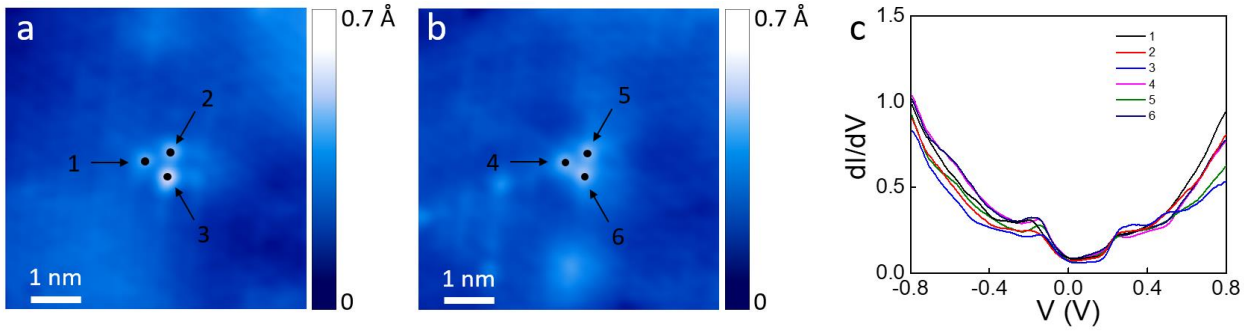

Figure 5.15. STS obtained from different defects of type B defects. (a) STM image showing an isolated type B defect (V_s = 0.3 V, I = 0.7 nA). (b) A type B defect from another area (V_s = 0.3 V, I = 0.7 nA). (c) STS taken from the 6 protruding Se atoms marked in (a) and (b).

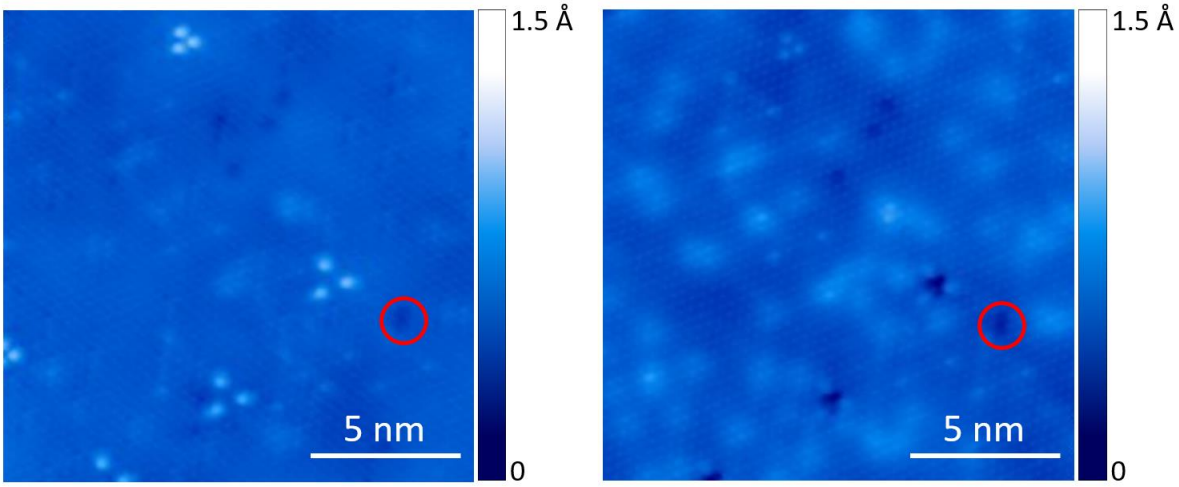

Figure 5.16. STM images showing a Se double vacancy consist of 2 nearest top layer Se atoms missing. (a) Empty-state image (V_s = 0.3 V, I = 0.7 nA) and (b) Filled-state image (V_s = − 0.2 V, I = 0.7 nA).

Conclusion

This dissertation focus on STM study on 2D materials. Two-dimensional TMDCs, such as $TiSe_2$ and $PtSe_2$ are ideal systems for exploring the fundamentals in condensed matter physics.

Although CVT has been widely used to grow bulk TMDCs with high melting point transistion metal for decades, it is the first time to be used for synthesizing 2D TMDCs. By optimizing the growth temperature, growth time, transport agent and growth substrate, the growth rate was significantly lower and thin flakes with controllable thickness is obtained. Large scale RT-STM images showed atomic scale flat surface. At 77K, 2×2 CDW phase was clearly visualized by LT-STM, confirming the high crystallinity. Moreover, in principle, all TMDCs that can be grown in the form of single crystals by CVT can also be grown into 2D form by carefully adjusting the growth parameters as we demonstrated in this work. Therefore, we believe that in parallel with CVD synthesis, CVT approach will become another universal method for growing various 2D atomic crystals to further extend the family of 2D materials.

In the next chapter, we observed that the triangular shape monolayer vacancy islands on $TiSe_2$ evolved to hexagonal shape with a parabolic area growth behavior under STM scanning. Such evolution cannot be explained by vacancies diffusion from the bulk. A phase-field model is used to simulate the growth behavior of a triangular void that is formed during the annealing of the $TiSe_2$ and its diffusional growth when exposed to electrical stressing by a STM tip. Good agreement was obtained between observed experimental results and simulated growth, by using a vacancy source term preferentially acting at the void edges in the equation of motion of the vacancy concentration field. Our work suggests the non-linear (parabolic) void growth observed could result in reduced 2D TMD device lifetimes, from that expected via conventional linear bulk diffusional growth law estimates.

In the last chapter, we investigated intrinsic point defects in ultrathin $PtSe_2$ layers grown via the CVT method, by using STM/STS and first-principles calculations. We observed and identified five dominant types of point defects a are Pt vacancies at the topmost and next monolayers, Se vacancies in the topmost monolayer, and Se antisites at Pt sites within the topmost monolayer. We calculated the formation energies of these defect types and compared them with the densities of

the defects observed in experiments. The relative densities of the dominant defect types are in good agreement with the calculated formation energies. Our findings elucidate the modification of electronic structures from the point defects, which would be crucial for optimizing the growth of ultrathin $PtSe_2$ layers and designing future electronic and spintronic devices.

References

[1] K. S. Novoselov, A. K. Geim, S. V. Morozov, D. Jiang, Y. Zhang, S. V. Dubonos, I. V. Grigorieva, and A. A. Firsov, *Electric field effect in atomically thin carbon films,* Science **306**, 666 (2004).

[2] P. R. Wallace, *The Band Theory of Graphite,* Phys Rev **71**, 622 (1947).

[3] C. Lee, X. D. Wei, J. W. Kysar, and J. Hone, *Measurement of the elastic properties and intrinsic strength of monolayer graphene,* Science **321**, 385 (2008).

[4] E. Stolyarova, K. T. Rim, S. M. Ryu, J. Maultzsch, P. Kim, L. E. Brus, T. F. Heinz, M. S. Hybertsen, and G. W. Flynn, *High-resolution scanning tunneling microscopy imaging of mesoscopic graphene sheets on an insulating surface,* Proc. Natl. Acad. Sci. U.S.A. **104**, 9209 (2007).

[5] S. Bae, H. Kim, Y. Lee, X. F. Xu, J. S. Park, Y. Zheng, J. Balakrishnan, T. Lei, H. R. Kim, Y. I. Song, Y. J. Kim, K. S. Kim, B. Ozyilmaz, J. H. Ahn, B. H. Hong, and S. Iijima, *Roll-to-roll production of 30-inch graphene films for transparent electrodes,* Nat. Nanotechnol. **5**, 574 (2010).

[6] K. I. Bolotin, K. J. Sikes, Z. Jiang, M. Klima, G. Fudenberg, J. Hone, P. Kim, and H. L. Stormer, *Ultrahigh electron mobility in suspended graphene,* Solid State Commun **146**, 351 (2008).

[7] A. A. Balandin, S. Ghosh, W. Z. Bao, I. Calizo, D. Teweldebrhan, F. Miao, and C. N. Lau, *Superior thermal conductivity of single-layer graphene,* Nano Lett. **8**, 902 (2008).

[8] Y. Hernandez, V. Nicolosi, M. Lotya, F. M. Blighe, Z. Y. Sun, S. De, I. T. McGovern, B. Holland, M. Byrne, Y. K. Gun'ko, J. J. Boland, P. Niraj, G. Duesberg, S. Krishnamurthy, R. Goodhue, J. Hutchison, V. Scardaci, A. C. Ferrari, and J. N. Coleman, *High-yield production of graphene by liquid-phase exfoliation of graphite,* Nat. Nanotechnol. **3**, 563 (2008).

[9] W. A. de Heer, C. Berger, X. S. Wu, P. N. First, E. H. Conrad, X. B. Li, T. B. Li, M. Sprinkle, J. Hass, M. L. Sadowski, M. Potemski, and G. Martinez, *Epitaxial graphene,* Solid State Commun **143**, 92 (2007).

[10] X. S. Li, W. W. Cai, J. H. An, S. Kim, J. Nah, D. X. Yang, R. Piner, A. Velamakanni, I. Jung, E. Tutuc, S. K. Banerjee, L. Colombo, and R. S. Ruoff, *Large-Area Synthesis of High-Quality and Uniform Graphene Films on Copper Foils,* Science **324**, 1312 (2009).

[11] L. L. Liu, M. Q. Qing, Y. B. Wang, and S. M. Chen, *Defects in Graphene: Generation, Healing, and Their Effects on the Properties of Graphene: A Review,* J Mater Sci Technol **31**, 599 (2015).

[12] S. Navalon, A. Dhakshinamoorthy, M. Alvaro, M. Antonietti, and H. Garcia, *Active sites on graphene-based materials as metal-free catalysts,* Chem Soc Rev **46**, 4501 (2017).

[13] P. Solis-Fernandez, M. Bissett, and H. Ago, *Synthesis, structure and applications of graphene-based 2D heterostructures,* Chem Soc Rev **46**, 4572 (2017).

[14] M. Pumera and Z. Sofer, *Towards stoichiometric analogues of graphene: graphane, fluorographene, graphol, graphene acid and others,* Chem Soc Rev **46**, 4450 (2017).

[15] L. G. De Arco, Y. Zhang, C. W. Schlenker, K. Ryu, M. E. Thompson, and C. W. Zhou, *Continuous, Highly Flexible, and Transparent Graphene Films by Chemical Vapor Deposition for Organic Photovoltaics,* Acs Nano **4**, 2865 (2010).

[16] D. C. Wei, Y. Q. Liu, Y. Wang, H. L. Zhang, L. P. Huang, and G. Yu, *Synthesis of N-Doped Graphene by Chemical Vapor Deposition and Its Electrical Properties,* Nano Lett. **9**, 1752 (2009).

[17] A. L. M. Reddy, A. Srivastava, S. R. Gowda, H. Gullapalli, M. Dubey, and P. M. Ajayan, *Synthesis Of Nitrogen-Doped Graphene Films For Lithium Battery Application,* Acs Nano **4**, 6337 (2010).

[18] G. Reina, J. M. Gonzalez-Dominguez, A. Criado, E. Vazquez, A. Bianco, and M. Prato, *Promises, facts and challenges for graphene in biomedical applications,* Chem Soc Rev **46**, 4400 (2017).

[19] J. Li, S. Majety, R. Dahal, W. P. Zhao, J. Y. Lin, and H. X. Jiang, *Dielectric strength, optical absorption, and deep ultraviolet detectors of hexagonal boron nitride epilayers,* Appl. Phys. Lett. **101** (2012).
[20] M. P. Levendorf, C. J. Kim, L. Brown, P. Y. Huang, R. W. Havener, D. A. Muller, and J. Park, *Graphene and boron nitride lateral heterostructures for atomically thin circuitry,* Nature **488**, 627 (2012).
[21] P. W. Bridgman, *Two new modifications of phosphorus.,* J. Am. Chem. Soc. **36**, 1344 (1914).
[22] X. Li, J. P. Sun, P. Shahi, M. Gao, A. H. MacDonald, Y. Uwatoko, T. Xiang, J. B. Goodenough, J. G. Cheng, and J. S. Zhou, *Pressure-induced phase transitions and superconductivity in a black phosphorus single crystal,* Proc. Natl. Acad. Sci. U.S.A. **115**, 9935 (2018).
[23] L. K. Li, Y. J. Yu, G. J. Ye, Q. Q. Ge, X. D. Ou, H. Wu, D. L. Feng, X. H. Chen, and Y. B. Zhang, *Black phosphorus field-effect transistors,* Nat. Nanotechnol. **9**, 372 (2014).
[24] Y. X. Deng, Z. Luo, N. J. Conrad, H. Liu, Y. J. Gong, S. Najmaei, P. M. Ajayan, J. Lou, X. F. Xu, and P. D. Ye, *Black Phosphorus-Monolayer MoS2 van der Waals Heterojunction p-n Diode,* Acs Nano **8**, 8292 (2014).
[25] X. Zhang, X. F. Qiao, W. Shi, J. B. Wu, D. S. Jiang, and P. H. Tan, *Phonon and Raman scattering of two-dimensional transition metal dichalcogenides from monolayer, multilayer to bulk material,* Chem Soc Rev **44**, 2757 (2015).
[26] D. L. Greenaway and R. Nitsche, *Preparation and Optical Properties of Group 4-62 Chalcogenides Having Cdi2 Structure,* J Phys Chem Solids **26**, 1445 (1965).
[27] F. J. Disalvo, D. E. Moncton, and J. V. Waszczak, *Electronic Properties and Superlattice Formation in Semimetal Tise2,* Phys. Rev. B **14**, 4321 (1976).
[28] G. Li, W. Z. Hu, D. Qian, D. Hsieh, M. Z. Hasan, E. Morosan, R. J. Cava, and N. L. Wang, *Semimetal-to-semimetal charge density wave transition in 1T-TiSe2,* Phys. Rev. Lett. **99** (2007).
[29] J. C. E. Rasch, T. Stemmler, B. Muller, L. Dudy, and R. Manzke, *1T-TiSe(2): Semimetal or Semiconductor?,* Phys. Rev. Lett. **101** (2008).
[30] P. Peierls, *Quantum Theory of Solids* 1955).
[31] C. Monney, C. Battaglia, H. Cercellier, P. Aebi, and H. Beck, *Exciton Condensation Driving the Periodic Lattice Distortion of 1T-TiSe2,* Phys. Rev. Lett. **106** (2011).
[32] Y. Zhao, J. Qiao, Z. Yu, P. Yu, K. Xu, S. P. Lau, W. Zhou, Z. Liu, X. Wang, and W. Ji, *High‐Electron‐Mobility and Air‐Stable 2D Layered $PtSe_2$ FETs,* Adv. Mater. **29**, 1604230 (2017).
[33] M. Sajjad, E. Montes, N. Singh, and U. Schwingenschlögl, *Superior Gas Sensing Properties of Monolayer $PtSe_2$,* Adv. Mater. Interfaces **4**, 1600911 (2017).
[34] Y. Wang, L. Li, W. Yao, S. Song, J. Sun, J. Pan, X. Ren, C. Li, E. Okunishi, and Y.-Q. Wang, *Monolayer $PtSe_2$, a New Semiconducting Transition-Metal-Dichalcogenide, Epitaxially Grown by Direct Selenization of Pt,* Nano Lett. **15**, 4013 (2015).
[35] K. F. Mak, C. Lee, J. Hone, J. Shan, and T. F. Heinz, *Atomically Thin MoS2: A New Direct-Gap Semiconductor,* Phys. Rev. Lett. **105** (2010).
[36] B. Jayasena and S. Subbiah, *A novel mechanical cleavage method for synthesizing few-layer graphenes,* Nanoscale Res Lett **6** (2011).
[37] P. Joensen, R. F. Frindt, and S. R. Morrison, *Single-Layer Mos2,* Mater Res Bull **21**, 457 (1986).
[38] M. A. Py and R. R. Haering, *Structural Destabilization Induced by Lithium Intercalation in Mos2 and Related-Compounds,* Can J Phys **61**, 76 (1983).
[39] J. N. Coleman, M. Lotya, A. O'Neill, S. D. Bergin, P. J. King, U. Khan, K. Young, A. Gaucher, S. De, R. J. Smith, I. V. Shvets, S. K. Arora, G. Stanton, H. Y. Kim, K. Lee, G. T. Kim, G. S. Duesberg, T. Hallam, J. J. Boland, J. J. Wang, J. F. Donegan, J. C. Grunlan, G. Moriarty, A. Shmeliov, R. J. Nicholls, J. M. Perkins, E. M. Grieveson, K. Theuwissen, D. W. McComb, P. D. Nellist, and V. Nicolosi, *Two-Dimensional Nanosheets Produced by Liquid Exfoliation of Layered Materials,* Science **331**, 568 (2011).

[40] C. Virojanadara, M. Syvajarvi, R. Yakimova, L. I. Johansson, A. A. Zakharov, and T. Balasubramanian, *Homogeneous large-area graphene layer growth on 6H-SiC(0001),* Phys. Rev. B **78** (2008).
[41] Y. C. Lin, W. J. Zhang, J. K. Huang, K. K. Liu, Y. H. Lee, C. T. Liang, C. W. Chu, and L. J. Li, *Wafer-scale MoS2 thin layers prepared by MoO3 sulfurization,* Nanoscale **4**, 6637 (2012).
[42] P. R. Somani, S. P. Somani, and M. Umeno, *Planer nano-graphenes from camphor by CVD,* Chem Phys Lett **430**, 56 (2006).
[43] L. B. Gao, W. C. Ren, H. L. Xu, L. Jin, Z. X. Wang, T. Ma, L. P. Ma, Z. Y. Zhang, Q. Fu, L. M. Peng, X. H. Bao, and H. M. Cheng, *Repeated growth and bubbling transfer of graphene with millimetre-size single-crystal grains using platinum,* Nat. Commun. **3** (2012).
[44] W. Liu, H. Li, C. Xu, Y. Khatami, and K. Banerjee, *Synthesis of high-quality monolayer and bilayer graphene on copper using chemical vapor deposition,* Carbon **49**, 4122 (2011).
[45] D. C. Geng, B. Wu, Y. L. Guo, L. P. Huang, Y. Z. Xue, J. Y. Chen, G. Yu, L. Jiang, W. P. Hu, and Y. Q. Liu, *Uniform hexagonal graphene flakes and films grown on liquid copper surface,* Proc. Natl. Acad. Sci. U.S.A. **109**, 7992 (2012).
[46] Y. H. Lee, X. Q. Zhang, W. J. Zhang, M. T. Chang, C. T. Lin, K. D. Chang, Y. C. Yu, J. T. W. Wang, C. S. Chang, L. J. Li, and T. W. Lin, *Synthesis of Large-Area MoS2 Atomic Layers with Chemical Vapor Deposition,* Adv. Mater. **24**, 2320 (2012).
[47] S. J. Yun, S. H. Chae, H. Kim, J. C. Park, J. H. Park, G. H. Han, J. S. Lee, S. M. Kim, H. M. Oh, J. Seok, M. S. Jeong, K. K. Kim, and Y. H. Lee, *Synthesis of Centimeter-Scale Monolayer Tungsten Disulfide Film on Gold Foils,* Acs Nano **9**, 5510 (2015).
[48] J. Y. Chen, X. X. Zhao, S. J. R. Tan, H. Xu, B. Wu, B. Liu, D. Y. Fu, W. Fu, D. C. Geng, Y. P. Liu, W. Liu, W. Tang, L. J. Li, W. Zhou, T. C. Sum, and K. P. Loh, *Chemical Vapor Deposition of Large-Size Monolayer MoSe2 Crystals on Molten Glass,* J. Am. Chem. Soc. **139**, 1073 (2017).
[49] Y. Gao, Y. L. Hong, L. C. Yin, Z. T. Wu, Z. Q. Yang, M. L. Chen, Z. B. Liu, T. Ma, D. M. Sun, Z. H. Ni, X. L. Ma, H. M. Cheng, and W. C. Ren, *Ultrafast Growth of High-Quality Monolayer WSe2 on Au,* Adv. Mater. **29** (2017).
[50] K. K. Kam and B. A. Parkinson, *Detailed Photocurrent Spectroscopy of the Semiconducting Group-Vi Transition-Metal Dichalcogenides,* J Phys Chem-Us **86**, 463 (1982).
[51] W. Jaegermann and D. Schmeisser, *Reactivity of Layer Type Transition-Metal Chalcogenides Towards Oxidation,* Surf. Sci. **165**, 143 (1986).
[52] H. Wang, X. W. Huang, J. H. Lin, J. Cui, Y. Chen, C. Zhu, F. C. Liu, Q. S. Zeng, J. D. Zhou, P. Yu, X. W. Wang, H. Y. He, S. H. Tsang, W. B. Gao, K. Suenaga, F. C. Ma, C. L. Yang, L. Lu, T. Yu, E. H. T. Teo, G. T. Liu, and Z. Liu, *High-quality monolayer superconductor NbSe2 grown by chemical vapour deposition,* Nat. Commun. **8** (2017).
[53] H. Wang, Y. Chen, M. Duchamp, Q. S. Zeng, X. W. Wang, S. H. Tsang, H. L. Li, L. Jing, T. Yu, E. H. T. Teo, and Z. Liu, *Large-Area Atomic Layers of the Charge-Density-Wave Conductor TiSe2,* Adv. Mater. **30** (2018).
[54] D. Akinwande, C. J. Brennan, J. S. Bunch, P. Egberts, J. R. Felts, H. J. Gao, R. Huang, J. S. Kim, T. Li, Y. Li, K. M. Liechti, N. S. Lu, H. S. Park, E. J. Reed, P. Wang, B. I. Yakobson, T. Zhang, Y. W. Zhang, Y. Zhou, and Y. Zhu, *A review on mechanics and mechanical properties of 2D materials-Graphene and beyond,* Extreme Mech Lett **13**, 42 (2017).
[55] J. C. Meyer, C. Kisielowski, R. Erni, M. D. Rossell, M. F. Crommie, and A. Zettl, *Direct Imaging of Lattice Atoms and Topological Defects in Graphene Membranes,* Nano Lett. **8**, 3582 (2008).
[56] A. A. El-Barbary, R. H. Telling, C. P. Ewels, M. I. Heggie, and P. R. Briddon, *Structure and energetics of the vacancy in graphite,* Phys. Rev. B **68** (2003).
[57] Y. Kim, J. Ihm, E. Yoon, and G. D. Lee, *Dynamics and stability of divacancy defects in graphene,* Phys. Rev. B **84** (2011).

[58] W. Zhou, X. L. Zou, S. Najmaei, Z. Liu, Y. M. Shi, J. Kong, J. Lou, P. M. Ajayan, B. I. Yakobson, and J. C. Idrobo, *Intrinsic Structural Defects in Monolayer Molybdenum Disulfide,* Nano Lett. **13**, 2615 (2013).
[59] L. Nguyen, H. P. Komsa, E. Khestanova, R. J. Kashtiban, J. J. P. Peters, S. Lawlor, A. M. Sanchez, J. Sloan, R. V. Gorbachev, I. V. Grigorieva, A. V. Krasheninnikov, and S. J. Haigh, *Atomic Defects and Doping of Monolayer NbSe2,* Acs Nano **11**, 2894 (2017).
[60] S. Zhang, C. G. Wang, M. Y. Li, D. Huang, L. J. Li, W. Ji, and S. W. Wu, *Defect Structure of Localized Excitons in a WSe_2 Monolayer,* Phys. Rev. Lett. **119**, 046101 (2017).
[61] G. H. Ryu, J. Chen, Y. Wen, S. Zhou, R. J. Chang, and J. H. Warner, *Atomic structural catalogue of defects and vertical stacking in 2H/3R mixed polytype multilayer WS2 pyramids,* Nanoscale **11**, 10859 (2019).
[62] H. P. Komsa, S. Kurasch, O. Lehtinen, U. Kaiser, and A. V. Krasheninnikov, *From point to extended defects in two-dimensional MoS2: Evolution of atomic structure under electron irradiation,* Phys. Rev. B **88** (2013).
[63] G. L. Ye, Y. J. Gong, J. H. Lin, B. Li, Y. M. He, S. T. Pantelides, W. Zhou, R. Vajtai, and P. M. Ajayan, *Defects Engineered Monolayer MoS2 for Improved Hydrogen Evolution Reaction,* Nano Lett. **16**, 1097 (2016).
[64] S. Hosoki, S. Hosaka, and T. Hasegawa, *Surface Modification of MoS_2 Using an STM,* Appl. Surf. Sci. **60-1**, 643 (1992).
[65] Y. Chen, S. X. Huang, X. Ji, K. Adepalli, K. D. Yin, X. Ling, X. W. Wang, J. M. Xue, M. Dresselhaus, J. Kong, and B. Yildiz, *Tuning Electronic Structure of Single Layer MoS2 through Defect and Interface Engineering,* Acs Nano **12**, 2569 (2018).
[66] Y. F. Chen, J. Y. Xi, D. O. Dumcenco, Z. Liu, K. Suenaga, D. Wang, Z. G. Shuai, Y. S. Huang, and L. M. Xie, *Tunable Band Gap Photoluminescence from Atomically Thin Transition-Metal Dichalcogenide Alloys,* Acs Nano **7**, 4610 (2013).
[67] Y. J. Gong, Z. Liu, A. R. Lupini, G. Shi, J. H. Lin, S. Najmaei, Z. Lin, A. L. Elias, A. Berkdemir, G. You, H. Terrones, M. Terrones, R. Vajtai, S. T. Pantelides, S. J. Pennycook, J. Lou, W. Zhou, and P. M. Ajayan, *Band Gap Engineering and Layer-by-Layer Mapping of Selenium-Doped Molybdenum Disulfide,* Nano Lett. **14**, 442 (2014).
[68] J. Suh, T. E. Park, D. Y. Lin, D. Y. Fu, J. Park, H. J. Jung, Y. B. Chen, C. Ko, C. Jang, Y. H. Sun, R. Sinclair, J. Chang, S. Tongay, and J. Q. Wu, *Doping against the Native Propensity of MoS2: Degenerate Hole Doping by Cation Substitution,* Nano Lett. **14**, 6976 (2014).
[69] A. Lherbier, X. Blase, Y. M. Niquet, F. Triozon, and S. Roche, *Charge transport in chemically doped 2D graphene,* Phys. Rev. Lett. **101** (2008).
[70] D. O. Dumcenco, H. Kobayashi, Z. Liu, Y.-S. Huang, and K. Suenaga, *Visualization and quantification of transition metal atomic mixing in $Mo_{1-x}W_xS_2$ single layers,* Nat. Commun. **4**, 1351 (2013).
[71] H. Li, X. Duan, X. Wu, X. Zhuang, H. Zhou, Q. Zhang, X. Zhu, W. Hu, P. Ren, and P. J. J. o. t. A. C. S. Guo, *Growth of Alloy MoS2 x Se2 (1–x) Nanosheets with Fully Tunable Chemical Compositions and Optical Properties,* **136**, 3756 (2014).
[72] K. Dolui, I. Rungger, C. Das Pemmaraju, and S. Sanvito, *Possible doping strategies for MoS2 monolayers: An ab initio study,* Phys. Rev. B **88** (2013).
[73] K. Sugawara, K. Kanetani, T. Sato, and T. Takahashi, *Fabrication of Li-intercalated bilayer graphene,* Aip Adv **1** (2011).
[74] M. Kuhne, F. Paolucci, J. Popovic, P. M. Ostrovsky, J. Maier, and J. H. Smet, *Ultrafast lithium diffusion in bilayer graphene,* Nat. Nanotechnol. **12**, 895 (2017).
[75] S. Ichinokura, K. Sugawara, A. Takayama, T. Takahashi, and S. Hasegawa, *Superconducting Calcium-Intercalated Bilayer Graphene,* Acs Nano **10**, 2761 (2016).

[76] M. A. Lukowski, A. S. Daniel, F. Meng, A. Forticaux, L. S. Li, and S. Jin, *Enhanced Hydrogen Evolution Catalysis from Chemically Exfoliated Metallic MoS2 Nanosheets,* J. Am. Chem. Soc. **135**, 10274 (2013).
[77] P. O. Lehtinen, A. S. Foster, A. Ayuela, A. Krasheninnikov, K. Nordlund, and R. M. Nieminen, *Magnetic properties and diffusion of adatoms on a graphene sheet,* Phys. Rev. Lett. **91** (2003).
[78] K. T. Chan, J. B. Neaton, and M. L. Cohen, *First-principles study of metal adatom adsorption on graphene,* Phys. Rev. B **77** (2008).
[79] O. Cretu, A. V. Krasheninnikov, J. A. Rodriguez-Manzo, L. T. Sun, R. M. Nieminen, and F. Banhart, *Migration and Localization of Metal Atoms on Strained Graphene,* Phys. Rev. Lett. **105** (2010).
[80] H. S. Li, S. S. Wang, H. Sawada, G. G. D. Han, T. Samuels, C. S. Allen, A. I. Kirkland, J. C. Grossman, and J. H. Warner, *Atomic Structure and Dynamics of Single Platinum Atom Interactions with Monolayer MoS2,* Acs Nano **11**, 3392 (2017).
[81] G. L. Liu, A. W. Robertson, M. M. J. Li, W. C. H. Kuo, M. T. Darby, M. H. Muhieddine, Y. C. Lin, K. Suenaga, M. Stamatakis, J. H. Warner, and S. C. E. Tsang, *MoS2 monolayer catalyst doped with isolated Co atoms for the hydrodeoxygenation reaction,* Nat. Chem. **9**, 810 (2017).
[82] P. Y. Huang, C. S. Ruiz-Vargas, A. M. van der Zande, W. S. Whitney, M. P. Levendorf, J. W. Kevek, S. Garg, J. S. Alden, C. J. Hustedt, Y. Zhu, J. Park, P. L. McEuen, and D. A. Muller, *Grains and grain boundaries in single-layer graphene atomic patchwork quilts,* Nature **469**, 389 (2011).
[83] O. V. Yazyev and S. G. Louie, *Topological defects in graphene: Dislocations and grain boundaries,* Phys. Rev. B **81**, 195420 (2010).
[84] A. M. van der Zande, P. Y. Huang, D. A. Chenet, T. C. Berkelbach, Y. M. You, G. H. Lee, T. F. Heinz, D. R. Reichman, D. A. Muller, and J. C. Hone, *Grains and grain boundaries in highly crystalline monolayer molybdenum disulphide,* Nat. Mater. **12**, 554 (2013).
[85] Y. J. Ma, S. Kolekar, H. C. Diaz, J. Aprojanz, I. Miccoli, C. Tegenkamp, and M. Batzill, *Metallic Twin Grain Boundaries Embedded in MoSe2 Monolayers Grown by Molecular Beam Epitaxy,* Acs Nano **11**, 5130 (2017).
[86] Y. L. Huang, Y. F. Chen, W. J. Zhang, S. Y. Quek, C. H. Chen, L. J. Li, W. T. Hsu, W. H. Chang, Y. J. Zheng, W. Chen, and A. T. S. Wee, *Bandgap tunability at single-layer molybdenum disulphide grain boundaries,* Nat. Commun. **6** (2015).
[87] B. Radisavljevic, A. Radenovic, J. Brivio, V. Giacometti, and A. Kis, *Single-layer MoS2 transistors,* Nat. Nanotechnol. **6**, 147 (2011).
[88] H. Fang, S. Chuang, T. C. Chang, K. Takei, T. Takahashi, and A. Javey, *High-Performance Single Layered WSe2 p-FETs with Chemically Doped Contacts,* Nano Lett. **12**, 3788 (2012).
[89] Y. D. Zhao, J. S. Qiao, Z. H. Yu, P. Yu, K. Xu, S. P. Lau, W. Zhou, Z. Liu, X. R. Wang, W. Ji, and Y. Chai, *High-Electron- Mobility and Air-Stable 2D Layered PtSe2 FETs,* Adv. Mater. **29** (2017).
[90] F. N. Xia, T. Mueller, Y. M. Lin, A. Valdes-Garcia, and P. Avouris, *Ultrafast graphene photodetector,* Nat. Nanotechnol. **4**, 839 (2009).
[91] T. Mueller, F. N. A. Xia, and P. Avouris, *Graphene photodetectors for high-speed optical communications,* Nat Photonics **4**, 297 (2010).
[92] Z. Y. Yin, H. Li, H. Li, L. Jiang, Y. M. Shi, Y. H. Sun, G. Lu, Q. Zhang, X. D. Chen, and H. Zhang, *Single-Layer MoS2 Phototransistors,* Acs Nano **6**, 74 (2012).
[93] O. Lopez-Sanchez, D. Lembke, M. Kayci, A. Radenovic, and A. Kis, *Ultrasensitive photodetectors based on monolayer MoS2,* Nat. Nanotechnol. **8**, 497 (2013).
[94] W. J. Zhang, J. K. Huang, C. H. Chen, Y. H. Chang, Y. J. Cheng, and L. J. Li, *High-Gain Phototransistors Based on a CVD MoS2 Monolayer,* Adv. Mater. **25**, 3456 (2013).
[95] T. Y. Su, H. Medina, Y. Z. Chen, S. W. Wang, S. S. Lee, Y. C. Shih, C. W. Chen, H. C. Kuo, F. C. Chuang, and Y. L. Chueh, *Phase-Engineered PtSe2-Layered Films by a Plasma-Assisted Selenization*

Process toward All PtSe2-Based Field Effect Transistor to Highly Sensitive, Flexible, and Wide-Spectrum Photoresponse Photodetectors, Small **14** (2018).
[96] D. Wu, Y. E. Wang, L. H. Zeng, C. Jia, E. P. Wu, T. T. Xu, Z. F. Shi, Y. T. Tian, X. J. Li, and Y. H. Tsang, *Design of 2D Layered PtSe2 Heterojunction for the High-Performance, Room-Temperature, Broadband, Infrared Photodetector,* Acs Photonics **5**, 3820 (2018).
[97] Z. X. Zhang, L. H. Zeng, X. W. Tong, Y. Gao, C. Xie, Y. H. Tsang, L. B. Luo, and Y. C. Wu, *Ultrafast, Self-Driven, and Air-Stable Photodetectors Based on Multilayer PtSe2/Perovskite Heterojunctions,* J Phys Chem Lett **9**, 1185 (2018).
[98] L. H. Zeng, S. H. Lin, Z. H. Lou, H. Y. Yuan, H. Long, Y. Y. Li, W. Lu, S. P. Lau, D. Wu, and Y. H. Tsang, *Ultrafast and sensitive photodetector based on a PtSe2/silicon nanowire array heterojunction with a multiband spectral response from 200 to 1550 nm,* Npg Asia Mater **10**, 352 (2018).
[99] L. H. Zeng, S. H. Lin, Z. J. Li, Z. X. Zhang, T. F. Zhang, C. Xie, C. H. Mak, Y. Chai, S. P. Lau, L. B. Luo, and Y. H. Tsang, *Fast, Self-Driven, Air-Stable, and Broadband Photodetector Based on Vertically Aligned PtSe2/GaAs Heterojunction,* Adv Funct Mater **28** (2018).
[100] Z. F. Liu, Q. Liu, Y. Huang, Y. F. Ma, S. G. Yin, X. Y. Zhang, W. Sun, and Y. S. Chen, *Organic Photovoltaic Devices Based on a Novel Acceptor Material: Graphene,* Adv. Mater. **20**, 3924 (2008).
[101] E. Fortin and W. M. Sears, *Photo-Voltaic Effect and Optical-Absorption in Mos2,* J Phys Chem Solids **43**, 881 (1982).
[102] M. Bernardi, M. Palummo, and J. C. Grossman, *Extraordinary Sunlight Absorption and One Nanometer Thick Photovoltaics Using Two-Dimensional Monolayer Materials,* Nano Lett. **13**, 3664 (2013).
[103] M. L. Tsai, S. H. Su, J. K. Chang, D. S. Tsai, C. H. Chen, C. I. Wu, L. J. Li, L. J. Chen, and J. H. He, *Monolayer MoS2 Heterojunction Solar Cells,* Acs Nano **8**, 8317 (2014).
[104] S. S. Lin, X. Q. Li, P. Wang, Z. J. Xu, S. J. Zhang, H. K. Zhong, Z. Q. Wu, W. L. Xu, and H. S. Chen, *Interface designed MoS2/GaAs heterostructure solar cell with sandwich stacked hexagonal boron nitride,* Sci. Rep. **5** (2015).
[105] F. Schedin, A. K. Geim, S. V. Morozov, E. W. Hill, P. Blake, M. I. Katsnelson, and K. S. Novoselov, *Detection of individual gas molecules adsorbed on graphene,* Nat. Mater. **6**, 652 (2007).
[106] F. Yavari and N. Koratkar, *Graphene-Based Chemical Sensors,* J Phys Chem Lett **3**, 1746 (2012).
[107] S. Mao, S. M. Cui, G. H. Lu, K. H. Yu, Z. H. Wen, and J. H. Chen, *Tuning gas-sensing properties of reduced graphene oxide using tin oxide nanocrystals,* J Mater Chem **22**, 11009 (2012).
[108] S. Liu, B. Yu, H. Zhang, T. Fei, and T. Zhang, *Enhancing NO2 gas sensing performances at room temperature based on reduced graphene oxide-ZnO nanoparticles hybrids,* Sensor Actuat B-Chem **202**, 272 (2014).
[109] B. Cho, A. R. Kim, Y. Park, J. Yoon, Y. J. Lee, S. Lee, T. J. Yoo, C. G. Kang, B. H. Lee, H. C. Ko, D. H. Kim, and M. G. Hahm, *Bifunctional Sensing Characteristics of Chemical Vapor Deposition Synthesized Atomic-Layered MoS2,* Acs Appl Mater Inter **7**, 2952 (2015).
[110] D. J. Late, T. Doneux, and M. Bougouma, *Single-layer MoSe2 based NH3 gas sensor,* Appl. Phys. Lett. **105** (2014).
[111] C. Su, X. D. Bu, L. H. Xu, J. L. Liu, and C. Zhang, *A novel LiFePO4/graphene/carbon composite as a performance-improved cathode material for lithium-ion batteries,* Electrochim Acta **64**, 190 (2012).
[112] X. F. Zhou, F. Wang, Y. M. Zhu, and Z. P. Liu, *Graphene modified LiFePO4 cathode materials for high power lithium ion batteries,* J Mater Chem **21**, 3353 (2011).
[113] Y. P. Liu, H. T. Wang, L. Cheng, N. Han, F. P. Zhao, P. R. Li, C. H. Jin, and Y. G. Li, *TiS2 nanoplates: A high-rate and stable electrode material for sodium ion batteries,* Nano Energy **20**, 168 (2016).
[114] D. Zhang, G. Q. Zhao, P. Li, Y. Zhang, W. B. Qiu, J. Shu, Y. Z. Jiang, S. X. Dou, and W. P. Sun, *Readily Exfoliated TiSe2 Nanosheets for High-Performance Sodium Storage,* Chem-Eur J **24**, 1193 (2018).
[115] T. R. Juran and M. Smeu, *TiSe2 cathode for beyond Li-ion batteries,* J Power Sources **436** (2019).

[116] P. C. Li, C. M. Chen, Z. Huang, Y. Cai, and M. Zhang, *The transformation of anatase TiO2 to TiSe2 to form TiO2-TiSe2 composites for Li+/Na+ storage with improved capacities,* Crystengcomm **21**, 2517 (2019).
[117] U. Staufer, R. Wiesendanger, L. Eng, L. Rosenthaler, H. R. Hidber, H. J. Guntherodt, and N. Garcia, *Nanometer Scale Structure Fabrication with the Scanning Tunneling Microscope,* Appl. Phys. Lett. **51**, 244 (1987).
[118] M. F. Crommie, C. P. Lutz, and D. M. Eigler, *Confinement of Electrons to Quantum Corrals on a Metal-Surface,* Science **262**, 218 (1993).
[119] L. Tapaszto, G. Dobrik, P. Lambin, and L. P. Biro, *Tailoring the atomic structure of graphene nanoribbons by scanning tunnelling microscope lithography,* Nat. Nanotechnol. **3**, 397 (2008).
[120] S. Akari, R. Moller, and K. Dransfeld, *Triangular Structures on Tungsten Diselenide Induced and Observed by Scanning Tunneling Microscopy,* Applied Physics Letters **59**, 243 (1991).
[121] J. Boneberg, M. Lohrmann, M. Bohmisch, F. Burmeister, M. LuxSteiner, and P. Leiderer, *Electrical field induced growth of triangular nanometer structures on WSe2,* Zeitschrift Fur Physik B-Condensed Matter **99**, 567 (1996).
[122] W. Yamaguchi, O. Shiino, H. Sugawara, T. Hasegawa, and K. Kitazawa, *Surface etching of 1T-TaS2 with the UHV-STM,* Applied Surface Science **119**, 67 (1997).
[123] J. Y. Wang, H. S. Zheng, G. C. Xu, L. F. Sun, D. K. Hu, Z. X. Lu, L. N. Liu, J. Y. Zheng, C. G. Tao, and L. Y. Jiao, *Controlled Synthesis of Two-Dimensional 1T-$TiSe_2$ with Charge Density Wave Transition by Chemical Vapor Transport,* J. Am. Chem. Soc. **138**, 16216 (2016).
[124] M. D. Johannes, I. I. Mazin, and C. A. Howells, *Fermi-surface nesting and the origin of the charge-density wave in NbSe2,* Phys. Rev. B **73** (2006).
[125] P. Chen, Y. H. Chan, X. Y. Fang, Y. Zhang, M. Y. Chou, S. K. Mo, Z. Hussain, A. V. Fedorov, and T. C. Chiang, *Charge density wave transition in single-layer titanium diselenide,* Nat. Commun. **6** (2015).
[126] E. Morosan, H. W. Zandbergen, B. S. Dennis, J. W. G. Bos, Y. Onose, T. Klimczuk, A. P. Ramirez, N. P. Ong, and R. J. Cava, *Superconductivity in CuxTiSe2,* Nat. Phys. **2**, 544 (2006).
[127] A. F. Kusmartseva, B. Sipos, H. Berger, L. Forro, and E. Tutis, *Pressure Induced Superconductivity in Pristine 1T-TiSe2,* Phys. Rev. Lett. **103** (2009).
[128] S. Kolekar, M. Bonilla, Y. J. Ma, H. C. Diaz, and M. Batzill, *Layer- and substrate-dependent charge density wave criticality in 1T-TiSe2,* 2D Mater. **5** (2018).
[129] Y. S. e. al., *Incommensurate Chiral CDW in 1T-VSe_2,* https://arxiv.org/pdf/1812.01368.pdf (2018).
[130] G. Duvjir, B. K. Choi, I. Jang, S. Ulstrup, S. Kang, T. T. Ly, S. Kim, Y. H. Choi, C. Jozwiak, A. Bostwick, E. Rotenberg, J. G. Park, R. Sankar, K. S. Kim, J. Kim, and Y. J. Chang, *Emergence of a Metal-Insulator Transition and High-Temperature Charge-Density Waves in VSe2 at the Monolayer Limit,* Nano Lett. **18**, 5432 (2018).
[131] H. Ryu, Y. Chen, H. Kim, H. Z. Tsai, S. J. Tang, J. Jiang, F. Liou, S. Kahn, C. H. Jia, A. A. Omrani, J. H. Shim, Z. Hussain, Z. X. Shen, K. Kim, B. I. Min, C. Hwang, M. F. Crommie, and S. K. Mo, *Persistent Charge-Density-Wave Order in Single-Layer TaSe2,* Nano Lett. **18**, 689 (2018).
[132] D. C. Freitas, P. Rodiere, M. R. Osorio, E. Navarro-Moratalla, N. M. Nemes, V. G. Tissen, L. Cario, E. Coronado, M. Garcia-Hernandez, S. Vieira, M. Nunez-Regueiro, and H. Suderow, *Strong enhancement of superconductivity at high pressures within the charge-density-wave states of 2H-TaS2 and 2H-TaSe2,* Phys. Rev. B **93** (2016).
[133] C. B. Scruby, P. M. Williams, and G. S. Parry, *Role of Charge-Density Waves in Structural Transformations of 1t Tas2,* Philos Mag **31**, 255 (1975).
[134] C. Zhu, Y. Chen, F. C. Liu, S. J. Zheng, X. B. Li, A. Chaturvedi, J. D. Zhou, Q. D. Fu, Y. M. He, Q. S. Zeng, H. J. Fan, H. Zhang, W. J. Liu, T. Yu, and Z. Liu, *Light-Tunable 1T-TaS2 Charge-Density-Wave Oscillators,* Acs Nano **12**, 11203 (2018).

[135] Y. Fujisawa, T. Iwasaki, D. Fujii, S. Ohta, J. Iwashita, T. Fujita, M. Nakata, K. Kishimoto, S. Demura, and H. Sakata, *Superposition of root 13 x root 13 and 3 x 3 supermodulations in TaS2 probed by scanning tunneling microscopy,* J Phys Conf Ser **969** (2018).
[136] M. M. Ugeda, A. J. Bradley, Y. Zhang, S. Onishi, Y. Chen, W. Ruan, C. Ojeda-Aristizabal, H. Ryu, M. T. Edmonds, H. Z. Tsai, A. Riss, S. K. Mo, D. H. Lee, A. Zettl, Z. Hussain, Z. X. Shen, and M. F. Crommie, *Characterization of collective ground states in single-layer NbSe2,* Nat. Phys. **12**, 92 (2016).
[137] X. X. Xi, L. Zhao, Z. F. Wang, H. Berger, L. Forro, J. Shan, and K. F. Mak, *Strongly enhanced charge-density-wave order in monolayer NbSe2,* Nat. Nanotechnol. **10**, 765 (2015).
[138] A. K. Geim and I. V. Grigorieva, *Van der Waals heterostructures,* Nature **499**, 419 (2013).
[139] L. Britnell, R. M. Ribeiro, A. Eckmann, R. Jalil, B. D. Belle, A. Mishchenko, Y. J. Kim, R. V. Gorbachev, T. Georgiou, S. V. Morozov, A. N. Grigorenko, A. K. Geim, C. Casiraghi, A. H. Castro Neto, and K. S. Novoselov, *Strong Light-Matter Interactions in Heterostructures of Atomically Thin Films,* Science **340**, 1311 (2013).
[140] Y. B. Wu, W. Yang, T. B. Wang, X. H. Deng, and J. T. Liu, *Broadband perfect light trapping in the thinnest monolayer graphene-MoS2 photovoltaic cell: the new application of spectrum-splitting structure,* Sci. Rep. **6** (2016).
[141] J. P. Peng, J. Q. Guan, H. M. Zhang, C. L. Song, L. L. Wang, K. He, Q. K. Xue, and X. C. Ma, *Molecular beam epitaxy growth and scanning tunneling microscopy study of TiSe2 ultrathin films,* Phys. Rev. B **91** (2015).
[142] K. Sugawara, Y. Nakata, R. Shimizu, P. Han, T. Hitosugi, T. Sato, and T. Takahashi, *Unconventional Charge-Density-Wave Transition in Monolayer 1T-TiSe2,* Acs Nano **10**, 1341 (2016).
[143] L. J. Li, E. C. T. O'Farrell, K. P. Loh, G. Eda, B. Ozyilmaz, and A. H. C. Neto, *Controlling many-body states by the electric-field effect in a two-dimensional material,* Nature **529**, 185 (2016).
[144] X. X. Xi, Z. F. Wang, W. W. Zhao, J. H. Park, K. T. Law, H. Berger, L. Forro, J. Shan, and K. F. Mak, *Ising pairing in superconducting NbSe2 atomic layers,* Nat. Phys. **12**, 139 (2016).
[145] Y. J. Yu, F. Y. Yang, X. F. Lu, Y. J. Yan, Y. H. Cho, L. G. Ma, X. H. Niu, S. Kim, Y. W. Son, D. L. Feng, S. Y. Li, S. W. Cheong, X. H. Chen, and Y. B. Zhang, *Gate-tunable phase transitions in thin flakes of 1T-TaS2,* Nat. Nanotechnol. **10**, 270 (2015).
[146] G. X. Liu, B. Debnath, T. R. Pope, T. T. Salguero, R. K. Lake, and A. A. Balandin, *A charge-density-wave oscillator based on an integrated tantalum disulfide-boron nitride-graphene device operating at room temperature,* Nat. Nanotechnol. **11**, 844 (2016).
[147] Z. Yan, C. Jiang, T. R. Pope, C. F. Tsang, J. L. Stickney, P. Goli, J. Renteria, T. T. Salguero, and A. A. Balandin, *Phonon and thermal properties of exfoliated TaSe2 thin films,* J. Appl. Phys. **114** (2013).
[148] J. Renteria, R. Samnakay, C. Jiang, T. R. Pope, P. Goli, Z. Yan, D. Wickramaratne, T. T. Salguero, A. G. Khitun, R. K. Lake, and A. A. Balandin, *All-metallic electrically gated 2H-TaSe2 thin-film switches and logic circuits,* J. Appl. Phys. **115** (2014).
[149] R. Samnakay, D. Wickramaratne, T. R. Pope, R. K. Lake, T. T. Salguero, and A. A. Balandin, *Zone-Folded Phonons and the Commensurate-Incommensurate Charge-Density-Wave Transition in 1T-TaSe2 Thin Films,* Nano Lett. **15**, 2965 (2015).
[150] J. Chang, E. Blackburn, A. T. Holmes, N. B. Christensen, J. Larsen, J. Mesot, R. X. Liang, D. A. Bonn, W. N. Hardy, A. Watenphul, M. von Zimmermann, E. M. Forgan, and S. M. Hayden, *Direct observation of competition between superconductivity and charge density wave order in YBa2Cu3O6.67,* Nat. Phys. **8**, 871 (2012).
[151] X. S. Wang, H. B. Feng, Y. M. Wu, and L. Y. Jiao, *Controlled Synthesis of Highly Crystalline MoS2 Flakes by Chemical Vapor Deposition,* J. Am. Chem. Soc. **135**, 5304 (2013).
[152] M. Y. Li, Y. M. Shi, C. C. Cheng, L. S. Lu, Y. C. Lin, H. L. Tang, M. L. Tsai, C. W. Chu, K. H. Wei, J. H. He, W. H. Chang, K. Suenaga, and L. J. Li, *Epitaxial growth of a monolayer WSe2-MoS2 lateral p-n junction with an atomically sharp interface,* Science **349**, 524 (2015).

[153] F. Lévy, *Crystallography and crystal chemistry of materials with layered structure* 1976).
[154] R. Köppe, J. Steiner, and H. Schnöckel, *GaP_5 und InP_5: Ungewöhnliche Moleküle eröffnen neue Wege zur Reindarstellung von III/V ‐ Halbleitermaterialien,* Z. Anorg. Allg. Chem **629**, 2168 (2003).
[155] L. Chen, B. L. Liu, M. Y. Ge, Y. Q. Ma, A. N. Abbas, and C. W. Zhou, *Step-Edge-Guided Nucleation and Growth of Aligned WSe2 on Sapphire via a Layer-over-Layer Growth Mode,* Acs Nano **9**, 8368 (2015).
[156] S. Sugai, K. Murase, S. Uchida, and S. Tanaka, *Raman Studies of Lattice-Dynamics in 1t-Tise2,* Solid State Commun **35**, 433 (1980).
[157] B. Hildebrand, C. Didiot, A. M. Novello, G. Monney, A. Scarfato, A. Ubaldini, H. Berger, D. Bowler, C. Renner, and P. Aebi, *Doping Nature of Native Defects in 1T−$TiSe_2$,* Phys. Rev. Lett. **112**, 197001 (2014).
[158] A. M. Novello, B. Hildebrand, A. Scarfato, C. Didiot, G. Monney, A. Ubaldini, H. Berger, D. Bowler, P. Aebi, and C. Renner, *Scanning tunneling microscopy of the charge density wave in 1T−$TiSe_2$ in the presence of single atom defects,* Phys. Rev. B **92**, 081101 (2015).
[159] H. S. Zheng, S. Valtierra, N. Ofori-Opoku, C. H. Chen, L. F. Sun, S. S. Yuan, L. Y. Jiao, K. H. Bevan, and C. G. Tao, *Electrical Stressing Induced Monolayer Vacancy Island Growth on $TiSe_2$,* Nano Lett. **18**, 2179 (2018).
[160] Q. H. Wang, K. Kalantar-Zadeh, A. Kis, J. N. Coleman, and M. S. Strano, *Electronics and optoelectronics of two-dimensional transition metal dichalcogenides,* Nat Nanotechnol **7**, 699 (2012).
[161] A. Splendiani, L. Sun, Y. B. Zhang, T. S. Li, J. Kim, C. Y. Chim, G. Galli, and F. Wang, *Emerging Photoluminescence in Monolayer MoS2,* Nano Lett **10**, 1271 (2010).
[162] K. F. Mak, C. Lee, J. Hone, J. Shan, and T. F. Heinz, *Atomically Thin MoS2: A New Direct-Gap Semiconductor,* Phys Rev Lett **105**, 136805 (2010).
[163] R. Lv, H. Terrones, A. L. Elías, N. Perea-López, H. R. Gutiérrez, E. Cruz-Silva, L. P. Rajukumar, M. S. Dresselhaus, and M. Terrones, *Two-dimensional transition metal dichalcogenides: Clusters, ribbons, sheets and more,* Nano Today **10**, 559 (2015).
[164] H. D. Ozaydin, H. Sahin, J. Kang, F. M. Peeters, and R. T. Senger, *Electronic and magnetic properties of 1 T-TiSe 2 nanoribbons,* 2D Materials **2**, 044002 (2015).
[165] B. Radisavljevic and A. Kis, *Mobility engineering and a metal-insulator transition in monolayer MoS2,* Nat Mater **12**, 815 (2013).
[166] F. K. Perkins, A. L. Friedman, E. Cobas, P. M. Campbell, G. G. Jernigan, and B. T. Jonker, *Chemical Vapor Sensing with Mono layer MoS2,* Nano Lett **13**, 668 (2013).
[167] N. Wakabayashi, H. G. Smith, K. C. Woo, and F. C. Brown, *Phonons and Charge-Density Waves in It-Tise2,* Solid State Commun **28**, 923 (1978).
[168] D. Mihailovic, D. Dvorsek, V. V. Kabanov, J. Demsar, L. Forro, and H. Berger, *Femtosecond data storage, processing, and search using collective excitations of a macroscopic quantum state,* Appl Phys Lett **80**, 871 (2002).
[169] T. Ritschel, J. Trinckauf, K. Koepernik, B. Buchner, M. V. Zimmermann, H. Berger, Y. I. Joe, P. Abbamonte, and J. Geck, *Orbital textures and charge density waves in transition metal dichalcogenides,* Nat Phys **11**, 328 (2015).
[170] L. Yang, M. L. Cohen, and S. G. Louie, *Magnetic Edge-State Excitons in Zigzag Graphene Nanoribbons,* Phys Rev Lett **101**, 186401 (2008).
[171] C. G. Tao, L. Y. Jiao, O. V. Yazyev, Y. C. Chen, J. J. Feng, X. W. Zhang, R. B. Capaz, J. M. Tour, A. Zettl, S. G. Louie, H. J. Dai, and M. F. Crommie, *Spatially resolving edge states of chiral graphene nanoribbons,* Nat. Phys. **7**, 616 (2011).
[172] J. V. Lauritsen, M. V. Bollinger, E. Laegsgaard, K. W. Jacobsen, J. K. Norskov, B. S. Clausen, H. Topsoe, and F. Besenbacher, *Atomic-Scale Insight Into Structure and Morphology Changes of MoS2 Nanoclusters in Hydrotreating Catalysts,* Journal of Catalysts **221**, 510 (2004).
[173] J. H. Lin, S. T. Pantelides, and W. Zhou, *Vacancy-Induced Formation and Growth of Inversion Domains in Transition-Metal Dichalcogenide Monolayer,* Acs Nano **9**, 5189 (2015).

[174] C. O. Girit, J. C. Meyer, R. Erni, M. D. Rossell, C. Kisielowski, L. Yang, C. H. Park, M. F. Crommie, M. L. Cohen, S. G. Louie, and A. Zettl, *Graphene at the Edge: Stability and Dynamics,* Science **323**, 1705 (2009).
[175] X. T. Jia, M. Hofmann, V. Meunier, B. G. Sumpter, J. Campos-Delgado, J. M. Romo-Herrera, H. B. Son, Y. P. Hsieh, A. Reina, J. Kong, M. Terrones, and M. S. Dresselhaus, *Controlled Formation of Sharp Zigzag and Armchair Edges in Graphitic Nanoribbons,* Science **323**, 1701 (2009).
[176] K. E. N Provatas, *Phase-Field Methods in Materials Science and Engineering* (Wiley-VCH, 2011).
[177] K. Elder, H. Gould, and J. Tobochnik, *Langevin Simulations of Nonequilibrium Phenomena,* Computers in Physics **7**, 27 (1993).
[178] S. Rokkam, A. El-Azab, P. Millett, and D. Wolf, *Phase field modeling of void nucleation and growth in irradiated metals,* Model Simul Mater Sc **17**, 064002 (2009).
[179] B. Hildebrand, C. Didiot, A. M. Novello, G. Monney, A. Scarfato, A. Ubaldini, H. Berger, D. R. Bowler, C. Renner, and P. Aebi, *Doping Nature of Native Defects in 1T-TiSe2,* Phys Rev Lett **112**, 197001 (2014).
[180] J. Ishioka, Y. H. Liu, K. Shimatake, T. Kurosawa, K. Ichimura, Y. Toda, M. Oda, and S. Tanda, *Chiral Charge-Density Waves,* Phys Rev Lett **105**, 176401 (2010).
[181] H. Q. Zhou, F. Yu, Y. Y. Liu, X. L. Zou, C. X. Cong, C. Y. Qiu, T. Yu, Z. Yan, X. N. Shen, L. F. Sun, B. I. Yakobson, and J. M. Tour, *Thickness-dependent patterning of MoS2 sheets with well-oriented triangular pits by heating in air,* Nano Res **6**, 703 (2013).
[182] M. Yamamoto, T. L. Einstein, M. S. Fuhrer, and W. G. Cullen, *Anisotropic Etching of Atomically Thin MoS2,* J Phys Chem C **117**, 25643 (2013).
[183] P. Maksymovych, D. B. Dougherty, X. Y. Zhu, and J. T. Yates, *Nonlocal dissociative chemistry of adsorbed molecules induced by localized electron injection into metal surfaces,* Phys Rev Lett **99**, 016101 (2007).
[184] L. Chen, H. Li, and A. T. S. Wee, *Nonlocal Chemical Reactivity at Organic-Metal Interfaces,* Acs Nano **3**, 3684 (2009).
[185] L. Ratke and P. W. Voorhees, *Growth and coarsening ripening in material processing* (Springer, 2002).
[186] H. P. Komsa, S. Kurasch, O. Lehtinen, U. Kaiser, and A. V. Krasheninnikov, *From point to extended defects in two-dimensional MoS2: Evolution of atomic structure under electron irradiation,* Phys Rev B **88**, 035301 (2013).
[187] T. Michely, K. H. Besocke, and G. Comsa, *Observation of Sputtering Damage on Au(111),* Surf Sci **230**, L135 (1990).
[188] H. P. Komsa, J. Kotakoski, S. Kurasch, O. Lehtinen, U. Kaiser, and A. V. Krasheninnikov, *Two-Dimensional Transition Metal Dichalcogenides under Electron Irradiation: Defect Production and Doping,* Phys Rev Lett **109**, 035503 (2012).
[189] A. Bruix, J. V. Lauritsen, and B. Hammer, *Effects of particle size and edge structure on the electronic structure, spectroscopic features, and chemical properties of Au(111)-supported MoS2 nanoparticles,* Faraday Discuss **188**, 323 (2016).
[190] Y. Kim, J. L. Huang, and C. M. Lieber, *Characterization of Nanometer Scale Wear and Oxidation of Transition-Metal Dichalcogenide Lubricants by Atomic Force Microscopy,* Appl Phys Lett **59**, 3404 (1991).
[191] E. Delawski and B. A. Parkinson, *Layer-by-Layer Etching of 2-Dimensional Metal Chalcogenides with the Atomic Force Microscope,* J Am Chem Soc **114**, 1661 (1992).
[192] C. Enss, R. Winters, M. Reinermann, G. Weiss, S. Hunklinger, and M. LuxSteiner, *STM-study of triangular defect structures induced on WSe2,* Z Phys B Con Mat **99**, 561 (1996).
[193] J. C. Arnault, J. L. Bubendorff, A. Pimpinelli, and J. P. Bucher, *Transition in the growth kinetics of vacancy islands on NbSe2,* Surf Sci **348**, 185 (1996).

[194] S. Kondo, S. Heike, M. Lutwyche, and Y. Wada, *Surface Modification Mechanism of Materials with Scanning Tunneling Microscope,* J Appl Phys **78**, 155 (1995).
[195] T. E. Kidd, B. I. Gamb, P. I. Skirtachenko, and L. H. Strauss, *Dopant Enhanced Etching of TiSe2 by Scanning Tunneling Microscopy,* Langmuir **26**, 10980 (2010).
[196] D. Cao, T. Shen, P. Liang, X. S. Chen, and H. B. Shu, *Role of Chemical Potential in Flake Shape and Edge Properties of Mono layer MoS2,* J Phys Chem C **119**, 4294 (2015).
[197] W. Zhao and F. Ding, *Energetics and kinetics of phase transition between a 2H and a 1T MoS2 monolayer-a theoretical study,* Nanoscale **9**, 2301 (2017).
[198] K. H. Bevan, W. G. Zhu, H. Guo, and Z. Y. Zhang, *Terminating Surface Electromigration at the Source,* Phys Rev Lett **106**, 156404 (2011).
[199] K. H. Bevan, F. Zahid, D. Kienle, and H. Guo, *First-principles analysis of the STM image heights of styrene on Si(100),* Phys Rev B **76**, 045325 (2007).
[200] H. S. Zheng, Y. Choi, F. Baniasadi, D. K. Hu, L. Y. Jiao, K. Park, and C. G. Tao, *Visualization of point defects in ultrathin layered 1T-PtSe2,* 2D Mater. **6** (2019).
[201] X. Lin, J. Lu, Y. Shao, Y. Zhang, X. Wu, J. Pan, L. Gao, S. Zhu, K. Qian, and Y. Zhang, *Intrinsically patterned two-dimensional materials for selective adsorption of molecules and nanoclusters,* Nat. Mater. **16**, 717 (2017).
[202] X. Zou and B. I. Yakobson, *An Open Canvas: 2D Materials with Defects, Disorder, and Functionality,* Acc. Chem. Res. **48**, 73 (2014).
[203] Q. H. Wang, K. Kalantar-Zadeh, A. Kis, J. N. Coleman, and M. S. Strano, *Electronics and optoelectronics of two-dimensional transition metal dichalcogenides,* Nat. Nanotechnol. **7**, 699 (2012).
[204] J. Lauritsen, M. Nyberg, J. K. Nørskov, B. Clausen, H. Topsøe, E. Lægsgaard, and F. Besenbacher, *Hydrodesulfurization reaction pathways on MoS_2 nanoclusters revealed by scanning tunneling microscopy,* J. Catal. **224**, 94 (2004).
[205] Y. Zhang, J. Ye, Y. Matsuhashi, and Y. Iwasa, *Ambipolar MoS_2 thin flake transistors,* Nano Lett. **12**, 1136 (2012).
[206] H. Wang, L. Yu, Y.-H. Lee, Y. Shi, A. Hsu, M. L. Chin, L.-J. Li, M. Dubey, J. Kong, and T. Palacios, *Integrated circuits based on bilayer MoS_2 transistors,* Nano Lett. **12**, 4674 (2012).
[207] R. Lv, J. A. Robinson, R. E. Schaak, D. Sun, Y. Sun, T. E. Mallouk, and M. Terrones, *Transition metal dichalcogenides and beyond: synthesis, properties, and applications of single-and few-layer nanosheets,* Acc. Chem. Res. **48**, 56 (2014).
[208] K. Liu, B. J. Zheng, J. J. Wu, Y. F. Chen, X. Q. Wang, F. Qi, D. W. He, W. L. Zhang, and Y. R. Li, *Synthesis of two-dimensional semiconductor single-crystal $PtSe_2$ under high pressure,* J. Mater. Sci. **53**, 1256 (2018).
[209] M. Yan, E. Wang, X. Zhou, G. Zhang, H. Zhang, K. Zhang, W. Yao, N. Lu, S. Yang, and S. Wu, *High quality atomically thin $PtSe_2$ films grown by molecular beam epitaxy,* 2D Mater. **4**, 045015 (2017).
[210] W. Yao, E. Wang, H. Huang, K. Deng, M. Yan, K. Zhang, K. Miyamoto, T. Okuda, L. Li, and Y. Wang, *Direct observation of spin-layer locking by local Rashba effect in monolayer semiconducting $PtSe_2$ film,* Nat. Commun. **8**, 14216 (2017).
[211] J.-Q. Lei, K. Liu, S. Huang, and X.-L. Zhou, *The comparative study on bulk-$PtSe_2$ and 2D 1-Layer-$PtSe_2$ under high pressure via first-principle calculations,* Theor. Chem. Acc. **136**, 97 (2017).
[212] S.-D. Guo, *Biaxial strain tuned thermoelectric properties in monolayer $PtSe_2$,* J. Mater. Chem. C **4**, 9366 (2016).
[213] H. L. Zhuang and R. G. Hennig, *Computational search for single-layer transition-metal dichalcogenide photocatalysts,* J. Phys. Chem. C **117**, 20440 (2013).
[214] S. M. Hus and A. P. Li, *Spatially-resolved studies on the role of defects and boundaries in electronic behavior of 2D materials,* Prog. Surf. Sci. **92**, 176 (2017).

[215] Z. Lin, B. R. Carvalho, E. Kahn, R. T. Lv, R. Rao, H. Terrones, M. A. Pimenta, and M. Terrones, *Defect engineering of two-dimensional transition metal dichalcogenides,* 2D Mater. **3**, 022002 (2016).
[216] H. Schweiger, P. Raybaud, G. Kresse, and H. Toulhoat, *Shape and edge sites modifications of MoS_2 catalytic nanoparticles induced by working conditions: a theoretical study,* J. Catal. **207**, 76 (2002).
[217] H.-P. Komsa, J. Kotakoski, S. Kurasch, O. Lehtinen, U. Kaiser, and A. V. Krasheninnikov, *Two-dimensional transition metal dichalcogenides under electron irradiation: defect production and doping,* Phys. Rev. Lett. **109**, 035503 (2012).
[218] A. Mills, Y. F. Yu, C. H. Chen, B. V. Huang, L. Y. Cao, and C. G. Tao, *Ripples near edge terminals in MoS_2 few layers and pyramid nanostructures,* Appl. Phys. Lett. **108**, 081601 (2016).
[219] H.-P. Komsa and A. V. Krasheninnikov, *Two-dimensional transition metal dichalcogenide alloys: stability and electronic properties,* J. Phys. Chem. Lett. **3**, 3652 (2012).
[220] A. N. Enyashin, M. Bar-Sadan, L. Houben, and G. Seifert, *Line defects in molybdenum disulfide layers,* J. Phys. Chem. C **117**, 10842 (2013).
[221] X. Zou, Y. Liu, and B. I. Yakobson, *Predicting dislocations and grain boundaries in two-dimensional metal-disulfides from the first principles,* Nano Lett. **13**, 253 (2012).
[222] H. P. Komsa and A. V. Krasheninnikov, *Engineering the Electronic Properties of Two‐Dimensional Transition Metal Dichalcogenides by Introducing Mirror Twin Boundaries,* Adv. Electron. Mater. **3**, 1600468 (2017).
[223] Y. C. Yang, X. Li, M. R. Wen, E. Hacopian, W. B. Chen, Y. J. Gong, J. Zhang, B. Li, W. Zhou, P. M. Ajayan, Q. Chen, T. Zhu, and J. Lou, *Brittle Fracture of 2D $MoSe_2$,* Adv. Mater. **29**, 1604201 (2017).
[224] T. T. Tran, K. Bray, M. J. Ford, M. Toth, and I. Aharonovich, *Quantum emission from hexagonal boron nitride monolayers,* Nat. Nanotechnol. **11**, 37 (2016).
[225] Y. Liu, F. Xu, Z. Zhang, E. S. Penev, and B. I. Yakobson, *Two-dimensional mono-elemental semiconductor with electronically inactive defects: the case of phosphorus,* Nano Lett. **14**, 6782 (2014).
[226] J. F. Gao, Y. Cheng, T. Tian, X. L. Hu, K. Y. Zeng, G. Zhang, and Y. W. Zhang, *Structure, Stability, and Kinetics of Vacancy Defects in Monolayer $PtSe_2$: A First-Principles Study,* Acs Omega **2**, 8640 (2017).
[227] D. K. Hu, G. C. Xu, L. Xing, X. X. Yan, J. Y. Wang, J. Y. Zheng, Z. X. Lu, P. Wang, X. Q. Pan, and L. Y. Jiao, *Two-Dimensional Semiconductors Grown by Chemical Vapor Transport,* Angew. Chem. Int. Ed. **56**, 3611 (2017).
[228] G. Kresse and J. Furthmüller, *Efficient iterative schemes for ab initio total-energy calculations using a plane-wave basis set,* Phys. Rev. B **54**, 11169 (1996).
[229] G. Kresse and J. Furthmüller, *Efficiency of ab-initio total energy calculations for metals and semiconductors using a plane-wave basis set,* Comput. Mater. Sci **6**, 15 (1996).
[230] D. M. Ceperley and B. Alder, *Ground state of the electron gas by a stochastic method,* Phys. Rev. Lett. **45**, 566 (1980).
[231] P. E. Blöchl, *Projector augmented-wave method,* Phys. Rev. B **50**, 17953 (1994).
[232] S. Furuseth, K. Selte, and A. Kjekshus, *Redetermined Crystal Structures of $NiTe_2$, $PdTe_2$, PtS_2, $PtSe_2$ and $PtTe_2$,* Acta Chem. Scand. **19**, 257 (1965).
[233] G. Kliche, *Far-infrared and X-ray investigations of the mixed platinum dichalcogenides $PtS_{2-x}Se_x$, $PtSe_{2-x}Te_x$, and $PtS_{2-x}Te_x$,* J. Solid State Chem. **56**, 26 (1985).
[234] G. Y. Guo and W. Y. Liang, *The Electronic-Structures of Platinum Dichalcogenides - PtS_2, $PtSe_2$ and $PtTe_2$,* J. Phys. C: Solid State Phys. **19**, 995 (1986).
[235] J. P. Perdew, K. Burke, and M. Ernzerhof, *Generalized gradient approximation made simple,* Phys. Rev. Lett. **77**, 3865 (1996).
[236] W. Zhang, J. Qin, Z. Huang, and W. Zhang, *The mechanism of layer number and strain dependent bandgap of 2D crystal $PtSe_2$,* J. Appl. Phys. **122**, 205701 (2017).
[237] M. J. Piotrowski, R. K. Nomiyama, and J. L. F. Da Silva, *Role of van der Waals corrections for the PtX_2 (X = O, S, Se) compounds,* Phys. Rev. B **88**, 075421 (2013).

[238] A. Ciarrocchi, A. Avsar, D. Ovchinnikov, and A. Kis, *Thickness-modulated metal-to-semiconductor transformation in a transition metal dichalcogenide,* Nat. Commun. **9**, 919 (2018).
[239] K. N. Zhang, M. Z. Yan, H. X. Zhang, H. Q. Huang, M. Arita, Z. Sun, W. H. Duan, Y. Wu, and S. Y. Zhou, *Experimental evidence for type-II Dirac semimetal in $PtSe_2$,* Phys. Rev. B **96**, 125102 (2017).
[240] S. Grimme, *Semiempirical GGA-type density functional constructed with a long-range dispersion correction,* J. Comput. Chem. **27**, 1787 (2006).
[241] S. Grimme, J. Antony, S. Ehrlich, and H. Krieg, *A consistent and accurate ab initio parametrization of density functional dispersion correction (DFT-D) for the 94 elements H-Pu,* J. Chem. Phys. **132**, 154104 (2010).
[242] J. Tersoff and D. R. Hamann, *Theory and Application for the Scanning Tunneling Microscope,* Phys. Rev. Lett. **50**, 1998 (1983).
[243] J. Tersoff and D. R. Hamann, *Theory of the Scanning Tunneling Microscope,* Phys. Rev. B **31**, 805 (1985).
[244] J. Kellner, G. Bihlmayer, V. L. Deringer, M. Liebmann, C. Pauly, A. Giussani, J. E. Boschker, R. Calarco, R. Dronskowski, and M. Morgenstern, *Exploring the subsurface atomic structure of the epitaxially grown phase-change material $Ge_2Sb_2Te_5$,* Phys. Rev. B **96**, 245408 (2017).
[245] J. Klijn, L. Sacharow, C. Meyer, S. Blugel, M. Morgenstern, and R. Wiesendanger, *STM measurements on the InAs(110) surface directly compared with surface electronic structure calculations,* Phys. Rev. B **68**, 205327 (2003).
[246] S. A. Pan, Q. Fu, T. Huang, A. D. Zhao, B. Wang, Y. Luo, J. L. Yang, and J. G. Hou, *Design and control of electron transport properties of single molecules,* Proc. Natl. Acad. Sci. U.S.A. **106**, 15259 (2009).
[247] K. Momma and F. Izumi, *VESTA 3 for three-dimensional visualization of crystal, volumetric and morphology data,* J. Appl. Crystallogr. **44**, 1272 (2011).
[248] C. Freysoldt, B. Grabowski, T. Hickel, J. Neugebauer, G. Kresse, A. Janotti, and C. G. Van de Walle, *First-principles calculations for point defects in solids,* Rev. Mod. Phys. **86**, 253 (2014).
[249] A. V. Krukau, O. A. Vydrov, A. F. Izmaylov, and G. E. Scuseria, *Influence of the exchange screening parameter on the performance of screened hybrid functionals,* J. Chem. Phys. **125**, 224106 (2006).
[250] M. A. U. Absor, I. Santoso, K. Abraha, F. Ishii, and M. Saito, *Defect-induced large spin-orbit splitting in monolayer $PtSe_2$,* Phys. Rev. B **96**, 115128 (2017).
[251] C. J. Chen, *Origin of Atomic Resolution on Metal-Surfaces in Scanning Tunneling Microscopy,* Phys. Rev. Lett. **65**, 448 (1990).
[252] S. Barja, *Identifying substitutional oxygen as a prolific point defect in monolayer transition metal dichalcogenides with experiment and theory,* Preprint at https://arxiv.org/abs/1810.03364 (2018).
[253] C. D. Zhang, C. Wang, F. Yang, J. K. Huang, L. J. Li, W. Yao, W. Ji, and C. K. Shih, *Engineering Point-Defect States in Monolayer WSe_2,* Acs Nano **13**, 1595 (2019).
[254] Y. J. Zheng, Y. F. Chen, Y. L. Huang, P. K. Gogoi, M. Y. Li, L. J. Li, P. E. Trevisanutto, Q. X. Wang, S. J. Pennycook, A. T. S. Wee, and S. Y. Quek, *Point Defects and Localized Excitons in 2D WSe_2,* Acs Nano **13**, 6050 (2019).